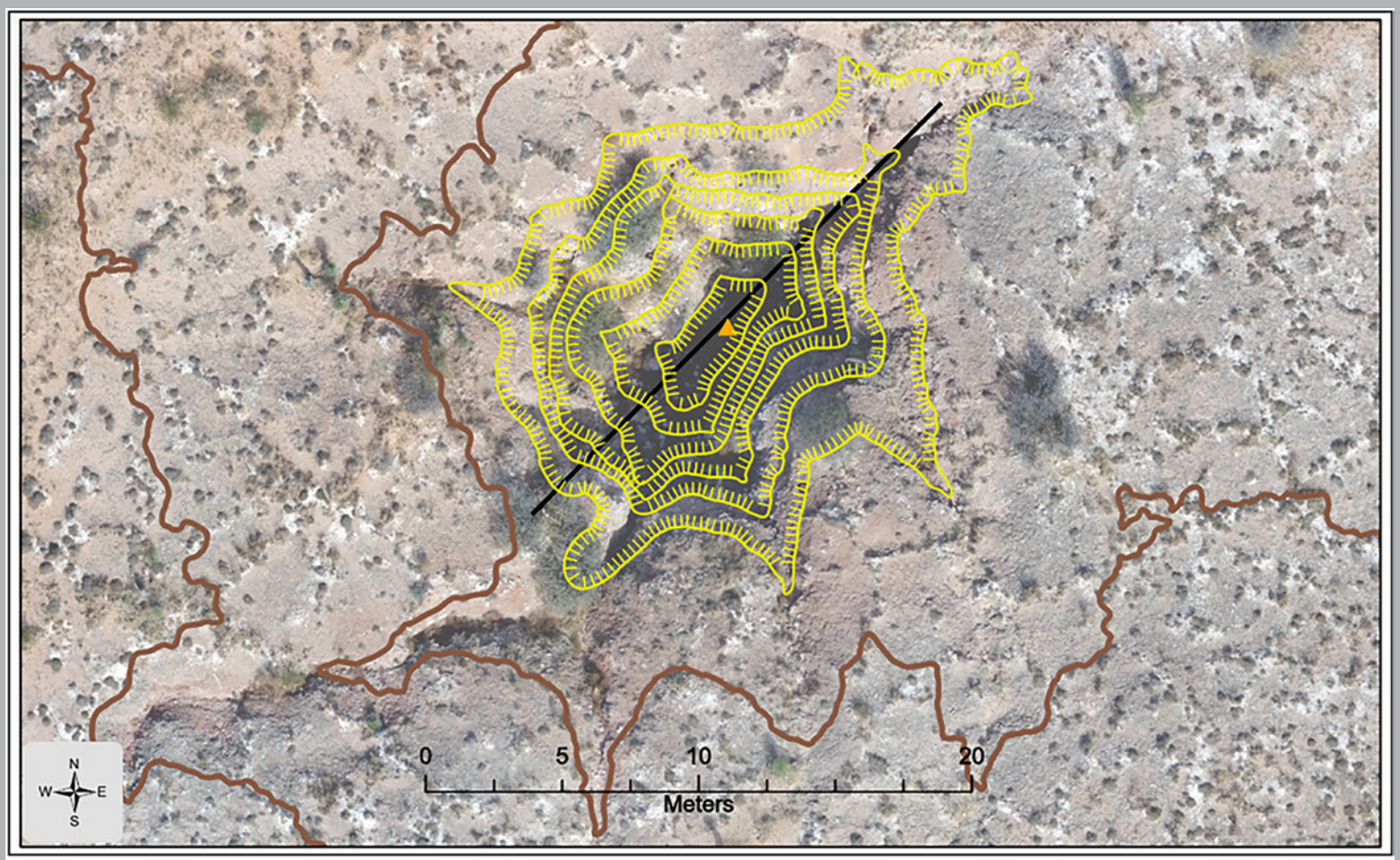
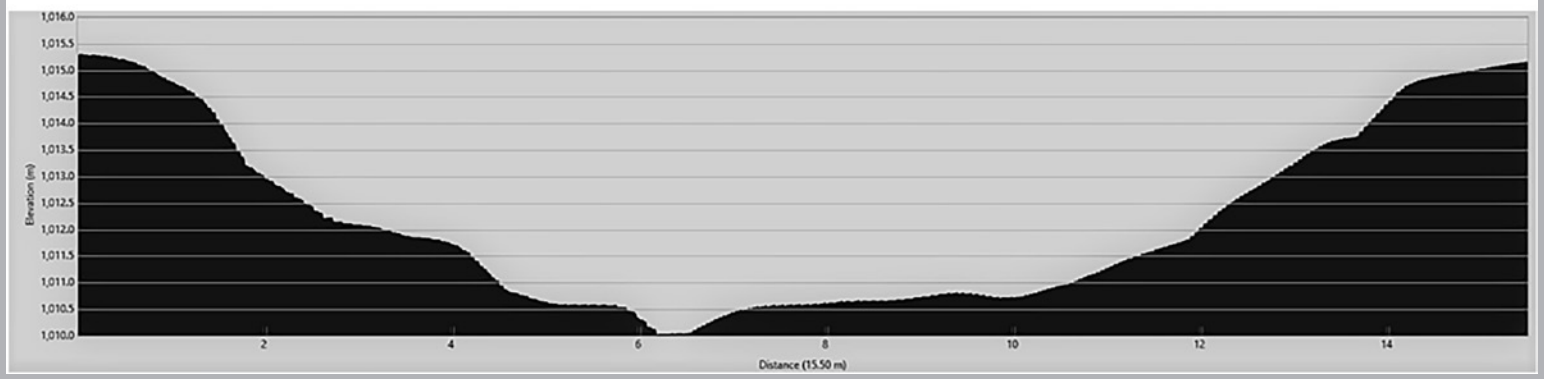
JOURNAL OF CAVE AND KARST STUDIES

September 2026
Volume 88, Number 3
ISSN 1090-6924
A Publication of the National Speleological Society





DEDICATED TO THE ADVANCEMENT OF SCIENCE, EDUCATION, EXPLORATION, AND CONSERVATION

Published By
The National Speleological Society

http://caves.org/pub/journal

Office
6001 Pulaski Pike NW
Huntsville, AL 35810 USA
Tel:256-852-1300
nss@caves.org

Editor-in-Chief
Malcolm S. Field
Washington, DC
703-347-8601
field.malcolm1@gmail.com

Production Editor
Scott A. Engel
Knoxville, TN
225-281-3914
sengel@caves.org

The *Journal of Cave and Karst Studies* , ISSN 1090-6924, CPM Number #40065056, is a multi-disciplinary, refereed journal published four times a year by the National Speleological Society. The *Journal* is available by open access on its website, or check the website for current print subscription rates. Back issues are available from the NSS office.

POSTMASTER: send address changes to the National Speleological Society Office listed above.

The Journal of Cave and Karst Studies is covered by the following ISI Thomson Services Science Citation Index Expanded, ISI Alerting Services, and Current Contents/Physical, Chemical, and Earth Sciences.

Copyright © 2026
by the National Speleological Society, Inc.

BOARD OF EDITORS

Anthropology
George Crothers
University of Kentucky
Lexington, KY
george.crothers@utk.edu

Conservation-Life Sciences
Julian J. Lewis & Salisa L. Lewis
Lewis & Associates, LLC.
Borden, IN
lewisbioconsult@aol.com

Earth Sciences
Benjamin Schwartz
Texas State University
San Marcos, TX
bs37@txstate.edu

Yongli Gao
University of Texas at San Antonio
yongli.gao@utsa.edu

Mario Parise
University Aldo Moro
Bari, Italy
mario.parise@uniba.it

Carol Wicks
Louisiana State University
Baton Rouge, LA
cwicks@lsu.edu

Exploration
Paul Burger
National Park Service
Eagle River, Alaska
paul_burger@nps.gov

Microbiology
Sarah Keenan
South Dakota School of Mines and Technology
Rapid City, SD
Sarah.Keenan@sdsmt.edu

Paleontology
Greg McDonald
National Park Service
Fort Collins, CO
greg_mcdonald@nps.gov

Social Sciences
Vacant

Front Cover: Drone generated orthomosaic of Whirlpool Sink, New Mexico. By MS Chenoweth.

Sarah Carmichael, James Seward, Bryce Norvell, Lucca Scoggins, Anna-Maria Riley, Morgan Smith, Howard Neufeld, and Suzanna Bräuer. The relationship between sediment geochemistry, manganese oxidation, human traffic, and microbial community structure across three southern Appalachian caves. *Journal of Cave and Karst Studies*, v. 88, no. 3, p. 45-61. DOI: 10.4311/2025MB0100

THE RELATIONSHIP BETWEEN SEDIMENT GEOCHEMISTRY, MANGANESE OXIDATION, HUMAN TRAFFIC, AND MICROBIAL COMMUNITY STRUCTURE ACROSS THREE SOUTHERN APPALACHIAN CAVES

Sarah Carmichael[1,C], James Seward[2], Bryce Norvell[3], Lucca Scoggins[1], Anna-Maria Riley[3], Morgan Smith[3,4], Howard Neufeld[3], and Suzanna Bräuer[3]

Abstract

Three southern Appalachian caves were assessed in a multiproxy analysis to determine if human visitation and modification of the cave environment could influence cave mineralogy, inorganic geochemistry, and microbial community assemblages. Cave sediments were collected from Daniel Boone Caverns in Fort Blackmore, VA (gated and locked with few visitors); Worley's Cave in Bluff City, TN (a wild show cave); and Linville Caverns outside of Marion, NC (a developed show cave). Sediments were all analyzed using Illumina sequencing for microbial community structure, as well as a combination of X-ray diffraction, whole-rock geochemistry, particle size distributions, and transmission electron microscopy (TEM) for mineral characterization. Distinct geochemical and microbial signatures were found both within and between the caves. Biological manganese oxidation was present in all three caves, with significant differences in geochemistry across sites that contained Mn oxides and those that did not. Geochemistry and mineralogy of sediments primarily reflected the local bedrock rather than human-associated traffic and detritus. PCA plots using whole-rock geochemistry (cross-referenced with X-ray diffraction data) indicate that sediment variability between caves was due to the amount of clay minerals relative to detrital feldspars and quartz, as well as the amount of detrital heavy minerals relative to Mn oxidation and phosphate. Sediment-hosted microbial communities from Linville Caverns (the most highly developed of the three caves) contained more Bacteroidota (a phylum associated both with high-molecular weight carbon and humans) than the other two caves, while Daniel Boone Caverns, a relatively pristine cave, contained more Thermoplasmatota, Chloroflexota, and Nitrospirota (oligotrophic phyla). Overall, our data corroborate studies demonstrating that Bacteroidota are positively correlated and Nitrospirota are negatively correlated with anthropogenic and nutrient input, and that bedrock type exerts a strong influence both on sediment geochemistry and on microbial community structure.

INTRODUCTION

Karst systems host vital sources of potable drinking water on a global scale (Hartmann et al., 2014) and support some of the most fragile and diverse ecosystems on Earth (Barton and Jurado, 2007; Engel, 2010; Brannen-Donnelly and Engel, 2015; Ma et al., 2021). Cave microorganisms are sensitive to variations in DOM from drip water (Cheng et al., 2024), flooding and sediment age (Mulec et al., 2025), artificial lighting (Mulec and Kosi, 2009; Burgoyne et al., 2021), and human visitation (Pronk et al., 2007, 2009; Bontemps et al., 2022). In particular, the anthropogenic impact in cave ecosystems has been globally documented (Zhong et al., 2011; Faimon et al., 2012; Saiz-Jimenez, 2012), and human visitation and the influx of human-derived materials can lead to the destruction of microhabitats (Northup, 2011), alteration of biogeochemical cycles, the introduction of fecal (Carmichael et al., 2013b) and skin-hosted (Biagioli et al., 2023) bacteria and fungi, the introduction of alien or invasive species (Nicolosi et al., 2023), and impacts on sensitive cave fauna such as bats (Blehert et al., 2011). Natural caves are oligotrophic and maintain a relatively consistent temperature throughout the year (Barton and Jurado, 2007; Barton et al., 2007). Show caves disrupt this natural equilibrium by the installation of artificial lighting, stairs, and trails and by inputs from human visitors (Saiz-Jimenez, 2012; Cigna, 2019; Biagioli et al., 2023). In addition, microplastic deposition is considered a biomarker for anthropogenic impact and has also been documented in cave sediments and karst aquifers (for example, see summary papers by Balestra et al., 2023; Hasenmueller et al., 2023; Piccardo and Bevilacqua, 2024), and similar observations have also been documented in southern Appalachian caves (Riley, 2024). These human-induced alterations can contribute to changes in cave microbial biodiversity (Fernandez-Cortes et al., 2011; Gillieson, 2011; Biagioli et al., 2023).

Many caves contain dark brown to black manganese (Mn) oxide biofilms or ferromanganese deposits comprised of higher concentrations of Mn and Fe than the surrounding bedrock (Northup et al., 2003; Carmichael and Bräuer, 2015). Field evidence from epigenic caves in the southern Appalachian Mountains indicates that Mn oxidation is stimulated by

[1]Department of Geological and Environmental Sciences, Appalachian State University, Boone, NC
[2]Department of Geography, McGill University, Montreal, Québec H3A 0G4
[3]Department of Biology, Appalachian State University, Boone, NC, 28608
[4]Stallergenes Greer, Lenoir, NC, 28645
[C]Corresponding author: carmichaelsk@appstate.edu.

exogenous carbon input into carbon-limited environments (Carmichael et al., 2013a, 2013b, 2015; Cloutier et al., 2017), which may vary spatially and temporally (He et al., 2024) and may also be influenced by epikarst (Pipan and Culver, 2013). We hypothesize that cave bedrock mineralogy and geochemistry may strongly influence these processes as well. Indeed, the impact of mineral type (Hutchens et al., 2010) or host rock (Barton et al., 2007) on microbial communities and the interactions of specific microorganisms with specific minerals (Kosznik-Kwaśnicka et al., 2022) have been well documented. In this study, we sought to determine to what degree (if any) human visitation and modification of the cave environment may influence cave mineralogy and/or geochemistry as well as microbial community assemblages. If this relationship appears robust, we can then characterize microbial assemblages in cave sediment as potential biomarkers that can represent different types of human impact.

SITE DESCRIPTIONS

Three caves from the Southern Appalachian Mountains were sampled for this study (Fig. 1, Table 1). We compared a developed show cave (Linville Caverns) with two wild caves: one that hosts tour groups as well as recreational cavers (Worley's Cave) and one that is gated, locked, and closed to the public (Daniel Boone Caverns).

Linville Caverns (LC) is located in McDowell County, North Carolina, along the North Fork of the Catawba River. It is in the Eastern Blue Ridge tectonic province and is hosted in the Cambrian Shady Dolomite, within a structural karst window between the Chattahoochee–Holland Mountain Fault and Cambrian siliciclastic rocks of the Grandfather Mountain Window (Thigpen et al., 2022). The cave is surrounded by hardwood and rhododendron forest (surrounded by the Pisgah National Forest) and is located in extremely steep terrain. It is a highly trafficked show cave that has been active since 1937 (https://www.linvillecaverns.com), receiving over 100,000 visitors a year (official Linville Caverns tourism brochure). A concrete path covers most of the floor in areas open to the public, and stairs, handrails, and artificial lights are present in certain areas as well.

Worley's Cave is found within the Ordovician Knox Dolomite of the Western Valley and Ridge province in Sullivan County, TN (near Bluff City, TN). It is structurally associated with the footwall of the Holston-Iron Mountain thrust sheet (Hatcher et al., 2007) and is surrounded by a mix of single family homes, small hardwood forest tracts (approximately 1–2 acres), and small agricultural fields raising both cattle and hay. It is frequently visited by recreational cavers and adventure tourism groups (estimated by the authors at ~10,000 visitors per year, as no publicly available records are kept). The cave contains a subterranean creek and is hydrologically linked to sinkholes in neighboring farm fields (Burnham et al., 2016).

Daniel Boone Caverns in Scott County, Virginia, is rarely visited and can therefore be considered a pristine cave (Carmichael et al., 2013a, 2015). It is located in the Eastern Valley and Ridge tectonic province, approximately 64 km northeast of Worley's Cave, and is also hosted within the Ordovician Knox Dolomite. It is located on the St. Paul-Honaker thrust sheet (Kulander and Dean, 1986) between the Copper Creek and Clinchport thrust faults (Virginia Division of Mineral Resources, 1993). It contains several drip pools, but lacks a complex subsurface hydrologic system; its location on an isolated ridge within a hardwood forest indicates that it does not experience any agricultural or municipal runoff, which has been confirmed with water testing (Carmichael et al., 2013a, 2013b).

MATERIALS AND METHODS

Sampling Protocol

Sites within each cave were chosen to assess the variability in microbial structures based on the amount of human foot traffic, manganese oxidation, and/or artificial light exposure (Table 2). All samples were taken from horizontal surfaces such as terraces, shelves, and the cave floor, rather than from vertical cave walls. Samples were taken by scraping the collection tube along the sample site's surface and placed on ice to be transported back to the lab. Samples were stored at −80 °C, with splits taken for whole-rock geochemical and mineralogical analysis. Manganese oxidation was detected using the Leucobeurbelin blue (LBB) assay (Krumbein and Altmann, 1973). In addition to the 21 samples taken from inside the cave, two surface samples of representative sediment/soil were taken in Falcon tubes from outside of the entrance of each cave: each cave had sediment sampled from the pathway directly in front of the cave entrance, and associated soil/sediment was taken at least 2 m from the cave entrance. Additional reference soil and sediment samples were taken from locations >2 m from each cave entrance where visitors do not walk, and were used as comparisons with cave sediment that may have experienced human foot traffic. These samples were analyzed with scanning transmission electron microscopy (see Geochemistry and Mineralogy, below), to determine if cave sediment mineralogy and any distinctive nanoparticles were influenced by human traffic coming into the cave or were naturally occuring in the soil.

Foot traffic levels were categorized as *High, Medium, Low*, and *Very Low*. These categories were qualitatively assigned based on direct observations of where tour groups go within show caves, as well as communications with cave owners about the number of visitors per year. The estimated number of visitors is summarized in Table 1. *High* traffic indicates an area with significant, repeated foot traffic, such as main footpaths along guided tour areas. *Medium* traffic

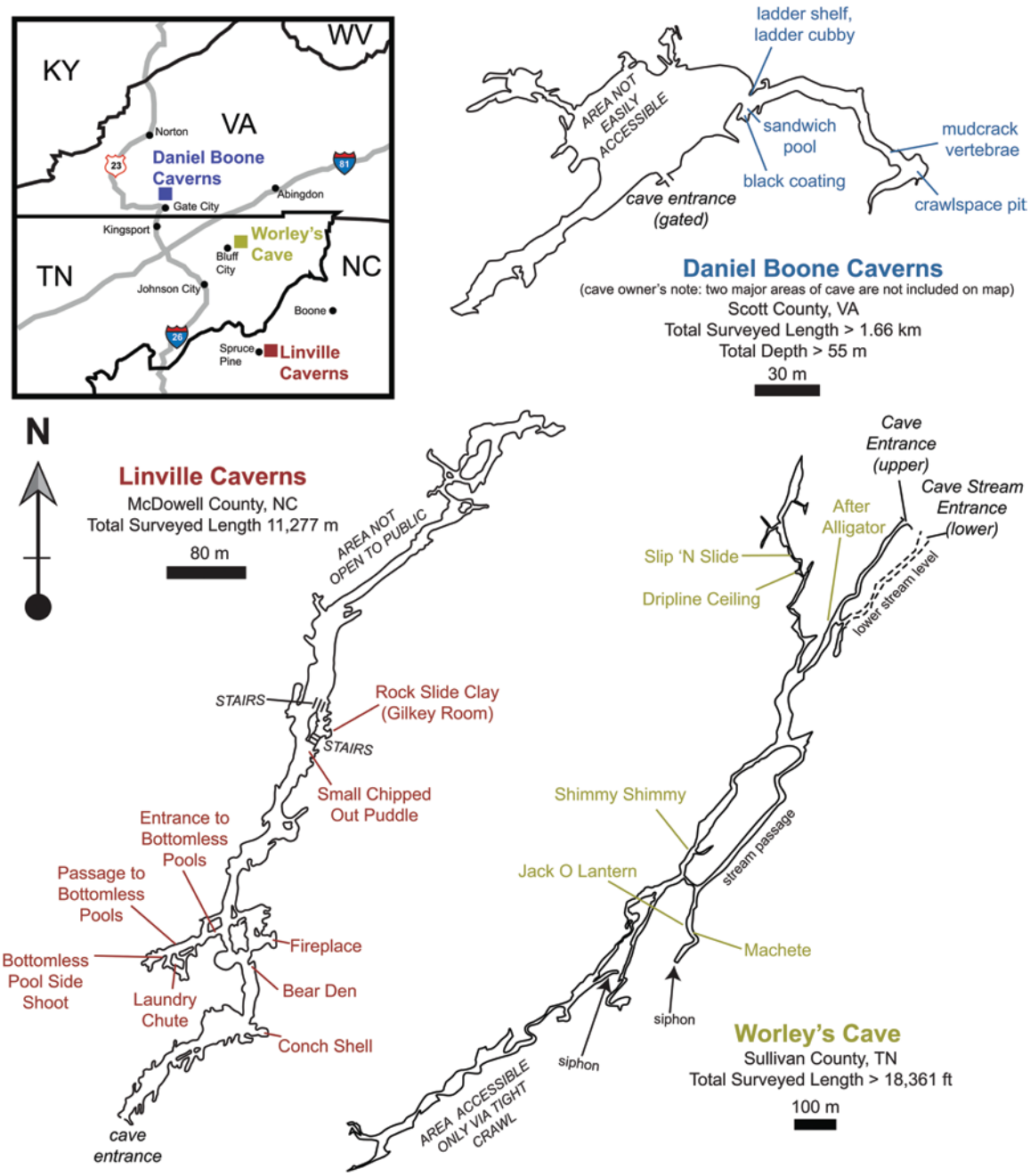


Figure 1. Maps of Linville Caverns, Daniel Boone Caverns, and Worley's Cave with the entrances and sample sites marked. Sample locations are shown using the corresponding color to the cave label and are described in detail in Table 1. Inset shows the relative locations of the three caves within NC, TN, and VA. Linville Caverns map modified from Bailey et al. (1987), and Worley's Cave and Daniel Boone Caverns maps modified from Carmichael et al. (2013a) and Cloutier et al. (2017).

indicates areas where it is easily possible to go off the main path, but tours do not typically bring visitors through the area. *Low* traffic indicates areas where the public is not necessarily prohibited from going but would be unlikely to go to on their own. *Very Low* traffic areas are places where the public is not permitted to go.

Twenty-one sediment samples were collected across the three caves. Linville Caverns had nine sample sites within the cave, representing varying levels of foot traffic, artificial lighting, and manganese oxidation. Six samples were taken from Worley's Cave: three from sites with little to no Mn oxidation, and three from sites that showed signs of current Mn oxidation (of these, three sites were classified as High foot traffic, while three were classified as Low foot traffic). Six samples were taken from Daniel Boone Caverns as well: three sites with little to no Mn oxidation and three sites with Mn oxidation. All samples from Daniel Boone Caverns were classified as Very Low traffic.

Table 1. Cave descriptions, bedrock geology, and surrounding features.

	Linville Caverns (LC)	Worley's Cave (WC)	Daniel Boone Caverns (DBC)
Bedrock Geology	Shady Dolomite (Cambrian)	Knox Group—Dolomite (Ordovician)	Knox Group—Dolomite (Ordovician)
Appalachian physiographic province	Eastern Blue Ridge	Eastern Valley and Ridge	Western Valley and Ridge
Associated structural features	Chattahoochee–Holland Mountain Fault (karst window), adjacent to Grandfather Mountain Window	Holston-Iron Mountain thrust sheet (footwall)	Between Copper Creek and Clinchport thrust faults
Surface environment	Hardwood and rhododendron forest, surrounded by Pisgah National Forest, on North Fork of Catawba River	Single family housing, subsistence agriculture (cattle, hay), pockets of hardwood forest	Hardwood forest, side of ridge on undeveloped land
Human visitation characteristics	Developed show cave (100,000 visitors/year) with walkways and artificial lighting	Undeveloped show cave, numerous tour groups, and recreational cavers (visitors/year estimated at ~5,000–10,000)	Undeveloped private cave, gated and locked (visitors/year estimated at ~10, including the authors of this paper)

Geochemistry and Mineralogy

Whole-rock geochemistry of cave sediment was performed at Activation Laboratories in Ancaster, Ontario, Canada, using the Lithogeochemistry and Whole Rock Analysis 4E - Exploration package. Mineralogy of cave sediment was assessed using a Shimadzu 6000 powder X-ray diffraction system with a Cu X-ray source, measured from 5°–80° 2θ in the Department of Geological and Environmental Sciences, Appalachian State University. Preliminary mineral identification was assigned via Match! Phase identification software from Crystal Impact, using the American Mineralogist database. Mineralogy was confirmed via scanning transmission and spot transmission electron microscopy with energy dispersive X-ray spectroscopy (STEM, TEM–EDS) at 120 kV and 65.5 µA using a JEOL JEM-1400 TEM with an Oxford Xplore TEM 80 mm^2 EDS detector in the Dewel Microscopy Facility at Appalachian State University.

Microbiology

DNA was extracted using the MP Biomedicals FastDNA spin kit for soil. Sequencing was performed at MR DNA on a MiSeq using the 515/806 primers of the V4 variable region of the 16S rRNA gene. MR DNA (Shallowater, TX, USA) was used for library preparation and sequencing. Forward and reverse sequences were then aligned using DADA2, and the nucleotide lengths were trimmed to <200 and 190 for forward and reverse reads, respectively (Callahan et al., 2016). A minimum overlap of 12 base pairs was established, sequences were denoised, and chimeras were removed. The SILVA 138 SSU database was used to assign taxonomy (McLaren and Callahan, 2021). Sequence data were converted to relative abundances of taxa per group as a proportion of all sequences for use in taxonomic figures (McMurdie and Holmes, 2013). Sequence data were deposited in the NCBI Sequence Read Archive (SRA) under BioProject accession PRJNA1468723.

Statistical Methods and Multivariate Analysis

All statistical analyses were conducted in RStudio (version 2024.04.1+748) (Allaire, 2012). Alpha diversity metrics, including Shannon and Simpson diversities as well as Pielou's evenness (Heip, 1974) and observed richness (Phylum classification), were calculated using the vegan package 2.7-3 (Oksanen et al., 2007) in RStudio. Pielou's evenness was calculated using Shannon diversity divided by the natural logarithm of observed richness. Differences in alpha diversity between caves were assessed using Kruskal–Wallis tests. Beta diversity was determined using Bray–Curtis dissimilarity calculated from phylum-level relative abundance. Two-sample, two-tailed, unpaired *t*-tests were also used to determine any statistically significant differences between the geochemical factors within Mn-positive and Mn-negative samples taken from a cave. Non-metric multidimensional scaling (NMDS) ordinations were made using the metaMDS function in the vegan package 2.7.3 (Oksanen et al., 2007). Ordination stress values were used to assess goodness-of-fit. Community analyses utilized the vegan package 2.7-3 (Oksanen et al., 2007). Figures were generated using the ggplot2 package 4.0.2 (Wickham, 2011). Differences in phylum-level microbial community structure between cave locations, as well as traffic intensities, were assessed using permutational multivariate analysis of variance (PERMANOVA) with the adonis2 function (vegan package 2.7.3) using 9999 permutations. Single- and marginal-effect models were assessed with independent effects of cave location and human traffic intensity on microbial community composition. Relationships between microbial communities and geochemical variables were evaluated using environmental fitting (envfit) and overlayed onto NMDS ordinations to determine variables associated with community clustering. Ordination ellipses were plotted at the 99% confidence level grouped by cave location.

Table 2. Sample site descriptions denoting the presence (+) or absence (−) of Mn oxidation, the amount of human traffic in the area, the presence of artificial lighting, and dominant mineralogy. Mineralogy assessed via powder X-ray diffraction (XRD) and/or transmission electron microscopy with energy dispersive X-ray spectroscopy (TEM–EDS) when needed. Some trace mineral structures were not identifiable via TEM–EDS, so are noted only by mineral formula or metal oxide group.

Sample Site	Cave	Mn +/−	Traffic	Light Level	Visual Site Description	Mineralogy
After Alligator	WC	(+)	High	No light	Approximately 1 m after alligator graffiti on way into cave	Quartz$^{(m)}$, illite, microcline, chlorite$^{(tr)}$
Machete	WC	(+)	Low	No light	Gravel stream bank at bend in stream passage; machete had been stabbed into the gravel at the time of sampling.	Quartz$^{(m)}$, illite, chlorite, microcline, birnessite$^{(tr)}$
Jack O Lantern	WC	(+)	Low	No light	Large flowstone deposit in stream passage; sample taken from clay and gravel underneath flowstone.	Quartz$^{(m)}$, illite$^{(tr)}$, chlorite$^{(tr)}$, microcline$^{(tr)}$
Shimmy Shimmy	WC	(−)	High	No light	Steep drop in cave before stream access; requiring “shimmying” down on all fours to the grab sample	Quartz$^{(m)}$, illite, chlorite, microcline
Dripline Ceiling	WC	(−)	Low	No light	Linear series of small (5 cm diameter) drip pools in clay floor from ceiling cave bacon drips above; forming line of puddles full of pebbles	Quartz$^{(m)}$, illite, chlorite, microcline
Slip ‘N Slide’	WC	(−)	High	No light	Clay bank with slippery ramp that leads down into Dripline Ceiling	Quartz$^{(m)}$, illite, chlorite, microcline
Ladder Shelf	DBC	(+)	Very low	No light	Small clay shelf near first ladder leading down into pit	Microcline$^{(m)}$, quartz, illite
Ladder Cubby	DBC	(+)	Very low	No light	Small clay hollowed out “cubby” above second ladder	Quartz$^{(m)}$, microcline, illite
Black Coating	DBC	(+)	Very low	No light	Pit below first ladder with lots of black coatings surrounding calcite veins; samples look like ice cream sandwiches	Dolomite$^{(m)}$, quartz, microcline$^{(tr)}$, birnessite$^{(tr)}$
Crawlspace Pit	DBC	(−)	Very low	No light	Small (1 m deep) breakdown pit at the back of the cave, past the mudcrack tunnel when the room opens up	Dolomite, quartz, microcline, calcite, chlorite
Sandwich Pool	DBC	(−)	Very low	No light	Drip pool at base of first ladder	Quartz, microcline, illite, dolomite$^{(tr)}$, chlorite$^{(tr)}$
Mudcrack Vertebrae	DBC	(−)	Very low	No light	Concretion (~20 cm diameter) that looks like large vertebrae, in mudcrack tunnel after cave popcorn crawl	Quartz, microcline
Rock Slide Clay (Gilkey Room)	LC	(+)	Medium	No lights	Small rubble/clay slump in “Gilkey Room” (as named by cave owners)	Illite, quartz, microcline, Fe oxides (biological?), Mn oxides (biological), apatite$^{(tr)}$, TiO_2 nanoparticles in illite clay$^{(tr)}$
Laundry Chute	LC	(+)	Low	No lights	Pit 30 cm in diameter opens into Bottomless Pool, has smooth walls, and looks like laundry chute	Illite$^{(m)}$, microcline, Fe oxides (biological?), TiO_2 nanoparticles in illite clay$^{(tr)}$
Conch Shell	LC	(+)	High	Direct light	Speleothem that looks like conch shell (as named by cave owners)	Illite$^{(m)}$, Mn oxide (biological), detrital rutile$^{(tr)}$, TiO_2 nanoparticles in illite clay$^{(tr)}$
Bottomless Pool Side Shoot	LC	(+)	Low	No lights	Narrow side passage at back of the Bottomless Pool area	Illite, microcline, quartz, dolomite, albite, calcite, Fe oxide$^{(tr)}$, detrital rutile$^{(tr)}$
Passage to Bottomless Pool	LC	(−)	Low	No lights	Main passage to the Bottomless Pool area (passage no longer used by public)	Illite, dolomite, quartz, microcline, albite, calcite, Fe oxide (biological?), TiO_2 nanoparticles in illite clay$^{(tr)}$
Bear Den	LC	(+)	Low	No lights	Hollow at the base of cave wall (as named by cave owners)	*Insufficient sample volume for analysis*
Entrance to Bottomless Pool	LC	(−)	Medium	Lights in proximity	Waiting area near Bottomless Pool, where guides turn off lights	*Insufficient sample volume for analysis*

Continued

Table 2. *Continued*

Fireplace	LC	(−)	High	Direct light	"Fireplace" hollow in cave wall, used as fireplace in 1800s during Civil War (as named by cave owners)	Illite$^{(m)}$, albite, calcite, microcline, TiO_2 nanoparticles in clay$^{(tr)}$
Small Chipped Out Puddle	LC	(−)	High	Indirect light	Puddle in concrete at base of stairs coming from Gilkey Room; high foot traffic has caused erosion in concrete.	Illite, microcline, calcite, quartz, dolomite, TiO_2 nanoparticles in clay$^{(tr)}$, iron oxide (appears biological)$^{(tr)}$

WC—Worley's Cave; DBC—Daniel Boone Caverns; LC—Linville Caverns.
^{m} = major component (dominant) and ^{tr} = trace component.

Principal component analyses were performed with the software PAST v. 1.81 (Hammer et al., 2001). Raw microbiology data were assessed using cluster analysis with a Bray–Curtis similarity index (Bray and Curtis, 1957), which remains a widely used coefficient in microbial ecology. Both microbiology data (phylum and class) and whole-rock geochemical data were analyzed separately using Principal Component Analysis (PCA), as PCA is the best way to visualize microbial abundance data across relatively similar sites (Ramette, 2007).

Prior to PCA, microbial data were first normalized using an arcsine transform function (commonly used for normalizing microbial abundance data). For PCA and cluster analysis of microbial communities, only the top 20 most abundant phyla and classes are included here for simplicity and image clarity, as the PCA results were nearly identical to those obtained when the entire data sets were used and therefore did not change the hypotheses outlined in the paper. The percentage of variance explained by each principal component is summarized in Table 3. PCA scores and PC loadings are provided in the Supplemental Files for the top 20 phyla/classes, as well as the entire data set.

PCA on whole-rock geochemical data was pre-processed via *Z*-score normalization to prevent the major element data from overwhelming important trace element data (and therefore masking important patterns in metal oxidation). For PCA of whole-rock geochemistry, all elemental data were used, and values that were below the detection limit were assigned a random number between zero and the detection limit.

RESULTS AND DISCUSSION

Microbiology

Phylum-level relative abundance demonstrated higher concentrations of Bacteroidota and Pseudomonadota in Linville Caverns and lower concentrations of Crenarchaeota and Methylmirabilota, whereas Daniel Boone Caverns was enriched in Thermoplasmatota, Chloroflexi, and Nitrospirota (Fig. 2). The Conch Shell site in Linville Caverns also revealed a noticeable enrichment in Cyanobacteriota, which is associated with artificial lighting. Similar trends were seen in the class abundance data (Fig. 3), where Linville Caverns had noticeably higher concentrations of Alphaproteobacteria and Bacteroidia, with lower concentrations of Methylomirabilia compared to both Worley's Cave and Daniel Boone Caverns. Both Shannon and Simpson alpha diversity indices (Fig. 4) indicate overall moderate alpha diversity across samples with high variability between samples, particularly in Linville Caverns. However, there were no obvious differences between caves for either index. Pielou's evenness and observed richness also show relatively similar patterns (Fig. 4). Kruskal–Wallis *p*-values for each metric of phylum-level community structure are all >0.15, indicating that alpha diversity is not particularly significant.

Cluster analysis (Fig. 5) of the top 20 phyla indicates that the major differences in cave microbial community structure appear to be dominated by cave-specific parameters (a combination of bedrock, soils, regional groundwater patterns, etc.), as individual caves tend to cluster together. This analysis shows an outlier group of three sites in Linville Caverns (Rock Slide Clay, Fireplace, and Small Chipped Out Puddle), which all show high to medium human foot traffic; these sites were associated with higher levels of Bacteriodota and Pseudomonadota and lower levels of Methylomirabilota than the other cave sites. Daniel Boone Caverns was particularly depleted in Pseudomonadota compared to Linville Caverns and Worley's Cave (Fig. 5), which likely represents lower anthropogenic impact. This depletion is likely due to lower visitation rates but could possibly also reflect lower amounts of allochthonous carbon from residential septic systems and/or from cattle. However, Linville Caverns has no nearby residential septic systems or cattle; so, this depletion is likely due to human visitation rather than non-point-source environmental carbon sources.

PCA of the top 20 phyla (Fig. 6) and classes (Fig. 7) more efficiently visualizes the patterns across the three cave sites and indicates that many of the cave sites reflect a combination of human traffic and cave-specific microbiomes, regardless of the amount of light or Mn oxidation. Table 3 summarizes the microbes most responsible for the variability across the sample sites, based on the PC loadings representing 95% of the variability within the microbial communities across all 21 sites (see Supplemental Tables S4 for phyla PC loadings and S5 for class loadings).

In both phyla and class data, PC1 (~51% of variance) and PC3 (~9% of variance) reflected microbes that are associated with the presence (or absence) of human traffic. Low-traffic samples were enriched in Thermoplasmatota,

Table 3. Principal component percent variance for the top 20 most abundant phyla and classes for all samples. Each principal component (PC) represents which organisms are primarily responsible for the variance across samples (loadings). When cumulative percent variance reached 95%, the loadings for additional principal components were not assessed as their contribution was negligible. Figures 5 and 6 show additional details for microbial communities for each PC.

Principal Component (PC)	Phylum % Variance (Cumulative)	Phyla Responsible for Variance	Class % Variance (Cumulative)	Classes Responsible for Variance
1	50.9 (50.9)	Bacteroidota, Pseudomonadota, Thermoproteota, Methylmirabilota	51.35 (51.35)	Bacteroidia, Alphaproteobacteria, Nitrososphaeria, Methylmirabilia
2	12.1 (63)	Methylmirabilota, Thermoplasmatota, Acidobacteriota, Cyanobacteriota	10.24 (61.59)	Methylomirabilia, Anaerolineae, Nitrospiria
3	9.5 (72.5)	Chloroflexota, Thermoproteota, Nitrospirota, Thermoplasmatota	9.1 (70.69)	Thermoplasmata, Anaerolineae, Nitrospiria, Alphaproteobacteria, Cyanophyceae
4	7.8 (80.3)	Methylmirabilota, Thermoproteota, Acidobacteriota	7.64 (78.32)	Nitrososphaeria, Vicinamibacteria
5	5.5 (85.8)	Cyanobacteria	7.26 (85.58)	Gammaproteobacteria, Blastocatellia, Thermoanaerobaculia, Thermoplasmata, Cyanophyceae
6	3.9 (89.7)	Verrucomicrobia, Cyanobacteriota, Chloroflexi, Actinomycetota	4.75 (90.33)	Cyanophyceae
7	2.5 (92.2)	Nitrospirota, Bacillota	2.13 (92.46)	Verrucomicrobiia, Polyangia, Blastocatellia
8	2.2 (94.5)	Acidobacteriota, Planctomycetota	2.05 (94.5)	Blastocatellia, Phycisphaerae, Vicinamibacteria
9	1.6 (96.1)	*Not assessed*	1.58 (96.08)	*Not assessed*
10	1.2 (97.3)	*Not assessed*	0.99 (97.07)	*Not assessed*
11	0.8 (98.1)	*Not assessed*	0.79 (97.86)	*Not assessed*
12	0.7 (98.8)	*Not assessed*	0.72 (98.58)	*Not assessed*
13	0.5 (99.3)	*Not assessed*	0.51 (99.1)	*Not assessed*
14	0.3 (99.6)	*Not assessed*	0.36 (99.46)	*Not assessed*
15	0.2 (99.8)	*Not assessed*	0.25 (99.71)	*Not assessed*
16	0.1 (99.9)	*Not assessed*	0.16 (99.87)	*Not assessed*
17	0 (100)	*Not assessed*	0.08 (99.95)	*Not assessed*
18	0 (100)	*Not assessed*	0.02 (99.98)	*Not assessed*
19	0 (100)	*Not assessed*	0.02 (100)	*Not assessed*
20	0 (100)	*Not assessed*	0 (100)	*Not assessed*

Chloroflexota, and Nitrospirota along PC3 and Thermoproteota and Methylomirabilota along PC1 (Fig. 6). Interestingly, along PC1, high-traffic samples were enriched in Bacteroidota and Pseudomonadota, two of the four human-associated phyla. Along PC2 (10%–12% of variance), the clustering pattern simply reflects cave-specific microbiomes where each cave clusters together, and the microbes responsible for the variability in PC2 are all cave/soil microbes typical of this region, as shown in Lange-Enyedi et al. (2023), Turrini et al. (2024), and Martin-Pozas et al. (2025). These are also microbes associated with clays (Chen et al., 2018) (see Table 2 for specific minerals associated with each site). None of the variance in the top 20 phyla shows any robust relationships between light levels or Mn oxidation, with the exception of Cyanobacteriota, which is next to an artificial light source in Linville Caverns.

Not surprisingly, PCA patterns for microbial class data are similar to those of the phyla data (Fig. 7); PC1 shows enrichment in Bacteroidia and Alphaproteobacteria in medium/high-traffic areas, and enrichment in Nitrososphaeria and Methylmirabilia in low-traffic areas (Fig. 6). There is more overlap in PC3 between high-traffic and low-traffic sites, but some very low-traffic areas show enrichment in Thermoplasmatota, Anaerolineae, and Nitrospiria. Several genera known to oxidize Mn were detected, including *Pseudomonas*, *Leptothrix*, and *Flavobacterium* (Carmichael et al., 2013a) as well as *Pedomicrobium* and *Caulobacter* species (Lozano and Rossi, 2012) and *Pseudoxanthamonus* (Ashassi-Sorkhabi et al., 2012). Since the process of Mn oxidation is polyphyletic and quite complex (Tebo et al., 2005, 2007; Geszvain et al., 2012; Hansel and Learman, 2016; Yu and Leadbetter, 2020), particularly in caves (Carmichael and Bräuer, 2015), it is unclear if these phyla are actually involved in Mn oxidation *in situ*.

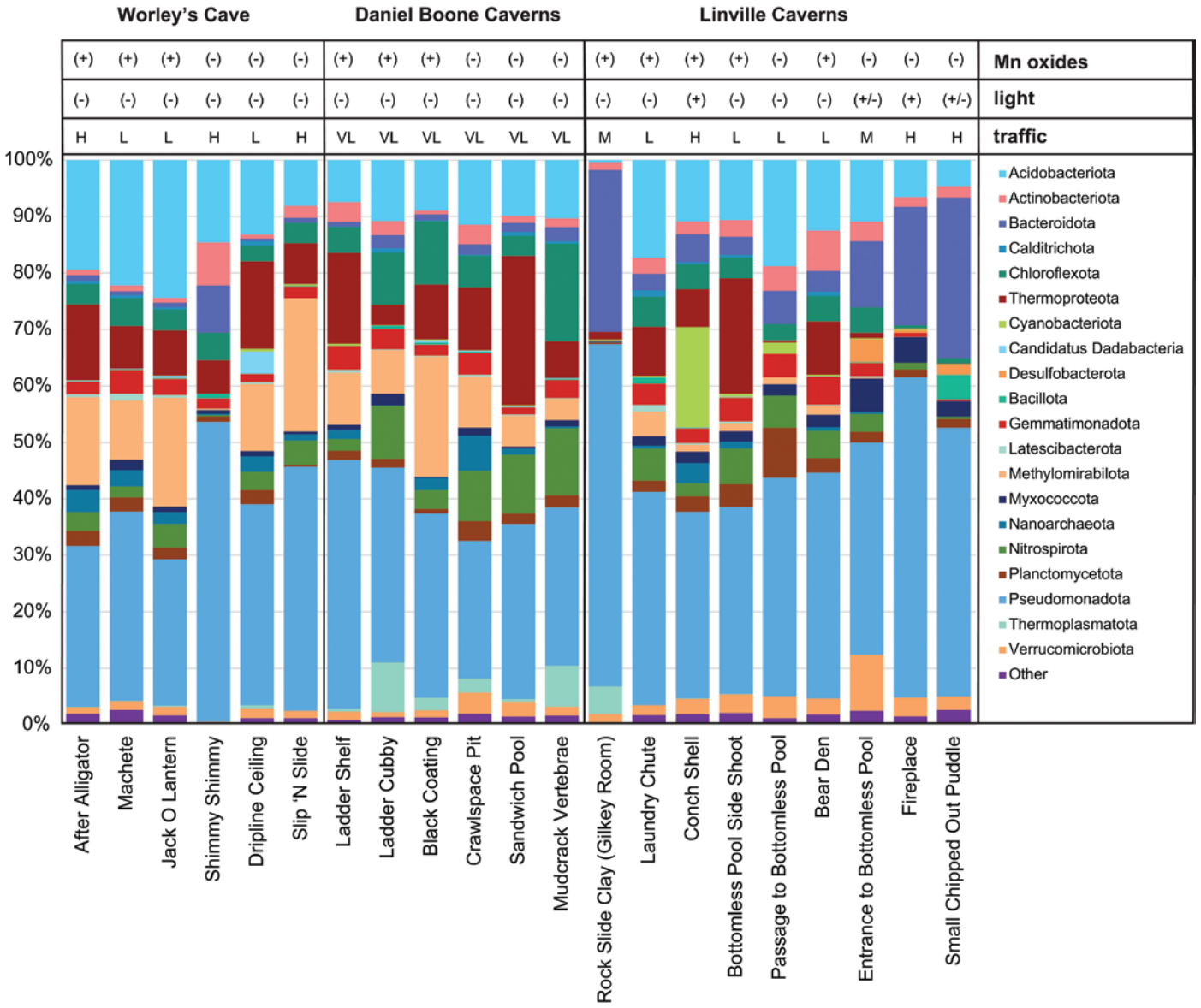


Figure 2. Phylum-level relative abundance of sequence reads across samples collected in all three caves. Manganese oxide notation of (+) indicates a positive LBB test, (−) indicates a negative LBB test. Light levels of (−) indicate no light (aside from caver headlamps or flashlights), (+/−) indicate indirect light, and (+) indicate direct light. Traffic is noted as H (high), M (medium), L (low), or VL (very low), as described in the sampling protocol.

Our microbial results align with previous research, indicating that Bacteroidota (formerly Bacteroidetes) serve as a critical signature of anthropogenic impact in cave environments. Specifically, work by Bontemps et al. (2022, 2023) demonstrates that human activity leads to the deposition of labile organic matter, which promotes a bloom of these bacteria in dark zone stains threatening Paleolithic art. Bacteroidota are characterized as copiotrophic due to their association with carbon amendment and their specialized ability to hydrolyze high-molecular weight organic matter, such as proteins, carbohydrates, and other nutrient-rich substrates (Fierer et al., 2007; Thomas et al., 2011). In particular, these "selfish" bacteria accumulate substrates like laminarin (Brown et al., 2024), while specific clusters like *Cytophaga-Flavobacter* show enrichment with chitin and protein (Cottrell and Kirchman, 2000). Our observations of increased *Chitinophagales*, *Flavobacteriales*, and *Cytophagales* within Linville Caverns sediments support these findings, as do the elevated concentrations of *Flavobacteriaceae* genera—such as *Formosa*, *Polaribacter*, *Ulvibacter*, and *Flavobacterium*—which are known to thrive when labile organic carbon is introduced (von Jackowski et al., 2022). This relationship is mirrored in preliminary microplastics data from all three caves (Riley, 2024), where Linville Caverns had far more microplastic and microfiber particles than Daniel Boone Caverns or Worley's Cave.

Additionally, artificial lighting may influence microbial composition at the Conch Shell site (the only site receiving direct light), where Cyanobacteriota were enriched relative to other sampling locations (Table 2). This was also the

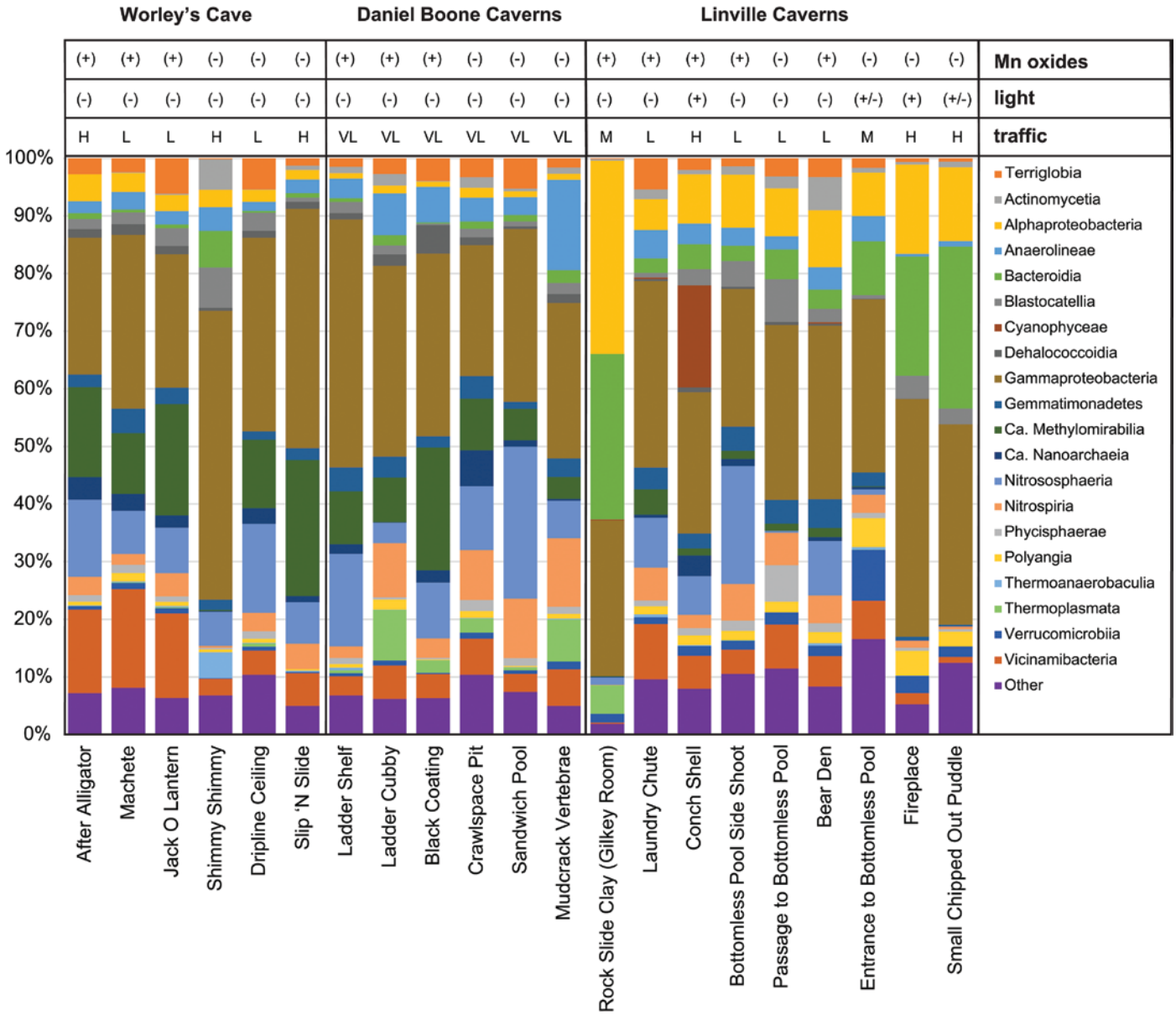


Figure 3. Class-level relative abundance of sequence reads across samples collected in all three caves. Manganese oxide notation of (+) indicates a positive LBB test, (−) indicates a negative LBB test. Light levels of (−) indicate no light (aside from caver headlamps or flashlights), (+/−) indicate indirect light, and (+) indicate direct light. Traffic is noted as H (high), M (medium), L (low), or VL (very low), as described in the sampling protocol.

only sample with a visible green patina present (Riley, 2024). Enrichment of Cyanobacteriota in cave systems via the use of artificial lighting has been documented in previous studies (Lamprinou et al., 2014; Czerwik-Marcinkowska and Massalski, 2018; Burgoyne et al., 2021), while others have noted changes in algal communities in caves due to artificial lighting (Biagioli et al., 2023).

Mineralogy and Geochemistry

X-ray diffraction of bulk sediment was combined with major, trace, and rare earth element (REE) whole-rock geochemistry data to determine the mineralogy of the sediment (Table 2). Mineral identifications were confirmed with transmission electron microscopy with energy-dispersive X-ray spectroscopy (TEM–EDS) analysis of individual sediment particles. Whole-rock geochemical data are provided in Supplemental Tables S1, S2, and S3. The sediments across the sample sites include combinations of fine silt-sized quartz and feldspar (dominantly microcline with minor albite), chlorite and illite clay, sand-sized grains of calcite and dolomite (from physical weathering of the cave walls), trace amounts of Fe oxides and Mn oxides (likely birnessite, which is the most common Mn oxide mineral in caves; see review by Carmichael and Bräuer, 2015) and TiO_2 nanoparticles.

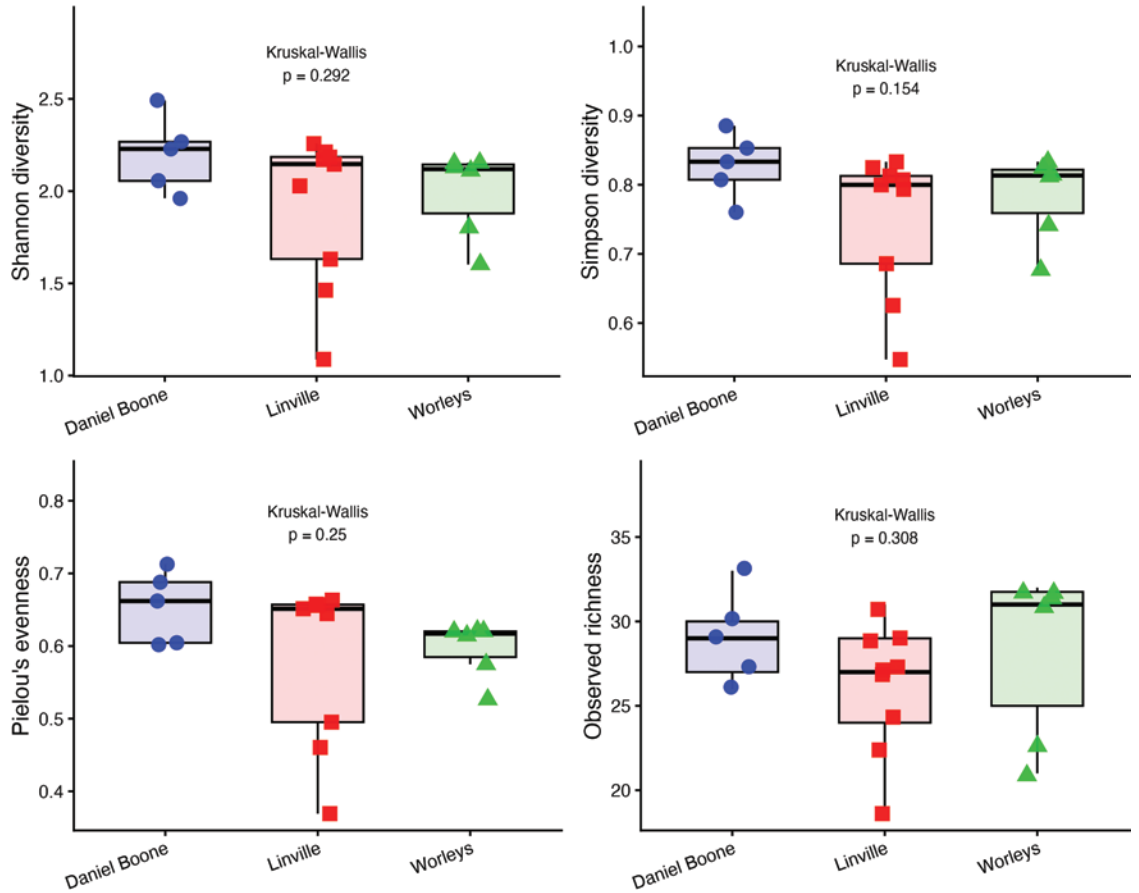


Figure 4. Alpha diversity metrices for phylum-level microbial communities between cave location. Panels show Shannon (top left) and Simpson (top right) diversities, as well as Pielou's evenness (bottom left) and observed richness (bottom right). Kruskal–Wallis *p*-values are shown within each panel.

Despite some clear indicators of anthropogenic sediment supply in TEM analysis of particles in Linville Caverns, anthropogenic particles were volumetrically insignificant compared to clay and silt particles. TiO_2 nanoparticles were present in both illite clay particles and quartz grains (Fig. 8) but did not appear to be introduced by human foot traffic even though these nanoparticles are extremely common in industrial products, sunscreen, shoe soles, etc. Soil samples taken from outside of each cave in areas where people do not walk also showed these nanoparticles in illite and quartz grains, and sediment samples from a carpet outside of the entrance to Linville Caverns did not show any unusual TiO_2 nanoparticle enrichment, so it is likely that these nanoparticles represent original mineral features from the overlying soils or from within the bedrock itself. This is not unexpected, as quartz commonly contains TiO_2 nanoparticles, particularly quartz formed during metamorphism (Ostapenko et al., 2007), and metamorphic quartz is common throughout the Proterozoic Blue Ridge basement rocks as well as the younger Paleozoic Valley and Ridge sediments of the southern Appalachians. Illite commonly contains TiO_2 nanoparticles because its crystal structure retains nanoparticles better than other types of clay minerals (Bayat et al., 2015).

Z-score transformed PCA plots of whole-rock geochemistry (Fig. 9) demonstrated that geochemical variance is mostly determined by host bedrock type combined with localized sample differences. PC1 (36% of variance) simply represents the amount of wall rock in the individual sediment sample (and is therefore not graphed), PC2 (16% of variance) represents the amount of clay minerals vs. detrital feldspars, and PC3 (12% of variance) represents the amount of detrital heavy minerals vs. Mn oxidation and phosphate (as shown in Fig. 8); 36% of the remaining variability is based on geochemical relationships that are less clear (Table 4, with specific loadings shown in Supplemental Table S6). Mn oxidation showed a weak signal in PCA but was still present in PC3 and may have correlation with an organic phosphate source.

Geochemical differences between sites that are Mn+ and Mn− show some correlations according to *t*-tests (Table 5), particularly in Linville Caverns, but PCA combined with TEM-EDS and XRD analysis gives a more coherent picture of the relationship (or lack thereof) between Mn oxidation and geochemistry. PC1, PC2, and PC3 patterns are reflected in the XRD and TEM–EDS analyses, where Linville Caverns has significantly more apatite/phosphate and clay materials

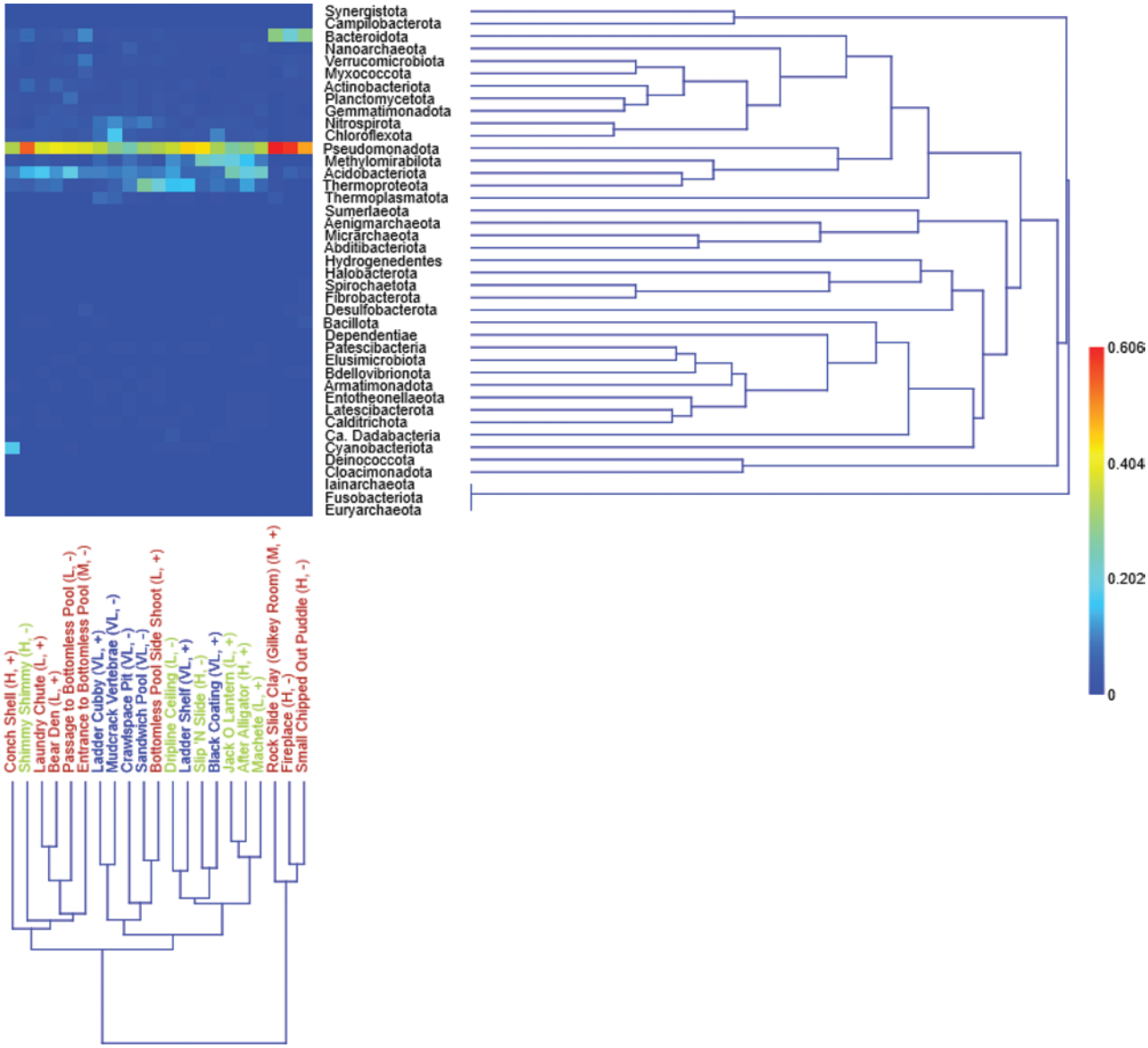


Figure 5. Two-way cluster analysis and heat map of phylum level abundance and cave groups using a Bray Curtis similarity index and raw abundance data. Worley's Cave sample locations are noted in green text, Daniel Boone Caverns in blue text, and Linville Caverns samples in red text. Traffic levels are denoted by H, M, L, and VL (high, medium, low and very low, respectively). Mn oxidation was noted as present or absent (+ or −) through Leucoberbelin Blue assays in the field. Using this similarity index, cave microbial community structure generally seems (with few exceptions) to be dominated by cave parameters (a combination of bedrock, soils, regional groundwater patterns, etc.) with an outlier group in Linville Caverns showing high-medium human foot traffic; these sites were associated with higher levels of Bacteriodota and Pseudomonadota and lower levels of Methylomirabilota than the other cave sites.

in its sediment, while Daniel Boone Caverns and Worley's Cave are enriched in quartz, feldspars, and detrital heavy minerals (Table 2). These clustering patterns likely reflect the original clastic sediments within the Knox Dolomite (hosting Worley's Cave and Daniel Boone Caverns) and the Shady Dolomite (hosting Linville Caverns), and variability within each cave likely only reflects local changes in sediment source at the time these rocks were deposited (see Mussman and Read, 1986; Montañez and Read, 1992; and Smoot and Southworth, 2014 for a more detailed sedimentological history of these rock units).

Non-metric multidimensional scaling (NMDS) combining sediment geochemistry and phylum-level community structure primarily demonstrates clustering according to cave and possibly exposure to traffic (Fig. 10). When combined with phylum data, a correlation of geochemistry with Mn oxidation (either + or −) was not present in NMDS patterns despite the *t*-test associations between Mn oxidation and (as shown in Table 5). When combined with geochemical data, correlation with traffic (recategorized as either H = high, or L = low, for better visualization) was no longer present despite being a driving factor in phylum-level data. The addition of average particle size data to NMDS analysis of geochemistry and

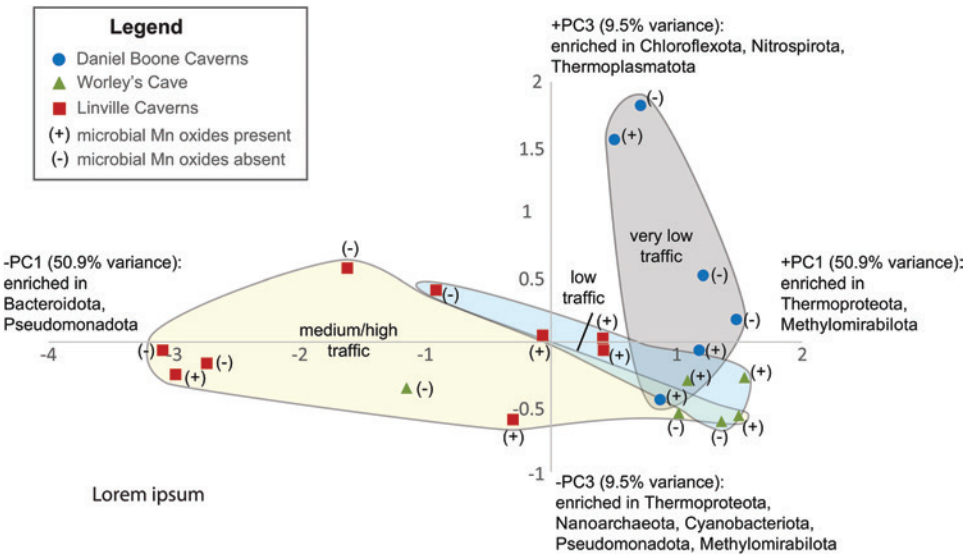


Figure 6. PCA of the top 20 most abundant phyla; samples that are more similar plot closer together, whereas samples that are more different plot farther apart. Samples from Linville Caverns are indicated by red squares, Daniel Boone Caverns by blue circles, and Worley's Cave by green triangles. There is a noticeable lack of overlap between samples classified as "high traffic," "low traffic," and "very low traffic" as defined in Table 2. Samples classified as "high traffic" have less Methylomirobilota and more Proteobacteria and Bacteriodoita than samples classified as "low traffic" and "very low traffic."

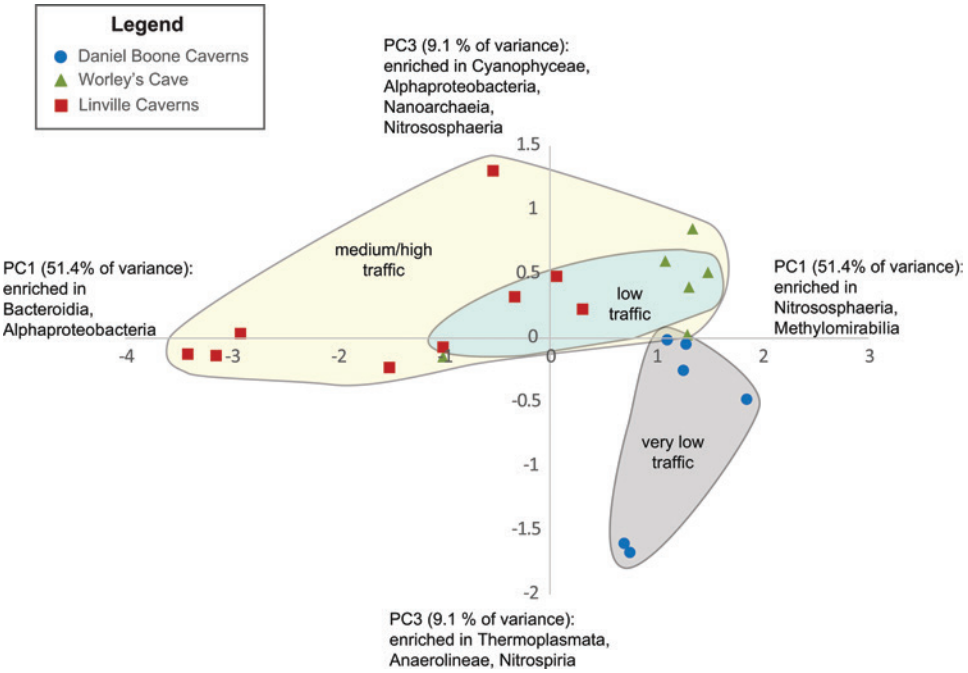


Figure 7. PCA of the top 20 most abundant classes of microbes; samples that are more similar plot closer together, whereas samples that are more different plot farther apart. Samples from Linville Caverns are indicated by red squares, Daniel Boone Caverns by blue circles, and Worley's Cave by green triangles. There is a noticeable lack of overlap between samples classified as "very low traffic" as defined in Table 2 with other traffic levels, and a trend towards enrichment in Cyanobacteriota, Bacteroidia, Alphaproteobacteria, and Nanoarchaeia as traffic levels increase.

phyla data did not change any results (Norvell, 2023), so particle size is unlikely to be a driver of microbial patterns.

PERMANOVA using Bray–Curtis dissimilarities (Table 6) assessed the independent effects of cave location and traffic intensity and showed that human traffic is associated with microbial community composition (also shown in PERDISP analysis). Cave sediment geochemistry also independently influences microbial community structure, per PERMANOVA and envfit testing. In particular, wt% Na_2O and trace elements Sr and Cs also have a strong correlation with community structure (which is also shown in the NMDS plot in Fig. 10). This relationship can be explained by the cave geochemistry, where (1) there is albite (a sodium rich feldspar) in the cave sediment fraction in Linville Caverns, and (2) there is more illite in the clay fraction of Linville Caverns sediment, and strontium preferentially sorbs to illite clays rather than chlorite clays (Fuller et al., 2016). Cesium is more complicated to interpret, because in our data it is coupled with aluminum concentrations (Supplemental Table S6). As aluminum is present in both feldspars and clays, and all of the cave sediments in this study have a mix of feldspars and clays, it is difficult to decouple which particular Al-bearing minerals are associated with Cs.

Geochemistry is clearly driving changes in microbial communities in our caves that span two distinct bedrock formations. When taken together, our results are consistent with previous studies that show how cave mineralogy (Hutchens et al., 2010; Kosznik-Kwaśnicka et al., 2022; Lange-Enyedi et al., 2023) and human visitation (Tomczyk-Żak and Zielenkiewicz, 2016) have been found to impact cave microbial communities, although cave mineralogy (or associated bedrock-related features such as groundwater and soil chemistry) appears to dominate a cave's microbiome

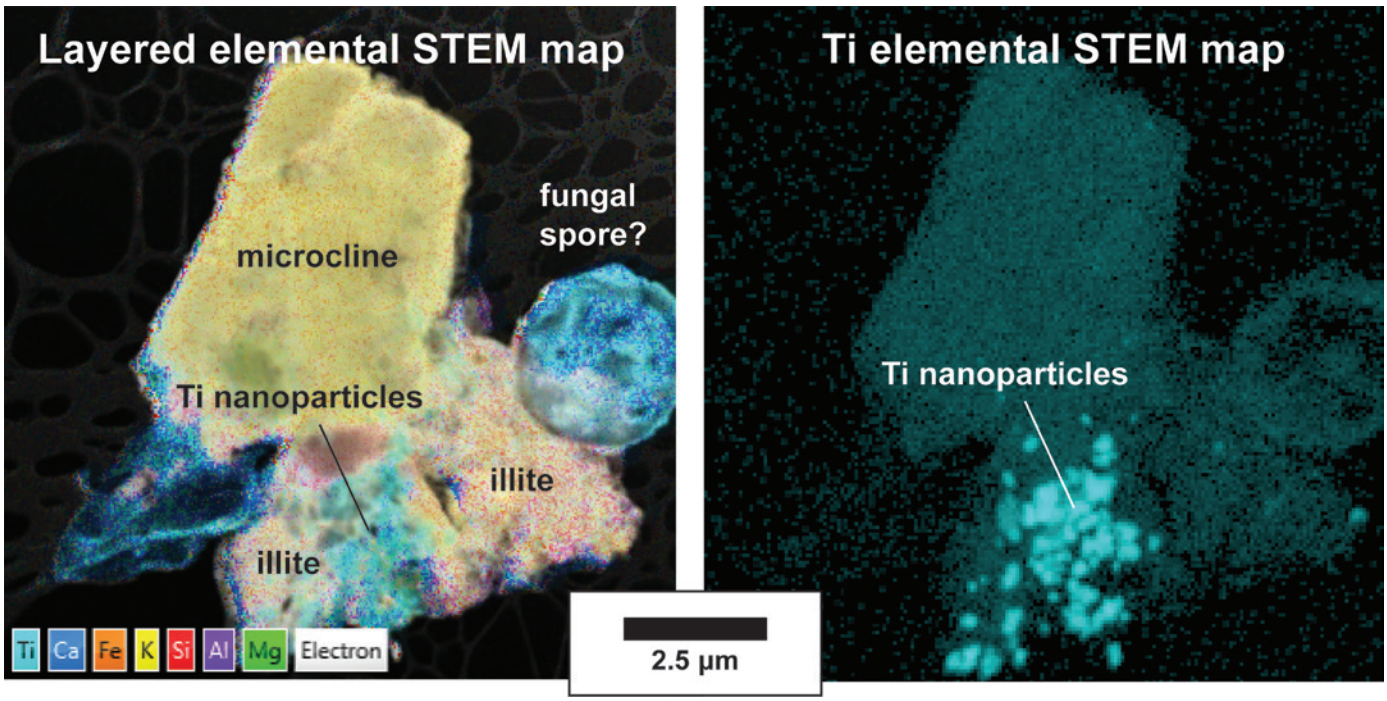


Figure 8. Scanning transmission electron microscopy (STEM) elemental map of sediment from the Rock Slide Clay in the Gilkey Room in Linville Caverns: layered elemental map is on the left, and Ti content is on the left. The round shape to the right of the image is likely a fungal spore. The area containing numerous Ti nanoparticles is a collection of illite clay grains. The larger, yellow grain is a fine silt-sized piece of microcline.

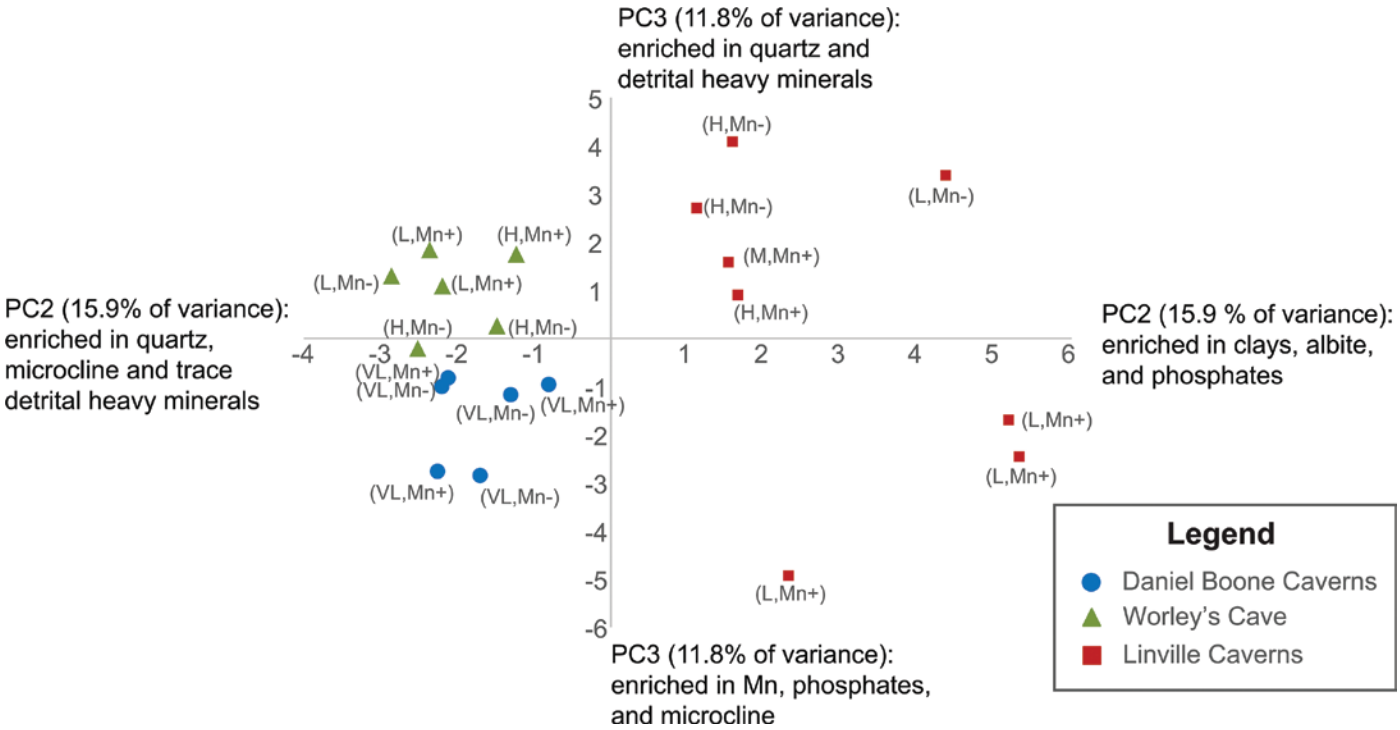


Figure 9. Z-score transformed PCA plots of whole-rock geochemistry of cave sediments using principal components 2 (PC2) and 3 (PC3); samples that are more similar plot closer together, whereas samples that are more different plot farther apart. PC1 is not shown, as it simply reflects the amount of calcite or dolomite host rock incorporated into the sediment through physical weathering of cave passages. For the purposes of this plot, whole-rock geochemistry has been translated into mineralogy based on combining geochemistry, XRD, and TEM–EDS analysis. Samples from Linville Caverns are indicated by red squares, Daniel Boone Caverns by blue circles, and Worley's Cave by green triangles. Traffic levels are denoted by H, M, L, and VL (high, medium, low and very low, respectively). The presence or absence of Mn oxidation is noted at Mn+ or Mn−. There is no obvious clustering in any sites aside from their association with the cave in which they are located, indicating that geochemistry is strongly influenced by bedrock geology.

Table 4. PCA loadings of whole-rock geochemical data (most useful principal components noted as *).

Principal Component (PC)	Geochemistry % Variance (Cumulative)	Minerals Likely Responsible for Variance
1	36.1 (36.1)	Calcite, dolomite (amount of wall rock in the sediment sample) relative to siliciclastic minerals
2*	15.9 (52)	Illite, microcline, chlorite, albite (amount and type of clay relative to the amount and type of detrital feldspars)
3*	11.8 (63.7)	Detrital heavy/refractory minerals relative to the presence of trace Mn- and P-bearing minerals (birnessite? apatite or organic phosphate?)
4	8.9 (72.6)	Weathered sulfides relative to detrital zircon?
5	6.5 (79.2)	Weathered sulfides relative to detrital zircon?
6	4.5 (83.6)	Amount of Mn oxidation?
7	3.6 (87.2)	Unknown; element combinations unclear
8	3.3 (90.5)	Unknown; element combinations unclear
9	2.3 (92.8)	*Not assessed—variance too low*
10	1.8 (94.6)	*Not assessed—variance too low*
11	1.7 (96.3)	*Not assessed—variance too low*
12	1.2 (97.5)	*Not assessed—variance too low*
13	0.8 (98.3)	*Not assessed—variance too low*
14	0.6 (98.9)	*Not assessed—variance too low*
15	0.5 (99.4)	*Not assessed—variance too low*
16	0.3 (99.8)	*Not assessed—variance too low*
17	0.1 (99.9)	*Not assessed—variance too low*
18	0.1 (100)	*Not assessed—variance too low*
19	0 (100)	*Not assessed—variance too low*

Table 5. Significant differences in major element geochemistry (elemental weight %) between Mn-positive and Mn-negative sites within each of the three caves; *p*-values for the *t*-tests are displayed.

Cave	Element	Mn+	Mn−	*p*-value
WC	C	0.58 (0.035)	0.12 (0.055)	0.001
LC	Al	1.48 (0.083)	1.19 (0.122)	0.030
LC	K	0.80 (0.039)	0.64 (0.035)	0.007
LC	Ti	0.39 (0.027)	0.32 (0.005)	0.038

Note: Data from Norvell (2023).

more so than human traffic alone (Figs. 6, 7, and 10).

SUMMARY

Cave bedrock type exerts a strong influence on sediment geochemistry (which is expected), but also on a cave's microbial community structure. The caves in this study differ by bedrock type and also by the number of annual visitors. Although it is uncertain to what degree each of these factors may be driving changes in microbial community assemblages, overall, our research shows that human visitors leave an indelible mark on cave sediments, depositing human-associated bacteria. Our data corroborate studies demonstrating that Bacteroidota are positively correlated and Nitrospirota are negatively correlated with anthropogenic input via human traffic, and that bedrock type also exerts a strong influence on sediment geochemistry and associated microbial communities within the sediment.

ACKNOWLEDGMENTS

We gratefully thank the staff at Linville Caverns for allowing sample collection and their direction throughout the various areas within the cave, John Rossi for his expertise in the field and for guiding the field team through Daniel Boone Caverns, and Milton Starnes for allowing us to collect samples from Daniel Boone Caverns. Lucca Scoggins received support from Appalachian State University's Office of Student Research and the Department of Geological and Environmental Sciences. We would like to extend an additional thanks to Lilith Hazzard for assisting with initial mineral

Table 6. Multivariate statistical analyses showing the relationships between cave location, human traffic, geochemical variables with respect to phylum-level microbial community clustering. PERMANOVA was based on Bray–Curtis dissimilarities, while marginal PERMANOVA models assessed the independent effects of cave location and traffic intensity (high or low traffic). Environmental fitting (envfit) identified geochemical drivers that were significantly related to microbial ordinations.

Test	Factor/ Variable	R^2	*F*	*p*-value	Interpretation
PERMANOVA	Traffic only	0.240	5.67	0.0025	Traffic associated with community composition
PERMANOVA	Cave (marginal)	0.245	3.81	0.0048	Cave identity independently structures communities
PERMANOVA	Traffic (marginal)	0.159	4.94	0.0054	Traffic independently influences community structure
PERMDISP	Traffic	—	8.52	0.0120	Traffic groups differ in multivariate dispersion
envfit	Na_2O	0.579	—	0.0013	Correlated with microbial community structure and feldspar type in cave sediment
envfit	Sr	0.620	—	<0.001	Strong association with NMDS structure, also correlated with clay type in cave sediment
envfit	Cs	0.339	—	0.0366	Opposes Sr/Na_2O environmental gradient

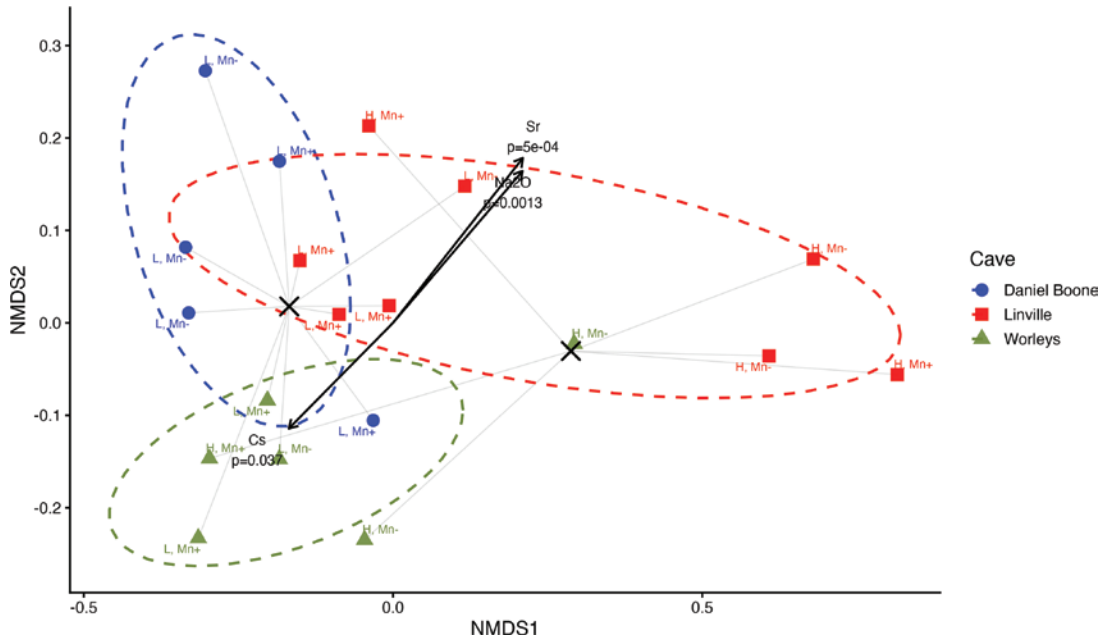


Figure 10. Non-metric multidimensional scaling (NMDS) ordination of phylum-level microbial community structure with only significant geochemical variables (black arrows) using environmental fitting (envfit) with accompanied *p*-values. Dashed ellipses show 99% confidence intervals associated with cave location. Point labels indicate human traffic intensity (H: high traffic, L: low traffic), as well as manganese oxidation status (+ or −). Stress = 0.094.

identification, and Steven J. Hageman for assistance with multivariate analyses. Partial support was provided through a Cave Conservancy Foundation grant to Suzanna Brauer, Sarah Carmichael, and Morgan Smith, and a Cave Research Foundation Graduate Research Grant awarded to Morgan Smith. Support was also provided by Appalachian State University.

SUPPLEMENTAL INFORMATION

Supplemental Tables and Figures.pdf
Phylum raw data (.xls)
Class raw data (.xls)

REFERENCES

Allaire, J., 2012, RStudio: integrated development environment for R: The R User Conference, useR!, https://posit.co/download/rstudio-desktop/.

Ashassi-Sorkhabi, H., Moradi-Haghighi, M., and Zarrini, G., 2012, The effect of *Pseudoxanthomonas* sp. as manganese oxidizing bacterium on the corrosion behavior of carbon steel: Materials Science and Engineering: C, v. 32, no. 2, p. 303–309.

Bailey, J., Adams, L., Adams, K., Holler, N., Bailey, S., Bailey, J., Cunningham, C., Shelton, E., Speer, E., Holler, C., Holler, S., and Holler, C., 1987, Map of Linville Caverns: McDowell County, NC, North Carolina Cave Survey.

Balestra, V., Vigna, B., De Costanzo, S., and Bellopede, R., 2023, Preliminary investigations of microplastic pollution in karst systems, from surface watercourses to cave waters: Journal of Contaminant Hydrology, v. 252, p. 104117.

Barton, H. A. and Jurado, V., 2007, What's up down there? Microbial diversity in caves: Microbe, v. 2, no. 3, p. 132–138.

Barton, H. A., Taylor, N. M., Kreate, M. P., Springer, A. C., Oehrle, S. A., and Bertog, J. L., 2007, The impact of host rock geochemistry on bacterial community structure in oligotrophic cave environments: International Journal of Speleology, v. 36, no. 2, p. 93–104.

Bayat, A. E., Junin, R., Mohsin, R., Hokmabadi, M., and Shamshirband, S., 2015, Influence of clay particles on Al_2O_3 and TiO_2 nanoparticles transport and retention through limestone porous media: measurements and mechanisms: Journal of Nanoparticle Research, v. 17, no. 5, p. 1–14.

Biagioli, F., Coleine, C., Piano, E., Nicolosi, G., Poli, A., Prigione, V., Zanellati, A., Varese, C., Isaia, M., and Selbmann, L., 2023, Microbial diversity and proxy species for human impact in Italian karst caves: Scientific Reports, v. 13, no. 1, p. 1–13

Blehert, D. S., Lorch, J. M., Ballmann, A. E., Cryan, P. M., and Meteyer, C. U., 2011, Bat white-nose syndrome in North America: Microbe, v. 6, p. 267–273.

Bontemps, Z., Alonso, L., Pommier, T., Hugoni, M., and Moënne-Loccoz, Y., 2022, Microbial ecology of tourist Paleolithic caves: Science of the Total Environment, v. 816, p. 151492.

Bontemps, Z., Prigent-Combaret, C., Guillmot, A., Hugoni, M., and Moënne-Loccoz, Y., 2023, Dark-zone alterations expand throughout Paleolithic Lascaux Cave despite spatial heterogeneity of the cave microbiome: Environmental Microbiome, v. 18, no. 1, p. 31.

Brannen-Donnelly, K and Engel, A. S., 2015, Bacterial diversity differences along an epigenic cave stream reveal evidence of community dynamics, succession, and stability: Frontiers in Microbiology, v. 6, p. 729.

Bray, J. R. and Curtis, J. T., 1957, An ordination of the upland forest communities of southern Wisconsin: Ecological Monographs, v. 27, no. 4, p. 325–349.

Brown, S., Lloyd, C. C., Giljan, G., Ghobrial, S., Amann, R., and Arnosti, C., 2024, Pulsed inputs of high molecular weight organic matter shift the mechanisms of substrate utilisation in marine bacterial communities: Environmental Microbiology, v. 26, no. 2, p. e16580.
Burgoyne, J., Crepeau, R., Jensen, J., Smith, H., Baker, G., and Leavitt, S. D., 2021, Lampenflora in a show cave in the Great Basin is distinct from communities on naturally lit rock surfaces in nearby wild caves: Microorganisms, v. 9, no. 6, p. 1188.
Burnham, T., Luffman, I., Whitelaw, M., and Gao, Y., Jr., 2016, Assessing structural control on groundwater flow in the Morrell Cave springshed, Sullivan County, Tennessee, in Feinberg, J. M., Gao, Y., and Alexander, E. C., eds., Caves and Karst Across Time: Geological Society of America Special Paper 516: Geological Society of America, p. 151–164, https://doi.org/10.1130/2015.2516(13).
Callahan, B. J., McMurdie, P. J., Rosen, M. J., Han, A. W., Johnson, A. J. A., and Holmes, S. P., 2016, DADA2: High-resolution sample inference from Illumina amplicon data: Nature Methods, v. 13, no. 7, p. 581–583.
Carmichael, M. J., Carmichael, S. K., Santelli, C. M., Strom, A., and Bräuer, S. L., 2013a, Mn(II)-oxidizing bacteria are environmentally relevant members of ferromanganese deposits in caves of the upper Tennessee River Basin: Geomicrobiology Journal, v. 30, no. 9, p. 779–800.
Carmichael, S. K. and Bräuer, S. L., 2015, Microbial diversity and manganese cycling: A review of Mn-oxidizing microbial cave communities, *in* Engel, A. S., ed., Microbial Life of Cave Systems, Vol. 3: Boston, MA, De Gruyter, p. 137–160.
Carmichael, S., Carmichael, M., Strom, A., Johnson, K., Roble, L., Gao, Y., and Brauer, S., 2013b, Sustained anthropogenic impact in Carter Salt Peter Cave, Carter County, Tennessee and the potential effects on Mn cycling: Journal of Cave and Karst Studies, v. 75, no. 3, p. 189–204.
Carmichael, S. K., Zorn, B. T., Santelli, C. M., Roble, L. A., Carmichael, M. J., and Bräuer, S. L., 2015, Nutrient input influences fungal community composition and size and can stimulate manganese (II) oxidation in caves: Environmental Microbiology Reports, v. 7, no. 4, p. 592–605.
Chen, C., Pan, G., Shi, W., Xu, F., Techtmann, S. M., Pfiffner, S. M., and Hazen, T. C., 2018, Clay flocculation effect on microbial community composition in water and sediment: Frontiers in Environmental Science, v. 6, no. 60, p. 1–10.
Cheng, X., Zhao, R., Bodelier, P. L., Song, Y., Yang, K., Tuovinen, O. H., and Wang, H., 2024, Differential response of subterranean microbiome to exogenous organic matter input in a cave ecosystem: Science of the Total Environment, v. 954, p. 176584.
Cigna, A. A., 2019, Show Caves: Encyclopedia of Caves: Elsevier, p. 909–921.
Cloutier, M. L., Carmichael, S. K., Carson, M. A., Madritch, M. D., and Bräuer, S. L., 2017, Carbon quantity and quality drives variation in cave microbial communities and regulates Mn(II) oxidation: Biogeochemistry, v. 134, no. 1–2, p. 77–94.
Cottrell, M. T. and Kirchman, D. L., 2000, Natural assemblages of marine proteobacteria and members of the Cytophaga-Flavobacter cluster consuming low- and high-molecular-weight dissolved organic matter: Applied and Environmental Microbiology, v. 66, no. 4, p. 1692–1697.
Czerwik-Marcinkowska, J and Massalski, A., 2018, Diversity of Cyanobacteria on Limestone Caves: Cyanobacteria: London, IntechOpen, p. 137–164.
Engel, A., 2010, Microbial diversity of cave ecosystems, *in* Barton, L. L., Mandl, M., and Loy, A., eds., *Geomicrobiology: Molecular and Environmental Perspective*: Springer Netherlands, p. 219–238, https://doi.org/10.1007/978-90-481-9204-5_10.
Faimon, J., Troppova, D., Baldik, V., and Novotny, R., 2012, Air circulation and its impact on microclimatic variables in the Cisarska Cave (Moravian Karst, Czech Republic): International Journal of Climatology, v. 32, no. 4, p. 599–623.
Fernandez-Cortes, A., Cuezva, S., Sanchez-Moral, S., Cañaveras, J. C., Porca, E., Jurado, V., Martin-Sanchez, P. M., and Saiz-Jimenez, C., 2011, Detection of human-induced environmental disturbances in a show cave: Environmental Science and Pollution Research, v. 18, no. 6, p. 1037–1045, https://doi.org/10.1007/s11356-011-0513-5.
Fierer, N., Bradford, M. A., and Jackson, R. B., 2007, Toward an ecological classification of soil bacteria: Ecology, v. 88, no. 6, p. 1354–1364.
Fuller, A. J., Shaw, S., Peacock, C. L., Trivedi, D., and Burke, I. T., 2016, EXAFS study of Sr sorption to illite, goethite, chlorite, and mixed sediment under hyperalkaline conditions: Langmuir: The ACS Journal of Surfaces and Colloids, v. 32, no. 12, p. 2937–2946.
Geszvain, K., Butterfield, C., Davis, R., Madison, A., Lee, S., Parker, D., Soldatova, A., Spiro, T., Luther, G., and Tebo, B., 2012, The molecular biogeochemistry of manganese(II) oxidation: Biochemical Society Transactions, v. 40, no. 6, p. 1244–1248.
Gillieson, D. S., 2011, Management of caves, *in* van Beynen, P., ed., Karst Management: New York, Springer, p. 141–158.
Hammer, Ø., Harper, D. A. T., and Ryan, P. D., 2001, PAST: Paleontological statistics software package for education and data analysis (version 3.12): Palaeontologia Electronica, v. 4, no. 1, p. 9.
Hansel, C. M. and Learman, D. R., 2016, The geomicrobiology of manganese: *in* Ehrlich, H. L., Newman, D. K., and Kappler, A., eds., Ehrlich's Geomicrobiology (6th edition): CRC Press, p. 401–452.
Hartmann, A., Goldscheider, N., Wagener, T., Lange, J., and Weiler, M., 2014, Karst water resources in a changing world: Review of hydrological modeling approaches: Reviews of Geophysics, v. 52, no. 3, p. 218–242.
Hasenmueller, E. A., Baraza, T., Hernandez, N. F., and Finegan, C. R., 2023, Cave sediment sequesters anthropogenic microparticles (including microplastics and modified cellulose) in subsurface environments: Science of the Total Environment, v. 893, p. 164690.
Hatcher, R. D. Jr., Lemiszki, P. J., and Whisner, J. B., 2007, Character of rigid boundaries and internal deformation of the southern Appalachian foreland fold-thrust belt, *in* Sears, J. W., Harms, T. A., and Evenchick, C. A., eds., Whence the Mountains? Inquiries into the Evolution of Orogenic Systems: A Volume in Honor of Raymond A. Price: Geological Society of America Special Paper 433, Geological Society of America, p. 243–276, https://doi.org/10.1130/2007.2433(12).
He, Y., Li, J., Li, X., Liao, J., Liang, Q., Li, H., Duan, R., Wang, C., Liu, B., Xue, Y., and Li, T., 2024, Characteristics and influencing factors of dissolved organic matter in cave drip water—a case study from Furong Cave, southwest China: Water, v. 16, no. 2, p. 207–222.
Heip, C., 1974, A new index measuring evenness: Journal of the Marine Biological Association of the United Kingdom, v. 54, no. 3, p. 555–557.
Hutchens, E., Gleeson, D., McDermott, F., Miranda-CasoLuengo, R., and Clipson, N., 2010, Meter-scale diversity of microbial communities on a weathered pegmatite granite outcrop in the Wicklow Mountains, Ireland; Evidence for mineral induced selection?: Geomicrobiology Journal, v. 27, no. 1, p. 1–14.
Kosznik-Kwaśnicka, K., Golec, P., Jaroszewicz, W., Lubomska, D., and Piechowicz, L., 2022, Into the unknown: microbial communities in caves, their role, and potential use: Microorganisms, v. 10, no. 2, p. 222.
Krumbein, W. E. and Altmann, H. J., 1973, A new method for the detection and enumeration of manganese oxidizing and reducing microorganisms: Helgoländer Wissenschaftliche Meeresuntersuchungen, v. 25, no. 2–3, p. 347–356.
Kulander, B. R. and Dean, S. L., 1986, Structure and tectonics of central and southern Appalachian valley and ridge and plateau Provinces, West Virginia and Virginia: AAPG Bulletin, v. 70, no. 11, p. 1674–1684.
Lamprinou, V., Danielidis, D. B., Pantazidou, A., Oikonomou, A., and Economou-Amilli, A., 2014, The show cave of Diros vs. wild caves of Peloponnese, Greece-distribution patterns of Cyanobacteria: International Journal of Speleology, v. 43, no. 3, p. 335–342.

Lange-Enyedi, N. T., Borsodi, A. K., Németh, P., Czuppon, G., Kovács, I., Leél-Őssy, S., Dobosy, P., Felföldi, T., Demény, A., and Makk, J., 2023, Habitat-related variability in the morphological and taxonomic diversity of microbial communities in two Hungarian epigenic karst caves: FEMS Microbiology Ecology, v. 99, no. 12, p. 1–17.

Lozano, R. P. and Rossi, C., 2012, Exceptional preservation of Mn-oxidizing microbes in cave stromatolites (El Soplao, Spain): Sedimentary Geology, v. 255–256, p. 42–55.

Ma, L., Huang, X., Wang, H., Yun, Y., Cheng, X., Liu, D., Lu, X., and Qiu, X., 2021, Microbial interactions drive distinct taxonomic and potential metabolic responses to habitats in karst cave ecosystem: Microbiology Spectrum, v. 9, no. 2, p. e01152–01121.

Martin-Pozas, T., Ghezzi, D., D'Angeli, I. M., Madonia, G., Chiarini, V., Vattano, M., De Waele, J., Cappelletti, M., Saiz-Jimenez, C., and Jurado, V., 2025, Microbial and geochemical variability in sediments and biofilms from Italian Gypsum Caves: Microbial Ecology, v. 88, no. 1, p. 1–19.

McLaren, M. R. and Callahan, B. J., 2021, Silva 138.1 prokaryotic SSU taxonomic training data formatted for DADA2 [data set]: Zenodo.

McMurdie, P. J. and Holmes, S., 2013, phyloseq: an R package for reproducible interactive analysis and graphics of microbiome census data: PLoS ONE, v. 8, no. 4, p. e61217.

Montañez, I. P. and Read, J. F., 1992, Eustatic control on early dolomitization of cyclic peritidal carbonates: evidence from the Early Ordovician Upper Knox Group, Appalachians: Geological Society of America Bulletin, v. 104, no. 7, p. 872–886.

Mulec, J and Kosi, G., 2009, Lampenflora algae and methods of growth control: Journal of Cave and Karst Studies, v. 71, p. 109–115.

Mulec, J., Pašić, L., and Oarga-Mulec, A., 2025, Metabolic traits of sediment bacteria in karst caves in the light of environmental changes: Frontiers in Microbiology, v. 16, p. 1724116.

Mussman, W and Read, J., 1986, Sedimentology and development of a passive-to-convergent-margin unconformity: Middle Ordovician Knox unconformity, Virginia Appalachians: Geological Society of America Bulletin, v. 97, no. 3, p. 282–295.

Nicolosi, G., Mammola, S., Verbrugge, L., and Isaia, M., 2023, Aliens in caves: the global dimension of biological invasions in subterranean ecosystems: Biological Reviews, v. 98, no. 3, p. 849–867.

Northup, D. E., 2011, Managing microbial communities in caves, *in* van Beynen, P., ed., Karst Management: New York, Springer, p. 225–240.

Northup, D. E., Barns, S. M., Yu, L. E., Spilde, M. N., Schelble, R. T., Dano, K. E., Crossey, L. J., Connolly, C. A., Boston, P. J., Natvig, D. O., and Dahm, C. N., 2003, Diverse microbial communities inhabiting ferromanganese deposits in Lechuguilla and Spider Caves: Environmental Microbiology, v. 5, no. 11, p. 1071–1086.

Norvell, B. G., 2023, The effects of substrate geochemistry on the distribution of manganese oxidizing bacteria in caves of the Upper Tennesee River Basin [MS thesis]: Boone, NC, Appalachian State University, 55 p.

Oksanen, J., Kindt, R., Legendre, P., O'Hara, B., Stevens, M. H. H., Oksanen, M. J., and Suggests, M., 2007, The vegan package: Community Ecology Package, v. 10, no. 719, p. 631–637.

Ostapenko, G., Tarashchan, A., and Mitsyuk, B., 2007, Rutile-quartz geothermobarometer: Geochemistry International, v. 45, no. 5, p. 506–508.

Piccardo, M and Bevilacqua, S., 2024, Lost in the dark: Current evidence and knowledge gaps about microplastic pollution in natural caves: Environments, v. 11, no. 11, p. 238–220.

Pipan, T and Culver, D., 2013, Forty years of epikarst: what biology have we learned?: International Journal of Speleology, v. 42, no. 3, p. 215–223.

Pronk, M., Goldscheider, N., and Zopfi, J., 2007, Particle-size distribution as indicator for fecal bacteria contamination of drinking water from karst springs: Environmental Science & Technology, v. 41, no. 24, p. 8400–8405.

Pronk, M., Goldscheider, N., Zopfi, J., and Zwahlen, F., 2009, Percolation and particle transport in the unsaturated zone of a karst aquifer: Groundwater, v. 47, no. 3, p. 361–369.

Ramette, A., 2007, Multivariate analyses in microbial ecology: FEMS Microbiology Ecology, v. 62, no. 2, p. 142–160.

Riley, A.-M., 2024, Human impact in Appalachian cave systems: How anthropogenic presence leads to the deposition of microplastics and alteration of native microbial cave communities [MS thesis]: Boone, NC, Appalachian State University, 53 p.

Saiz-Jimenez, C., 2012, Microbiological and environmental issues in show caves: World Journal of Microbiology and Biotechnology, v. 28, no. 7, p. 2453–2464.

Smoot, J. P. and Southworth, S., 2014, Volcanic rift margin model for the rift-to-drift setting of the late Neoproterozoic-early Cambrian eastern margin of Laurentia: Chilhowee Group of the Appalachian Blue Ridge: Geological Society of America Bulletin, v. 126, no. 1–2, p. 201–218.

Tebo, B. M., Clement, B. G., and Dick, G. J., 2007, Biotransformations of manganese, *in* Hurst, C. J., Crawford, R. L., Garland, J. L., Lipson, D. A., Mills, A. L., and Stetzenbach, L. D., eds., Manual of Environmental Microbiology: Washington, DC, ASM Press, p. 1223–1238.

Tebo, B. M., Johnson, H. A., McCarthy, J. K., and Templeton, A. S., 2005, Geomicrobiology of manganese(II) oxidation: Trends in Microbiology, v. 13, no. 9, p. 421–428.

Thigpen, J. R., Moecher, D. P., Stowell, H. H., Merschat, A., Hatcher, R. D., Jr, Powell, N. E., Spencer, B. M., Mako, C. A., Bollen, E. M., and Kylander-Clark, A., 2022, Defining the timing, extent, and conditions of Paleozoic metamorphism in the southern Appalachian Blue Ridge terranes of Tennessee, North Carolina, and northern Georgia: Tectonics, v. 41, no. 10, p. e2022TC007406.

Thomas, F., Hehemann, J.-H., Rebuffet, E., Czjzek, M., and Michel, G., 2011, Environmental and gut bacteroidetes: the food connection: Frontiers in Microbiology, v. 2, p. 93.

Tomczyk-Żak, K and Zielenkiewicz, U., 2016, Microbial diversity in caves: Geomicrobiology Journal, v. 33, no. 1, p. 20–38.

Turrini, P., Chebbi, A., Riggio, F. P., and Visca, P., 2024, The geomicrobiology of limestone, sulfuric acid speleogenetic, and volcanic caves: basic concepts and future perspectives: Frontiers in Microbiology, v. 15, p. 1370520.

Virginia Division of Mineral Resources, 1993, Geologic Map of Virginia: Virginia Division of Mineral Resources, scale 1:500,000: Association of American State Geologists.

von Jackowski, A., Becker, K. W., Wietz, M., Bienhold, C., Zäncker, B., Nöthig, E. M., and Engel, A., 2022, Variations of microbial communities and substrate regimes in the eastern Fram Strait between summer and fall: Environmental Microbiology, v. 24, no. 9, p. 4124–4136.

Wickham, H., 2011, ggplot2: WIREs Computational Statistics, v. 3, no. 2, p. 180–185.

Yu, H and Leadbetter, J. R., 2020, Bacterial chemolithoautotrophy via manganese oxidation: Nature, v. 583, no. 7816, p. 453–458.

Zhong, L., Deng, J., Song, Z., and Ding, P., 2011, Research on environmental impacts of tourism in China: Progress and prospect: Journal of Environmental Management, v. 92, no. 11, p. 2972–2983.

Dhanusha Kawalkar, Priyanka Desai, Rima Sadhukhan, Pooja Patil, and Shirish Manchi. Herpetofauna in the caves of the Andaman Islands: An appeal for conservation measures. *Journal of Cave and Karst Studies*, v. 88, no. 3, p. 62-71. DOI: 10.4311/2025LSC0121

HERPETOFAUNA IN THE CAVES OF THE ANDAMAN ISLANDS: AN APPEAL FOR CONSERVATION MEASURES

Dhanusha Kawalkar[1], Priyanka Desai[2], Rima Sadhukhan[1], Pooja Patil[1], and Shirish Manchi[1,C]

Abstract

As incidental inhabitants, amphibians and reptiles actively exploit subterranean ecosystems. In the Indian context, knowledge of cave-dwelling herpetofauna is scarce. This paper compiles information about the amphibians and reptiles encountered during multiple visits to the caves of the most significant cave complexes of the Andaman Islands on Baratang Island, Chalis-Ek on North Andaman Island, and Interview Island in the North and Middle Andaman Islands between 2018 and 2020, and 2024 and 2025. We encountered herpetofauna in all cave zones and added 14 species to the existing list of cave-dwelling herpetofauna. We reported four species of amphibians and twelve species of reptiles actively using the cave for roosting or foraging. Of the reported species, four amphibians; three (Chakrapani's narrow-mouthed Frog, Andaman wart frog, and Andaman bush toad) are endemic to the Andaman Islands. Among reptiles, three species are endemic to the Andaman Islands (Andaman Grass Skink, Andaman Bent-toed Gecko, and Anderson's Pit Viper), and the Nicobar Forest Dragon is distributed across the Andaman and Nicobar Islands. The study reports the presence of herpetofauna within the tropical caves of the Andaman Islands and highlights the importance of subterranean habitats for their conservation. Further detailed studies are recommended to understand habitat usage and behavior of herpetofauna within cave ecosystems.

INTRODUCTION

Amphibians and reptiles, collectively known as herpetofauna, serve as key indicator taxa for assessing habitat alteration and climate change globally (Sheridan and Olson, 2003; Olson and Saenz, 2013). Their sensitivity to environmental changes has precipitated an unprecedented decline in their populations (Harikrishnan et al., 2022). This is particularly severe on islands, where populations are at high risk of extinction due to limited distribution ranges and the presence of invasive species (Harikrishnan et al., 2022).

In light of these challenges in terrestrial habitats, subterranean environments offer essential refuge for many species from natural and anthropogenic disturbances (Biswas, 2014). Subterranean habitats serve multiple functions, including providing thermal protection (Uhrin and Lesinsky, 1997; Fenolio et al., 2005), providing shelter to evade predation (Manenti et al., 2009), serving as feeding habitats (Baumgart, 1981; Uhrin and Lesinsky, 1997), and acting as breeding grounds (Culver and Pipan, 2019). Several studies have documented all three living orders within the class Amphibia in cave habitats: Anura (frogs and toads), Caudata (salamanders), and Gymnophiona (caecilians) (Bonini et al., 1999; Bressi and Dolce, 1999; Biswas et al., 2011). In the Palearctic and Neotropical regions, amphibians are relatively prevalent in caves (Rosa and Penado, 2013); however, cave salamanders have commonly been the focus of scientific explorations (Sequeira et al., 2001; Kami, 2004; Lanza et al., 2006; Romero, 2009; Ianc et al., 2012). Previously, Olm *Proteus anguinus* Laurenti, 1768, was the only known obligate cave-dweller. However, based on Recknagel and Trontelj (2022), 14 cave-obligate species, all plethodontid and proteid salamanders, are known, and 11 salamander species or subspecies exhibit troglomorphism (Romero, 2009).

Reptiles also significantly utilize cave habitats (Gunn, 2004; Manchi and Sankaran, 2009; Pauwels et al., 2019). Of the four reptile orders, Squamata (snakes and lizards) (Pauwels et al., 2019), Testudines (turtles) (Milstead, 1956; Acuña-Mesen, 1994; Tuberville et al., 2005; Kawalkar et al., 2024), and Crocodilia (crocodiles) (Somaweera et al., 2020; Wynne et al., 2023) have been documented utilizing caves. Many of these taxa have been recorded using these caves as feeding grounds (Gunn, 2004; Manchi and Sankaran, 2009; Shirley et al., 2017)

Though herpetofauna are known to inhabit caves worldwide, little is known about India's cave-dwelling species, apart from sporadic reports of their occurrence (supplementary material). While exploring the limestone caves in the Andaman Islands between 2018 and 2020, and again in 2024 and 2025, we encountered 16 species of amphibians and reptiles. This document discusses the occurrence of herpetofauna in caves of the Andaman Islands and highlights the significance of these subterranean habitats with a brief review of the existing related knowledge.

[1]Division of Conservation Ecology, Sálim Ali Centre for Ornithology and Natural History, Anaikatty Post (South India Centre of Wildlife Institute of India), Coimbatore, Tamil Nadu 641 108, India
[2]Bharati Vidyapeeth (Deemed to be University), Institute of Environment Education & Research (BVIEER), Katraj, Pune, Maharashtra 411 043, India
[C]Corresponding author: ediblenest@gmail.com.

METHODS

Study Area

The Andaman and Nicobar Islands (10°14′20.40″ N, 93°13′48.00″ E, Fig. 1) are an island archipelago that extends into the Bay of Bengal (Andrews and Sankaran, 2002). These islands are a part of both the Indo-Burma and Sundaland biodiversity hotspots (Myers et al., 2000). The Andaman and Nicobar Islands experience a tropical to subtropical climate, characterized by humidity levels of 79%–89% and temperatures ranging from 21 to 33 °C (Saldanha, 1989; Rajendran et al., 2008). Due to the northeast and southwest monsoon, these islands receive substantial (300–350 cm) rainfall annually (Chakravarthy et al., 1987).

About 395 caves are known from 37 islands in the Andaman Nicobar Archipelago (Sankaran, 1998; Manchi and Sankaran, 2014). The random visual encounters of the herpetofauna (reptiles and amphibians) discussed here are from the archipelago's most significant cave complexes: Wraffter's Creek on Baratang Island, Interview Island, and Chalis-Ek on North Andaman Island. Baratang Island (12°05′ N, 92°45′E) features more than 175 caves spread across 0.77 km^2 (Sankaran, 2001; Manchi and Sankaran, 2014), with a unique karst forest (Mane et al., 2019), primarily dominated by calciphiles, comprising Andaman tropical evergreen and Andaman semi-evergreen forests (Champion and Seth, 2005). Chalis-Ek on North Andaman Island is a limestone hillock with 28 caves. Pal and Bhattacharya (2010) provided a detailed account of the metamorphic rocks belonging to the ophiolite series. Champion and Seth (2005) classified the vegetation of North Andaman into Andaman tropical evergreen, Andaman semi-evergreen, Andaman moist deciduous, mangroves, and littoral forest. Interview Island (12°56′17″ N and 92°42′31″ E) is the westernmost simple carbonate island (Kawalkar and Manchi, 2020). It has 34 known limestone caves and is the largest Wildlife Sanctuary (133.40 km^2) in the archipelago (Manchi and Sankaran, 2014; Vijayamma et al., 2021). Interview Island belongs to the Archipelago series, composed of soft limestone formed from coral and shell, soft calcareous sandstones, and soft white clays, with occasional bands of conglomerates (Oldham, 1885).

The fauna of the Andaman Islands exhibits affinities with the South-East Asian fauna, with some species restricted to a few islands in the archipelago (Rahmani et al., 2016). India is home to approximately 472 amphibian species, of which around half are endemic (Gosavi et al., 2020). In these islands, both amphibians and reptiles are distinct, with 21 species of amphibians (Harikrishnan and Vasudevan, 2018; Garg et al., 2022b) and 76 reptile species, of which 24 are endemic (https://forest.and.nic.in/).

Data Collection

The surveys were conducted between 2018 and 2020 and again between 2024 and 2025. We used a visual encounter survey (dos Santos et al., 2022), where three observers recorded the presence of herpetofauna across different parts of the caves. While surveying, we observed the animal's location (walls, floor, speleothems, etc.), behavior (e.g., roosting, feeding, and mating), cave zone (entrance, twilight, and dark), and the types of microhabitats (leaf litter, guano, crevices, etc.). We photographed the animals for further identification.

RESULTS

The present study adds 14 species (Fig. 2) to the existing list of 29 herpetofauna species reported from caves in India (supplementary material). During the present study, we recorded four amphibian and 12 reptile species from caves at Chalis-Ek, Baratang Island, and Interview Island (Fig. 3). The herpetofauna were recorded across the various microhabitats within caves for foraging and roosting (Table 1). Among the study sites, species diversity was highest in the caves at Baratang Island, followed by Chalis-Ek and Interview Island.

We recorded anurans from three families (Bufonidae, Microhylidae, and Dicroglossidae), further classified into four genera (*Duttaphrynus*, *Blythophryne*, *Microhyla*, and *Minervarya*) (Fig. 4). The Common Asian Toad (*Duttaphrynus melanostictus*), Andaman Bush Toad (*Blythophryne beryet*), Chakrapani's Narrow-mouthed Frog (*Microhyla chakrapanii*), and Andaman Wart Frog (*Minervarya cf. andamanensis*) (Fig. 5).

Among squamates, we recorded species from four families (Gekkonidae, Agamidae, Scincidae, and Varanidae), further classified into eight genera (Cyrtodactylus, Hemidactylus, Coryphophylax, Calotes, Sphenomorphus, Eutropis, Subdoluseps, and Varanus) (Fig. 6). The species observed were the Andaman Bent-toed Gecko (*Cyrtodactylus rubidus*), Flat-tailed House Gecko (*Hemidactylus platyurus*), Nicobar Forest Dragon (*Coryphophylax subcristatus*), Changeable Lizard (*Calotes versicolor*), Spotted Forest Skink (*Sphenomorphus maculatus*), Andaman Grass Skink (*Eutropis andamanensis*), Christmas Island Grass skink (*Subdoluseps bowringii*), and Common Water Monitor (*Varanus salvator*) (Fig. 6). Additionally, we recorded snakes from three families (Viperidae and Colubridae), including four genera (Trimeresurus, Gonyosoma, Lycodon, and Coelognathus). The species observed were Anderson's Pit Viper (*Trimeresurus andersonii*), Red-tailed Racer (*Gonyosoma oxycephalum*), Andaman Wolf Snake (*Lycodon hypsirhinoides*), and Yellow-striped Trinket Snake (*Coelognathus flavolineatus*) (Fig. 7).

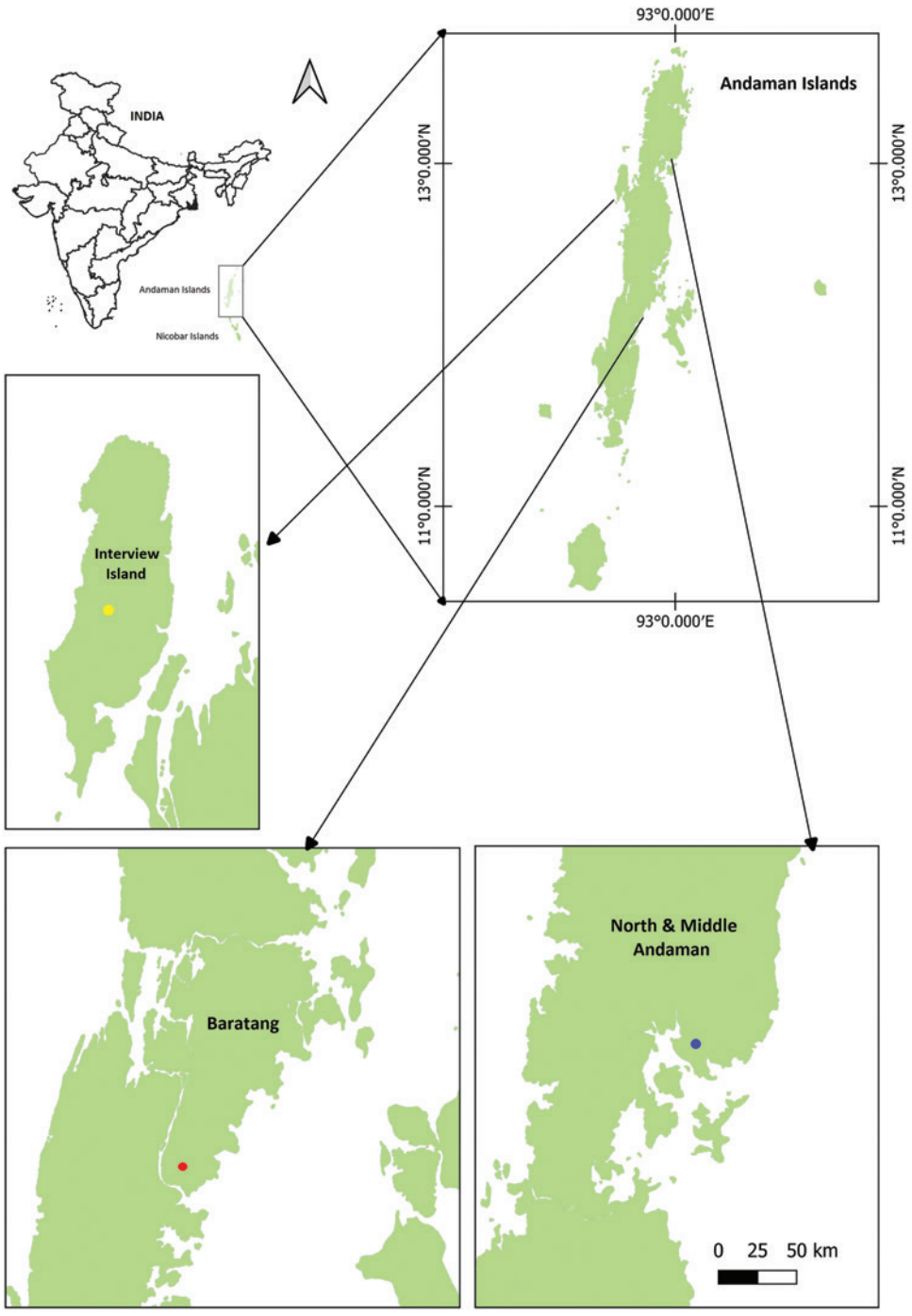


Figure 1. The geographical location of Baratang, Interview Island, and North Andaman (Chalis-Ek) Islands.

DISCUSSION

Amphibians and reptiles use caves with different rock types and environments; however, their ecological reasons are still scarcely explored (dos Santos et al., 2022). Similarly, the present study also recorded herpetofauna across various cave microhabitats for breeding, roosting, and foraging activities. Five amphibian and twelve reptile species were observed actively using the limestone caves in the Andaman Islands. Among amphibians, the common Asian toad, a widely distributed species across diverse habitats (Dutta et al., 2009), was first recorded in a subterranean habitat of the Siju Cave, Meghalaya (Sinha, 1999). Hence, its presence inside the caves of the Andaman Islands is apparent. Biswas et al. (2011) encountered this species in caves during the rainy seasons. Though we did not observe any breeding activity, finding it in the same places on repeated visits suggests they return to these spots regularly, using the caves as safe places for shelter, food, and maybe breeding.

The Andaman Bush Toad (Chandramouli et al., 2016) is another species recorded in the caves of Baratang Island. We encountered the species under the leaf litter in the cave entrance zone during February–March and November. In the twilight zone, the species was seen roosting in crevices of the cave wall, speleothems, and on the cave floor. Similarly, a species of arboreal toad, *Sigalegalephrynus mandailinguensis*, in Indonesia is documented to use both troglodytic and arboreal habitats, at 2 m above the cave floor (Smart et al., 2017). Hence, detailed cave exploration as a significant habitat for toads is vital. Moreover, the Andaman Bush Toad, which is "vulnerable" with a severely fragmented population in the islands (IUCN, 2023), requires an urgent, detailed understanding of its presence in cave habitats to develop conservation measures.

The presence of toads and frogs is considered incidental and common in the subterranean environments (Bressi and Dolce, 1999; Lunghi et al., 2018). Among the frogs observed are the Andaman Wart Frog (*Minervarya cf. andamanensis*) by Garg et al. (2022a) and Chakrapani's Narrow-mouthed Frog (*Microhyla chakrapanii*). The Andaman Wart Frog was observed in microhabitats such as crevices, eroded walls, bat or swiftlet guano deposits, soil, leaf litter, and areas where organic debris washed in from sinkholes during the monsoon (April–July). The occurrence of both species in the moist

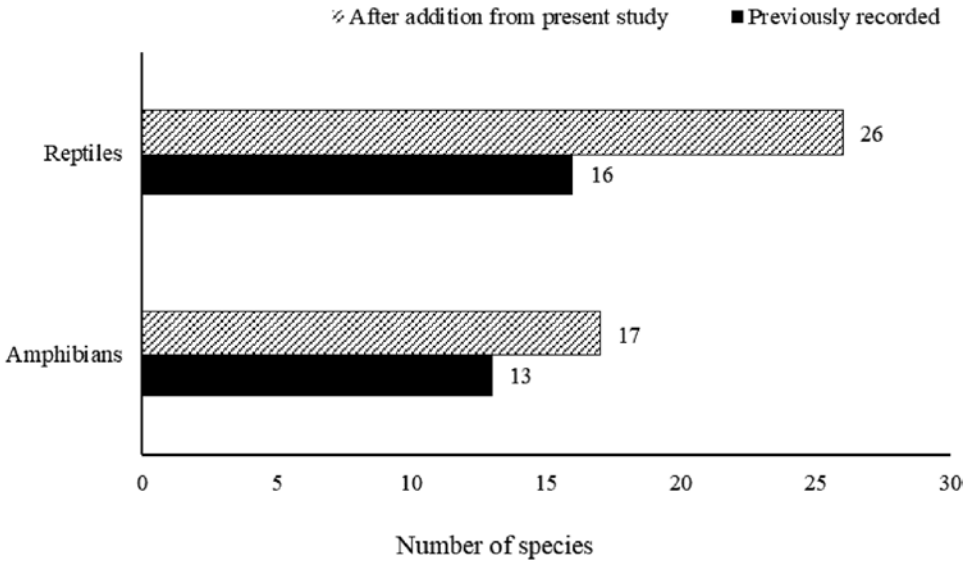


Figure 2. Comparative overview of India's cave-dwelling herpetofauna, showing species previously known from caves and those newly documented through the present surveys.

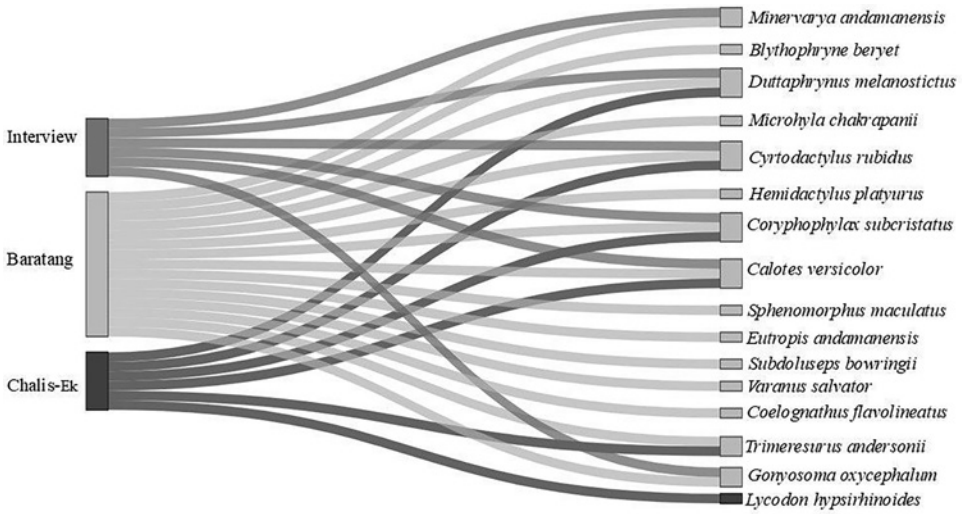


Figure 3. The presence of herpetofauna species across the study sites.

twilight and dark zones adds a new dimension to their ecological range, indicating a wider habitat plasticity than previously documented. Further detailed studies will help in understanding the habitat requirements and ecology of these frogs in caves.

Reptiles utilize various cave microhabitats (e.g., cave walls, crevices, and groundwater) for roosting and foraging (Poulton, 2004; Maglangit et al., 2021). We encountered several species of snakes. Both the Anderson's Pit Viper and the Red-tailed Racer were observed from the entrance zone to deep inside the caves, mostly beneath colonies of bats and swiftlets. At the entrances, they exhibit a sit-and-wait hunting posture. Inside the caves, they were observed under active bat roosts and swiftlet nests, likely waiting to ambush prey. Additionally, a Yellow-striped Trinket snake and an Andaman Wolf Snake were observed in the holes on the cave floor, suggesting that caves also serve as temporary refuges for these species. According to Turbanov et al. (2019), snakes occupy both inland and coastal caves and are usually observed using clastic sediments (small extraneous debris, fallen rocks, and boulders) in all three zones.

Snakes are recognized predators of lizards and geckos in terrestrial habitats (Landová et al., 2016); this trophic interaction is now also confirmed within the cave ecosystems of the Andaman Islands. We encountered geckos and lizards in a variety of microhabitats (walls, ceiling, and floor, including speleothems, cracks, and crevices) throughout the cave. The Andaman Bent-toed Gecko, a ground-dwelling species, is vespertine (active at dusk) and often found in the lower parts of the trunks of native trees (Mohan et al., 2020). We encountered this species between April and July in the dark parts of various cave zones, specifically in cracks and crevices on the walls. Not much is known about the species' breeding season. However, members of *Cyrtodactylus* in Malaysia are known to breed until April (Quah et al., 2021), which may also be the case with the Andaman Bent-toed Gecko. We encountered gecko eggs adhering to the crevices of the cave walls and to the dry parts of the stalagmites. However, we did not find any hatchlings or juveniles in the cave, and we are not certain about the species of the eggs encountered. Mostly, the isolated individuals were encountered. Only in one cave did we record five geckos together in the twilight zone.

Besides the Andaman Bent-toed Gecko, only the Flat-tailed House Gecko was seen on two separate occasions in a cave on Baratang Island. This species has an extensive geographic distribution, with its range centered in Southeast Asia (Mahony and Ali Reza, 2007). It has also been reported from the Andaman and Nicobar Islands. While primarily considered synanthropic species, there are growing reports of *Hemidactylus* species utilizing subterranean habitats across their range. For example, in the Zagros Mountains of Iran, multiple *Hemidactylus* species, including *H. persicus*, have been documented

Table 1. Herpetofauna recorded from the caves of North and Middle Andaman Islands.

Sr. No.	Species Name	IUCN Global Assessment	Wildlife Protection Act, 1972 Status	Study Sites			Zone	Micro-habitat	Activity	Endemicity	Abundance/ Population Trend (Based on IUCN Red List)
				Baratang Island	Interview Island	Chalis-Ek					
				Family: Bufonidae							
1	Common Asian toad (*Duttaphrynus melanostictus*)	Least concern	Not mentioned	✓	✓	✓	Entrance twilight dark	Speleothems, Bat and Bird guano	R, F	Non-endemic	Common/ stable
2	Andaman bush toad (*Blythophryne beryet*)	Vulnerable	Not mentioned	✓	X	X	Entrance twilight	Leaf litter, Boulder	R	Endemic	Common/ stable
				Family: Dicroglossidae							
3	Andaman wart frog (*Minervarya andamanensis*)	Least concern	Not mentioned	✓	✓	X	Dark	Cave wall/rock	R	Endemic	Common/ stable
				Family: Microhylidae							
4	Chakrapani's narrow-mouthed frog (*Microhyla chakrapanii*)	Least concern	Not mentioned	✓	X	X	Dark	Speleothems with flowing water	R	Endemic	Stable
				Reptiles							
				Family: Gekkonidae							
5	Andaman bent-toed gecko (*Cyrtodactylus rubidus*)	Least concern	Not mentioned	✓	✓	✓	Twilight dark	Crevices, Speleothems	R	Endemic	Common/ stable
6	Flat-tailed house gecko (*Hemidactylus platyurus*)	Least concern	Not mentioned	✓	X	X	Dark	Crevices, walls and speleothems	R	Non-endemic	Increasing
				Family: Agamidae							
7	Nicobar forest dragon (*Coryphophylax subcristatus*)	Least concern	Not mentioned	✓	✓	✓	Entrance	Cave floor	R, F	Endemic	Common/ stable
8	Changeable lizard (*Calotes versicolor*)	Least concern	Not mentioned	✓	✓	✓	Entrance	Cave floor	R, F	Non-endemic	Common/ stable
				Family: Scincidae							
9	Spotted forest skink (*Sphenomorphus maculatus*)	Least concern	Not mentioned	✓	X	X	Twilight dark	Speleothem	R	Non-endemic	Common/ stable
10	Andaman grass skink (*Eutropis andamanensis*)	Least concern	Not mentioned	✓	X	X	Twilight	Leaf litter, fallen branches, rock debris	R	Endemic	Stable
11	Christmas Island grass-skink (*Subdoluseps bowringii*)	Least concerned	Not mentioned	✓	X	X	Twilight	Leaf litter, fallen branches, rock debris	R	Non-endemic	Stable

Continued

Table 2. *Continued*

					Family: Varanidae							
12	Water monitor lizard (*Varanus salvator*)		Schedule I	✓	X	X	Twilight, Entrance	NA	F	Subspecies-Endemic	Common/unknown
					Family: Viperidae							
13	Anderson's pit viper (*Trimeresurus andersonii*)	Least concern	Schedule II	✓	X	✓	Entrance	Crevice	R, F	Endemic	Common/stable
					Family: Colubridae							
14	Red-tailed racer (*Gonyosoma oxycephalum*)	Least concern	Not mentioned	✓	✓	X	Entrance, twilight	Cave wall	F, R	Non-endemic	Common/decreasing
15	Andaman wolf snake (*Lycodon hypsirhinoides*)	Least concern	Not mentioned	X	X	✓	Entrance	Cave wall/rock	R	Endemic	Common/unknown
16	Yellow-striped trinket snake (*Coelognathus flavolineatus*)	Least concern	Not mentioned	✓	X	X	Dark	Crevice	R	Non-endemic	Stable

Figure 4. Amphibian species recorded from limestone caves of the Andaman Islands: (a) Common Asian toad (*Duttaphrynus melanostictus*), (b) Andaman bush toad (*Blythophryne beryet*), and (c) Chakrapani's narrow-mouthed frog (*Microhyla chakrapanii*).

within 15 different caves alongside other cave-adapted geckonids and phyllodactylids, emphasizing the genus's ecological flexibility and tendency to exploit sheltered cave-like environments (Esmaeili-Rineh et al., 2016). Similarly, cave-associated populations of *H. lemurinus* have been recorded in coastal cliff habitats such as the "Marneef Cave" in Dhofar, Oman, where individuals were observed using rock crevices and moist cavities influenced by marine spray, reinforcing their adaptation to dim, humid environments that mimic subterranean conditions (Quah et al., 2021). Although the flat-tailed house gecko is not generally considered a troglophile, its presence in the caves of Baratang Island suggests occasional subterranean refuge-seeking behavior, likely driven by humidity, prey availability, or microclimatic stability.

Among the Agamidae, the Nicobar Forest Dragon and the Changeable Lizard are often sighted in the entrance and twilight zones of the caves on Baratang Island. These sympatric species are generally arboreal and occur primarily in the rainforest. The Nicobar Forest Dragon is abundant on the islands and comprises the major lizard biomass in the rainforest (Harikrishnan et al., 2012). In the Philippines, lizards are documented to use cave habitats for breeding, foraging, and roosting (Maglangit et al., 2021). However, we did not record lizards breeding in the caves in the Andaman Islands, but it is probable. Detailed exploration is required to determine whether the lizards use the cave habitats for breeding.

A camera trap captured a Common Water Monitor lizard repeatedly visiting a cave over three days, and browsing, indicating the occasional use of subterranean habitats for foraging or refuge. This was the only observation of the family Varanidae made during this study. Other parts of Southeast Asia, such as Batu Caves, have documented the water monitor and four other lizard species using subterranean habitats (Teo et al., 2023).



Figure 5. Morphs of *Minervarya cf. andamanensis* observed during field surveys in the Andaman Islands. The morphs shown represent only a subset of the species' phenotypic variation.



Figure 6. Squamate reptiles recorded from limestone caves of the Andaman Islands: (a) Andaman bent-toed gecko (*Cyrtodactylus rubidus*), (b) Nicobar forest dragon (*Coryphophylax subcristatus*), (c) Changeable lizard (*Calotes versicolor*), (d) Spotted forest skink (*Sphenomorphus maculatus*), (e) Andaman grass skink (*Eutropis andamanensis*), and (f) Common water monitor lizard (*Varanus salvator andamanensis*).

The Spotted Forest Skink was observed in the entrance and twilight zones, crawling on various features within the limestone caves on Baratang Island. Later, between 2024 and 2025, the Andaman Grass Skink and Christmas Island Grass Skink were encountered in the Baratang caves. They were observed in the entrance and twilight zones amid leaf litter, broken twigs, and fallen branches. In the Hinophopan Cave in the Philippines (Maglangit et al., 2021), skinks were seen actively foraging inside caves. They were observed feeding on ants, crickets, and small arthropods near the entrance and twilight zone, and they often basked at the cave's opening (Maglangit et al., 2021).

CONCLUSION

This study is the first attempt to document the occurrence of herpetofauna in the limestone caves of the Andaman Islands.

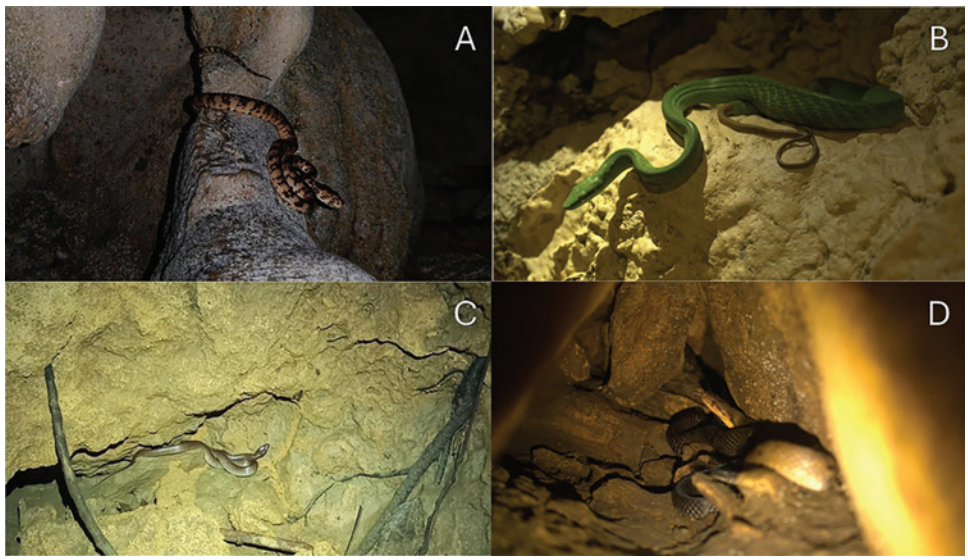


Figure 7. Snake species (Serpentes) recorded from limestone caves of the Andaman Islands: (a) Anderson's Pit Viper (*Trimeresurus andersonii*), (b) Red-tailed Racer (*Gonyosoma oxycephalum*), (c) Andaman Wolf Snake (*Lycodon hypsirhinoides*), and (d) Yellow-striped Trinket Snake (*Coelognathus flavolineatus*).

The caves are recognized as a significant habitat for the herpetofauna. The findings emphasize the subterranean habitats as a refuge for the herpetofauna of these unique tropical islands of India. We recommend conducting herpetofauna-focused cave studies, with special attention to the endemic species for targeted behavior and population abundance studies. We strongly appeal for conservation measures.

ACKNOWLEDGMENTS

We are grateful to the Ministry of Environment, Forests and Climate Change (MoEFCC) (2018–2020) and The Habitats Trust (THT) (2024–2025) for funding support. We are thankful to the Department of Environment and Forests, Andaman and Nicobar Islands, for granting the necessary permission and support. We sincerely thank Dr. S.R. Chandramouli and Dr. S. Harikrishnan for their help in the identification of the herpetofauna. We extend our gratitude to Dr. Prathamesh Gurjarpadhye and Mr. Sudheer Kumar Jena for their consistent support during the field work. We are thankful to Avimanyu Mukherjee and M. Vasudevan for their contributions during the surveys. Special thanks to Justin Sumit Kumar, Santial Toppo, Saw Safarmi, and Rajender Lakra, the swiftlet protection teams at Baratang, Interview Island, and Chalis-Ek, without whose support this work would have been unimaginable.

REFERENCES

Acuna-Mesen, R. A., 1994, Morphometric variation and ecologic characteristics of the habitat of the *Kinosternon scorpioides* turtle in Costa Rica (Chelonia, Kinosternidae): Revista Brasileira de Biologia, v. 54, no. 3, p. 537–547.

Andrews, H. V and Sankaran V., 2002, *Sustainable Management of Protected Areas in the Andaman and Nicobar Islands*: New Delhi, ANET, IIPA, and FFI.

Baumgart, G., 1981, Observations sur l'hibernation de quelques amphibiens dans les anciennes mines vosgiennes: Salamandre tachetée: Grenouille Rousse et Crapaud Commun: Aquarama, v. 58, p. 42–72.

Biswas, J., 2014, Occurrence and distribution of the cave-dwelling frogs of peninsular India: Ambient Science, v. 1, no. 2, p. 17–25, https://doi.org/10.21276/ambi.2014.01.2.rv02

Biswas, J., Shrotriya, S., Rajput, Y., and Sasmal, S., 2011, Impacts of ecotourism on bat habitats in caves of Kanger Valley National Park, India: Research Journal of Environmental Sciences, v. 5, no. 9, p. 752–762, https://doi.org/10.3923/rjes.2011.752.762

Bonini, L., Razzetti, E., and Barbieri, F., 1999, Cave breeding of *Bufo* (Linnaeus, 1758) in Liguria (North West Italy), *in* Miaud, C. and Guyetant, R., eds., Current Studies in Herpetology: Proceedings of the 9th Ordinary General Meeting of the Societas Europaea Herpetologica, p. 59–61.

Bressi, N and Dolce, S., 1999, Osservazioni di anfibi e rettili in grotta: Rivista di Idrobiologia, v. 38, p. 475–481, https://doi.org/10.21426/B632136017

Chakravarthy, N. V. K., Tripathi, K. P., and Gangwar, B., 1987, A comparative study of coastal climate with special reference to Andamans, India: Temperature and rainfall: Journal of the Andaman Science Association, v. 3, p. 119–124.

Champion, H. G and Seth, S. K., 2005, *A Revised Survey of the Forest Types of India*: Dehradun, Natraj Publishers.

Chandramouli, S. R., Vasudevan, K., Harikrishnan, S., Dutta, S. K., Jegath Janani, S., Sharma, R., Das, I., and Aggarwal, R., 2016, A new genus and species of arboreal toad with phytotelmonous larvae, from the Andaman Islands, India (Lissamphibia, Anura, Bufonidae): ZooKeys, v. 555, p. 57–90, https://doi.org/10.3897/zookeys.555.6522

Culver, D. C and Pipan, T., 2019, *The Biology of Caves and Other Subterranean Habitats*: Oxford, Oxford University Press, https://doi.org/10.1093/oso/9780198820765.001.0001

dos Santos, T., de Souza, A. M., Bondezan, F. L., and Eterovick, P. C., 2022, Going underground: What the natural history traits of cave users can tell us about cave use propensity: Journal of Herpetology, v. 56, no. 2, p. 153–163, https://doi.org/10.1670/20-055

Dutta, S. K., Nair, M. V., Mohapatra, P. P., and Mahapatra, A. K., 2009, *Amphibians and Reptiles*: Bhubaneswar, Regional Plant Research Centre Orissa, India, https://doi.org/10.13140/2.1.2440.0647

Esmaeili-Rineh, S., Shafiei, S., Malek-Hosseini, M. J., and Hosseinie, S., 2016, Distribution of cave-dwelling lizards of the families Gekkonidae and Phyllodactylidae (Sauria) in the Zagros Mountains, Iran: Subterranean Biology, v. 18, p. 39–47, https://doi.org/10.3897/subtbiol.18

Fenolio, D. B., Graening, G. O., and Stout, J. F., 2005, Seasonal movement patterns of Pickerel frogs (*Rana palustris*) in an Ozark cave and trophic implications supported by stable isotope evidence: The Southwestern Naturalist, v. 50, no. 3, p. 385–389, https://doi.org/10.1894/0038-4909(2005)050[0385:SMPOPF]2.0.CO;2

Garg, S., Chandrakasan, S., Gokulakrishnan, G., Gopika, C., Das, I., and Biju, S. D., 2022a, The curious case of Charles Darwin's frog, *Rana charlesdarwini* Das, 1998: Phylogenetic position and generic placement, with taxonomic insights on other Minervaryan frogs (Dicroglossidae: *Minervarya*) in the Andaman and Nicobar Archipelago: Vertebrate Zoology, v. 72, p. 169–199. https://doi.org/10.3897/vz.72.e79496

Garg, S., Sivaperuman, C., Gokulakrishnan, G., Chandramouli, S. R., and Biju, S. D., 2022b, Hiding in plain sight: Rain water puddles in Nicobar Islands of India reveal abundance of a new frog species of the genus *Microhyla* Tschudi, 1838 (Anura: Microhylidae): Zoological Studies, v. 61, p. e2, https://doi.org/10.6620/ZS.2022.61-2

Gosavi, N., Bayani, A., and Kunte, K., 2020, *Amphibians of India, v. 1.05*: Indian Foundation for Butterflies Trust, https://www.indianamphibians.org

Gunn, J., 2004, *Encyclopedia of Caves and Karst Science*: London, Routledge, https://doi.org/10.4324/9780203483855

Harikrishnan, S., Vasudevan, K., Chandramouli, S. R., Choudhury, B. C., Dutta, S. K., and Das, I., 2012, A new species of *Coryphophylax* Fitzinger in Steindachner, 1867 (Sauria: Iguania: Agamidae) from the Andaman Islands, India: Zootaxa, v. 3451, no. 1, p. 31–45, https://doi.org/10.11646/zootaxa.3451.1

Harikrishnan, S and Vasudevan, K., 2018, Amphibians of the Andaman & Nicobar Islands: Distribution, natural history, and notes on taxonomy: Alytes, v. 36, p. 238–265.

Harikrishnan, S., Ahmed, M. F., Das, A., Dutta, S. K., Giri, V., Mohapatra, P. P., Mukherjee, S., Thaker, M., Vijayakumar, S. P., and Shanker, K., 2022, A long-term monitoring programme to understand the impact of climate change on terrestrial herpetofauna of India: Hamadryad, v. 39, no. 1.

Ianc, R., Cicort-Lucaci, A. Ş., Ilieş, D., and Kovács, É. H., 2012, Note on the presence of *Salamandra* (Amphibia) in caves from Padurea Craiului Mountains, Romania: North-Western Journal of Zoology, v. 8, p. 202–204, https://doi.org/10.13140/2.1.3666

IUCN, 2023, The IUCN Red List of Threatened Species, *version 2023*, https://www.iucnredlist.org

Kami, H., 2004, The biology of the Persian Mountain Salamander, Batrachuperus persicus (Amphibia, Caudata, Hynobiidae) in Golestan Province, Iran: Asiatic Herpetological Research, v. 10, p. 182–190.

Kawalkar, D and Manchi, S., 2020, Coastal caves on the Interview Island of Andaman Islands, India: Carbonates and Evaporites, v. 35, no. 4, p. 111, https://doi.org/10.1007/s13146-020-00646-w

Kawalkar, D., Manchi, S., Parab, R., and Lad, P., 2024, First report of a freshwater turtle species as a permanent resident of a cave: The Herpetological Bulletin, v. 67, no. 167, p. 34–36, https://doi.org/10.33256/hb167.3436

Landová, E., Musilová, V., Polák, J., Sedláčková, K., and Frynta, D., 2016, Antipredatory reaction of the leopard gecko *Eublepharis macularius* to snake predators: Current Zoology, v. 62, no. 5, p. 439–450, https://doi.org/10.1093/cz/zow050

Lanza, B., Pastorelli, C., Laghi, P., and Cimmaruta, R., 2006, A review of systematics, taxonomy, genetics, biogeography and natural history of the genus *Speleomantes* Dubois, 1984 (Amphibia: Caudata: Plethodontidae): Atti del Museo Civico di Storia Naturale di Trieste, v. 52, p. 5–135.

Lunghi, E., Bruni, G., Ficetola, F. G., and Manenti, R., 2018, Is the Italian stream frog (*Rana italica* Dubois, 1987) an opportunistic exploiter of cave twilight zones?: Subterranean Biology, v. 25, p. 49–60.

Lunghi, E., Manenti, R., and Ficetola, G. F., 2017, Cave features, seasonality, and subterranean distribution of non-obligate cave dwellers: PeerJ, v. **5**, p. e3169, https://doi.org/10.7717/peerj.3169

Maglangit, E. P. T., Paraguya, J. J. J. B., Maglangit, R. M. T., Nuñeza, O. M., Diesmos, M. L. L., and Diesmos, A. C., 2021, Novel cave habitat used by the cryptic lizard *Pinoyscincus abdictus* (Squamata: Scincidae) on Dinagat Islands, Philippines: Phyllomedusa: Journal of Herpetology, v. 20, no. 1, p. 99–104, https://doi.org/10.11606/issn.2316-9079.v20i1p99-104

Mahony, S and Ali Reza, A. H. M., 2007, A herpetological collection from the Chittagong Hill Tracts, Bangladesh, with two new species records for the country: Hamadryad, v. 32, no. 1, p. 45–56.

Manchi, S and Sankaran, R., 2009, Predators of swiftlets and their nests in the Andaman and Nicobar Islands: Indian Birds, v. 5, no. 4, p. 118–120.

Manchi, S and Sankaran, R., 2014, Protection of the white-nest swiftlet (*Aerodramus fuciphagus*) in the Andaman Islands, India: An assessment: Oryx, v. 48, no. 2, p. 213–217, https://doi.org/10.1017/S0030605311000603

Mane, A. M., Prabakaran, N., and Manchi, S. S., 2019, Floral diversity, composition, and recruitment on the karstland of Baratang Island, India: Ecological Complexity, v. 37, p. 47–54, https://doi.org/10.1016/j.ecocom.2018.11.002

Manenti, R., Ficetola, G. F., Bianchi, B., and De Bernardi, F., 2009, Habitat features and distribution of *Salamandra* in underground springs: Acta Herpetologica, v. 4, no. 2, p. 143–151, https://doi.org/10.3390/d12040161

Milstead, W. W., 1956, Fossil turtles of Friesenhahn Cave, Texas, with the description of a new species of *Testudo*: Copeia, v. 1956, no. 3, p. 162–171.

Mohan, A. V., Orozco-terWengel, P., Shanker, K., and Vences, M., 2020, The Andaman day gecko paradox: An ancient endemic without pronounced phylogeographic structure: Scientific Reports, v. 10, no. 1, p. 11745, https://doi.org/10.1038/s41598-020-68402-7

Myers, N., Mittermeier, R. A., Mittermeier, C. G., da Fonseca, G. A. B., and Kent, J., 2000, Biodiversity hotspots for conservation priorities: Nature, v. 403, no. 6772, p. 853–858, https://doi.org/10.1038/35002501

Oldham, R. D., 1885, Notes on the geology of Andaman Islands: Records of the Geological Survey of India, v. 18, p. 135–145.

Olson, D. H and Saenz, D., 2013, Amphibians and Climate Change: U.S. Forest Service Climate Change Resource Center, https://www.fs.usda.gov/ccrc/topics/amphibians-and-climate-change https://doi.org/10.32800/abc.2005.28.0059

Pal, T and Bhattacharya, A., 2010, Greenschist-facies sub-ophiolitic metamorphic rocks of Andaman Islands, Burma-Java subduction complex: Journal of Asian Earth Sciences, v. 39, no. 6, p. 804–814, https://doi.org/10.1016/j.jseaes.2010.05.017

Pauwels, O. S. G., Carlino, P., Chirio, L., Daversa, D. R., Lips, J., Oslisly, R., and Testa, O., 2019, Amphibians and reptiles found in caves in Gabon, western Equatorial Africa: Cave and Karst Science, v. 46, no. 1, p. 3–12.

Poulton, B. C., 2004, Missouri River Benthic Macroinvertebrates: U.S. Geological Survey, Columbia Environmental Research Center, https://doi.org/10.1002/rra.1558

Quah, E. S. H., Grismer, L. L., and Shahrul, A. M. S., 2021, Conservation of Peninsular Malaysia's karst herpetofauna: A review of herpetological discoveries, research trends, and challenges: Raffles Bulletin of Zoology, v. 69, p. 573–601, https://doi.org/10.26107/RBZ-2021-0019

Rahmani, A. R., Islam, M. Z. U., and Kasambe, R. M., 2016, *Important Bird and Biodiversity Areas in India: Priority Sites for Conservation* (2nd edition), Vol I: Mumbai, Bombay Natural History Society, p. 1006.

Rajendran, K., Rajendran, C. P., Earnest, A., Prasad, G. R., Dutta, K., Ray, D. K., and Anu, R., 2008, Age estimates of coastal terraces in the Andaman and Nicobar Islands and their tectonic implications: Tectonophysics, v. 455, no. 1–4, p. 53–60, https://doi.org/10.1016/j.tecto.2008.05.004

Recknagel, H and Trontelj, P., 2022, From cave dragons to genomics: Advancements in the study of subterranean tetrapods: BioScience, v. 72, no. 3, p. 254–266, https://doi.org/10.1093/biosci/biab117

Romero, A., 2009, *Cave Biology: Life in Darkness*: Cambridge, Cambridge University Press, https://doi.org/10.1017/CBO9780511596841

Rosa, G and Penado, A., 2013, *Rana iberica* (Boulenger, 1879) goes underground: Subterranean habitat usage and new insights on natural history: Subterranean Biology, v. 11, p. 15–29, https://doi.org/10.3897/subtbiol.11.5170

Saldanha, C. J., 1989, *Andaman, Nicobar and Lakshadweep: An Environmental Impact Assessment*: New Delhi, Oxford & IBH Publishing Company, p. 215.

Sankaran, R., 1998, *The Impact of Nest Collection on the Edible-nest Swiftlet (Collocalia fuciphaga) in the Andaman and Nicobar Islands*: Coimbatore, Sálim Ali Centre for Ornithology and Natural History, p. 80.

Sankaran, R., 2001, The status and conservation of the Edible-nest Swiftlet (*Collocalia fuciphaga*) in the Andaman and Nicobar Islands: Biological Conservation, v. 97, no. 3, p. 283–294, https://doi.org/10.1016/S0006-3207(00)00124-5

Sequeira, F., Gonçalves, H., Faria, M. M., Meneses, V., and Arntzen, J. W., 2001, Habitat-structural and meteorological parameters influencing the activity and local distribution of the golden-striped salamander: Chioglossa Lusitanica: Herpetological Journal, v. 11, p. 85–90.

Sheridan, C. D and Olson, D. H., 2003, Amphibian assemblages in zero-order basins in the Oregon Coast Range: Canadian Journal of Forest Research, v. 33, no. 8, p. 1452–1477, https://doi.org/10.1139/x03-038

Shirley, M. H., Burtner, B., Oslisly, R., Sebag, D., and Testa, O., 2017, Diet and body condition of cave-dwelling dwarf crocodiles (*Osteolaemus tetraspis*, Cope 1861) in Gabon: African Journal of Ecology, v. 55, no. 4, p. 411–422, https://doi.org/10.1111/aje.12365

Sinha, Y. P., 1999, Bats of the Si Sheridanju Cave, South Garo Hills District, Meghalaya, India: Taxonomy and bionomics: Records of the Zoological Survey of India, v. 97, no. 1, p. 101–122, https://doi.org/10.26515/rzsi/v97/i1/1999/160258

Smart, U., Sarker, G. C., Arifin, U., Harvey, M. B., Sidik, I., Hamidy, A., Kurniawan, N., and Smith, E. N., 2017, A new genus and two new species of arboreal toads from the highlands of Sumatra with a phylogeny of Sundaland toad genera: Herpetologica, v. 73, no. 1, p. 63–75, https://doi.org/10.1655/Herpetologica-D-16-00041

Somaweera, R., Nifong, J., Rosenblatt, A., Brien, M. L., Combrink, X., Elsey, R. M., Grigg, G., Magnusson, W. E., Mazzotti, F. J., Pearcy, A., Platt, S. G., Shirley, M. H., Tellez, M., van der Ploeg, J., Webb, G., Whitaker, R., and Webber, B. L., 2020, The ecological importance of crocodylians: Towards evidence-based justification for their conservation: Biological Reviews, v. 95, no. 4, p. 936–959, https://doi.org/10.1111/brv.12594

Teo, E. W., Wong, S. P., Kem, Z., and Chan, K. O., 2023, Checklist of the herpetofauna of Batu Caves, Selangor, Malaysia: Malayan Nature Journal, v. 75, no. 1, p. 161–174.

Tuberville, T. D., Buhlmann, K. A., Bjorkland, R. K., Kerr, R. K., and Booher, D., 2005, Ecology of the Jamaican slider turtle (*Trachemys terrapen*), with implications for conservation and management: Chelonian Conservation and Biology, v. 4, no. 4, p. 908–915.

Turbanov, I. S., Kukushkin, O. V., and Vargovitsh, R. S., 2019, Amphibians and reptiles in the subterranean cavities of the Crimean Mountains: Russian Journal of Herpetology, v. 26, no. 1, p. 29–33, https://doi.org/10.30906/1026-2296-2019-26-1-29-53

Uhrin, M and Lesinsky, G., 1997, Mechanism of occurrence of amphibians in underground spaces in Slovakia: Preliminary data evaluation, *in* Proceedings of the 12th International Congress of Speleology, La Chaux-de-Fonds, Switzerland, Volume 3, p. 325–327.

Vijayamma, J. K., Dhamorikar, A., and Manchi, S., 2021, A new species of *Caridina* H. Milne Edwards, 1837 (Family: Atyidae) from a limestone cave on Interview Island, Andaman and Nicobar Islands, India: Zootaxa, v. 5057, no. 3, p. 102–114, https://doi.org/10.11646/zootaxa.5057.3.5

Wynne, J. J., Tellez, M., Hartwell, K., Reneau, S., Welch, G., Voyles, K. D., Cal, M., Cal, R., Castillo, D., and Champion, J., 2023, Cave-dwelling crocodiles of Central Belize: International Journal of Speleology, v. 52, no. 1, p. 75–81, https://doi.org/10.5038/1827-806X.52.1.2470

First Folia occurrence from Greece. Georgios Lazaridis and Panagiotis Sotirios Dittopoulos. *Journal of Cave and Karst Studies*, v. 88, no. 3, p. 72-77.
DOI: 10.4311/2025ES0118

FIRST FOLIA OCCURRENCE FROM GREECE

Georgios Lazaridis and Panagiotis Sotirios Dittopoulos

Abstract

Folia are among the rarest speleothems, known from 28 caves worldwide, and their origin is still a matter of ongoing scientific discussion and investigation. This study presents the first documented occurrence of folia in a Greek cave (Stafni Cave, Northern Greece), thus expanding the known geographical distribution and morphogenetic spectrum of these formations. The cave exhibits a morphologically complex setting with clear markers of water table oscillations, such as notches and cupolas, and unique depositional sequences that include folia, cave rafts, and associated pool infills. Notably, the folia occur stratigraphically beneath the rafts, suggesting progressive lowering of the water table. The folia deposit display classical "leaf-like" laminae. The preservation of these deposits below a thick layer of cave rafts that form a pseudo-floor suggests that their apparent rarity may reflect limited accessibility rather than true scarcity. Morphological features of the cave are consistent with speleogenetic models involving sulfuric acid speleogenesis (SAS), including sulfate mineral occurrences and proximity to active hydrogen sulfide-rich Na–Cl thermal springs. Folia morphology and formation are discussed. This study provides 3D documentation of a folia sample and lays the groundwork for future mineralogical and geochemical analyses aimed at testing these formation models. The findings contribute to ongoing debates on folia genesis and highlight the role of hypogene processes in cave evolution.

INTRODUCTION

Carbonate folia, the type investigated in this study, are rare speleothems formed primarily by carbonates, while similar folia morphologies occur in halite, elemental sulfur, mud, and lava, with 28 occurrences worldwide (Davis *et al.*, 2025). Carbonate folia are typically associated with oscillations of the water table and carbon dioxide degassing. They sometimes occur with dissolution features such as bubble trails, indicating dynamic physicochemical conditions during formation. Their formation process has been extensively studied and discussed (e.g., Green, 1991, 1997; Hill and Forti, 1997). A few controversial interpretations have been suggested, such as small-scale corrosion and calcite precipitation due to carbon dioxide degassing in hypogene speleogenesis (Green, 1991; Audra *et al.*, 2009); brine mixing (Queen, 2009); and deposition as a fluctuating-interface process based on particle accretion (Davis, 2012).

Although folia have been considered a strong indicator of hypogene speleogenesis, there are examples of epigene caves with folia occurrences (e.g., Plan and de Waele, 2011; D'Angeli *et al.*, 2015). López-Martínez *et al.* (2020) in their recent study of bubble trails and folia in the cenote Zapote in Mexico provide a detailed review of past works on folia. They also recognize "hell bells" as a subtype of folia. Similarly, another subtype of folia the "reversed pseudo-gours" found in Nerja Cave, Spain (Liñán Baena *et al.*, 2024). Queen (2009) identifies two morphological types of folia. In a recent review of folia occurrences, Davis *et al.* (2025) have summarized six folia types with respect to the controlling interface.

In Greece, more than 100 caves have been studied in relation to hydrothermal processes and hypogene speleogenesis (e.g., Lazaridis, 2017, 2024) without any previous identification of folia. This study provides a detailed account of the Stafni Cave morphology and its sedimentary infill where folia are identified and additionally supplemented by a 3D model accessible for further research.

The discovery of this previously undocumented occurrence of folia naturally invites an attempt to correlate the deposit with the speleogenetic history of the cave, thereby bringing into focus the range of formation mechanisms that have been proposed in the literature. To this end, the study was structured into two main stages: (1) interpretation of the cave's genesis; (2) identification and morphological characterization of the folia, with the aim of highlighting features critical to understanding the genesis of the deposit.

GEOLOGICAL SETTING

The Stafni Cave is located at about 23 m above sea level, in proximity to the hot springs of Eleftheres (Loutra Eleftheron), which are the only surface manifestation of the low-enthalpy Akropotamos geothermal field that exists in the area (Arvanitis *et al.*, 2016). Thermal water is recharged there along faults with a temperature of about 41.5 °C. The water is saline and rich in H_2S. The area is located in the Rhodope Massif and consists of marbles and gneisses intruded by tertiary granitoids (Eleftheriadis *et al.*, 2001). Parts of the basement are covered by post-Alpine sediments.

School of Geology, Aristotle University of Thessaloniki, 54124 Thessaloniki, Greece

In the broader region of the Loutra Eleftheron spring, small hypogene cave remnants lined with hydrothermal calcite have been identified in the marble (Lazaridis, 2024) and tafoni (small cavernous features formed by salt and moisture weathering) in the granodiorite (Lazaridis and Pipera, 2008).

METHODS

Samples of deposits collected from the cave include cave rafts, platy crystals, metallic mineral aggregates, and folia. The folia sample was taken from a loose, fallen fragment in order to preserve the *in situ* occurrence. Despite the exact location and orientation being unknown, the point at which the folia sample was separated from the lowest part of the documented *in situ* folia can be seen. 3D models of the cave and the folia site were created using the Polycam application on an iPhone 14 pro, which can provide cave maps that easily meet Grade 5 and, in many cases, meet Grade 6 prerequisites of the International Union of Speleology (UIS) as given in Häuselmann (2011), with the maximum possible detail (Lazaridis *et al.*, 2024). The option for photogrammetry in Polycam was used to create a digital model of the sample folia surface (Fig. 1).

RESULTS

Stafni Cave

The cave (Fig. 2) opens on a steep escarpment that dips to the south (76°/171°; dip angle/dip direction-marble dips with about 20° to the south) and develops into a low, sinuous passage that remains constricted throughout, requiring crawling for access (Fig. 3a). After approximately 6 m, an opening in the sediment fill of the floor becomes visible (Fig. 3b), flanked on both sides by well-defined notches just above the sediment surface. These notches are used as a reference level in the following description. A second level of a possible notch has been identified 1 m lower at a small inaccessible chamber that is partially scanned and included in the 3D model. Higher on the ceiling, cupolas have formed. At least two

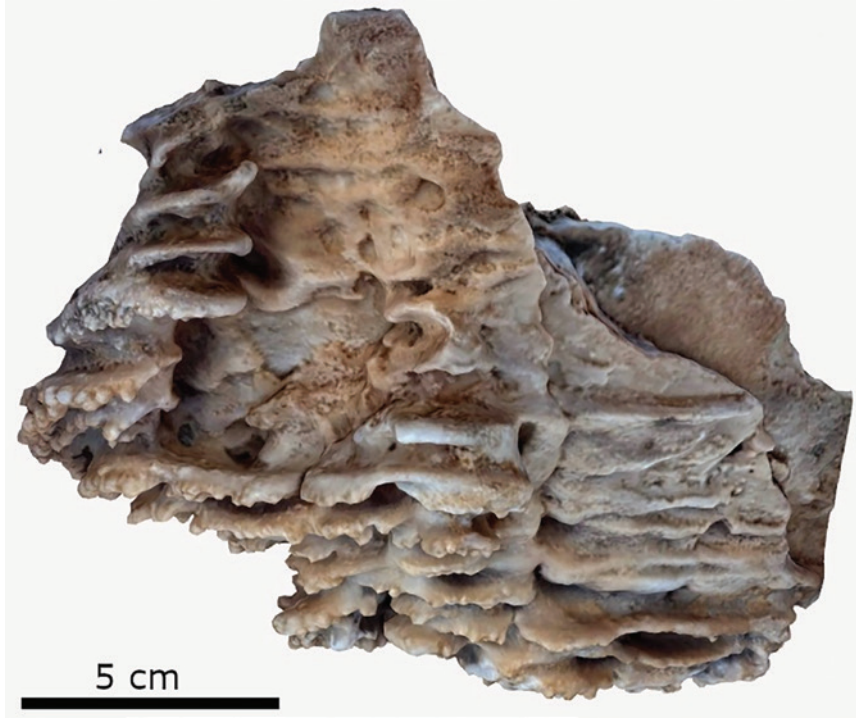


Figure 1. 3D model of the folia sample from the Stafni Cave (https://poly.cam/capture/BE3ECB8F-1C07-4291-BDCF-870A460B73E3).

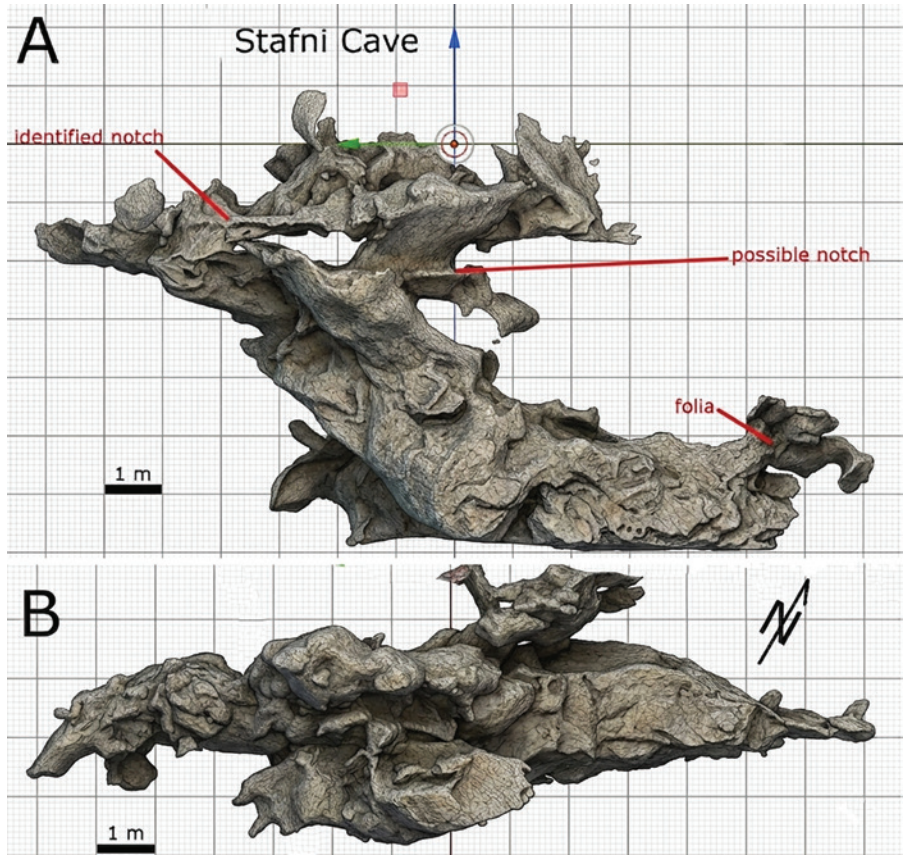


Figure 2. Stafni Cave 3D model: (a) Profile view of the model seen from the north. The position of an identified pair of notches is depicted, as well as a level of a possible notch in a small chamber. Folia occurrence in the innermost part of the cave. (b) Top view of the model. The escarpment dips to the south (171°). Arrows represent the three-axis reference system of the model.

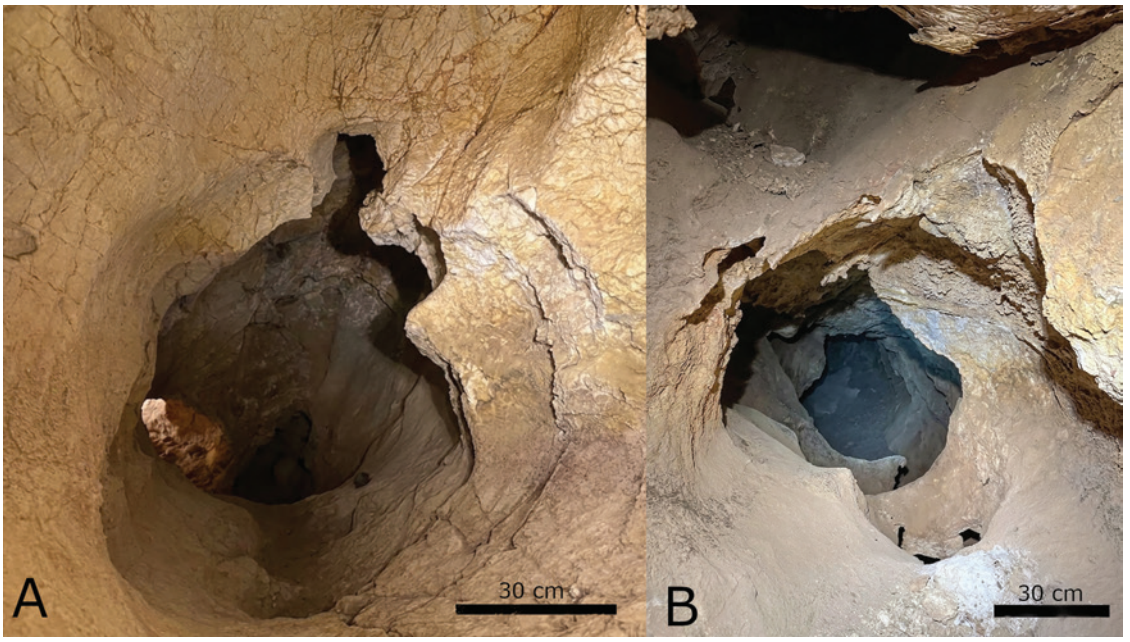


Figure 3. (a) Passage shape close to the entrance. (b) Descending passage to the lowest level.

shallow, pond-like features are also observed on the bedrock floor of the passage.

The opening leads downward (Fig. 3b) into a lower, linear chamber. At this point, the exposed cross section of the sediment fill reveals a thick accumulation of cave rafts, some exceeding 10 cm in diameter and a few millimeters in thickness. Similar raft-like features are also preserved on the ceiling of the chamber, where their flat surfaces are visible. In many places, these rafts are deposited at various angles, not necessarily horizontal, suggesting disturbance or variable water dynamics. The descending part is composed of successive holes and ridges. Just above the chamber floor, at least one occurrence of metallic-rich mineralization (possibly iron oxides or hydroxides) is observed on the wall. A nearby bedrock protrusion is coated with euhedral platy crystals, a few millimeters in length, forming aggregates that resemble desert rose aggregates, a morphology typical of sulfate minerals such as gypsum and baryte.



Figure 4. Folia deposits on the walls of the deepest part of the Stafni Cave at depths −3.65 to −3.85 below the notch level.

Cave coralloids locally cover the chamber walls. The floor at approximately −6.4 m below the notch reference level has a gray coloration, possibly indicative of past lake conditions within the cave.

In the innermost part of the chamber, folia speleothems are preserved *in situ*, still attached to the walls (Fig. 4). Additionally, at least one small bedrock fragment coated with folia was found on the chamber floor, indicating localized breakdown. The *in situ* folia are well developed at a depth between −3.65 and −4.70 m below the notch level.

The carbon dioxide concentration was 447 ppm in the surroundings of the cave, 615–665 ppm outside the entrance, 990–1022 ppm 1 m from the entrance, and 995–1158 ppm at the bottom of the cave.

Observations of the Folia Morphology

Since folia formation has been explained in previous studies, it is worth highlighting a few observations and suggestions based on the occurrence in the Stafni Cave.

The folia form a layered, step-like structure of repetitive, sub-horizontal ridges or "leaves" growing outward and downward. There appears to be a relatively regular distance between folia layers. These "leaves" form convex-up cups (some almost overhanging). Often, there are holes even at the central part of the "leaves" and successive layers show holes in line (Fig. 5). A series of folia cups can shape an angled downward deposit and sometimes appear overhanging in the central part of the passage. These parts resemble "stemmed" folia or "hells bells" (Fig. 5). Folia ridges measured in a few places are horizontal. The formation of folia took place on a few-millimeters-thick, subparallel, inclined deposits (see point 3 in Fig. 5b). Small cave coralloids are formed on the rims of the folia after their formation, developing on the typical folia morphology as described by Davis *et al.* (2025).

DISCUSSION

The Stafni Cave presents a complex interplay of depositional and dissolutional features that reflect the cave's hydrological evolution. The uppermost notch marks a former stable water table, while the accumulation of cave rafts just below this level indicates persistent standing water conditions conducive to their formation. The absence of shelfstone, however, suggests that this water surface was not long-term stable, or lacked the specific conditions required for shelfstone development.

A deeper depositional horizon is defined by the presence of folia speleothems, which occur stratigraphically beneath the cave rafts. This vertical succession of folia below cave rafts suggests a progressive lowering or oscillation of the water table, with discrete depositional phases tied to changing hydrological and physicochemical conditions.

Are folia rare speleothems, or are they rarely observed due to accessibility and observational bias? This question arises from the peculiar setting in the Stafni Cave, where folia occur beneath thick accumulations of cave rafts and pool sediment infill that form a pseudo-floor. Had the opening to the deeper passage not been exposed, the presence of folia would likely have remained undetected. In hypogene caves of Greece, and likely elsewhere, such "windows" into lower sediment-buried levels are rare. Consequently, folia may not be inherently rare, but rather rarely accessible, their apparent scarcity shaped by observational bias.

While folia have not yet been documented in other Greek caves, other lake-related speleothems are more common. Shelfstone and, more rarely, cave rafts have been reported in various hypogene and epigene settings. However, the abundance and dimensions of the cave rafts in the Stafni Cave appear unique in the regional context. Notably, cave rafts may occur alongside both folia and shelfstone, but the latter two are seldom found in association. Although all three form near the water–air interface, their differing occurrences suggest distinct physicochemical regimes or water-body dynamics.

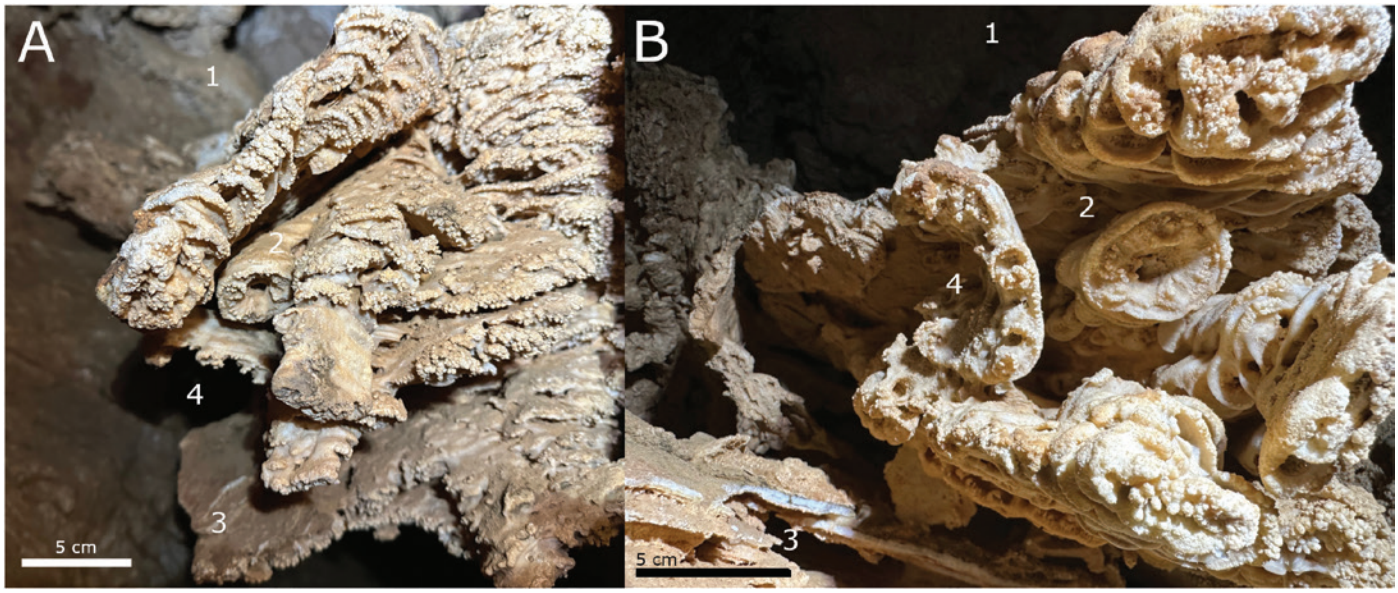


Figure 5. Folia in the Stafni cave: (a) Lateral upward view in the central part of the folia-bearing passage at about −4.7 m from the notch level. (b) Upward view of the same spot. (1) This free-hanging part of the folia was developed on thin planes of calcite that have been removed. (2) This part of the folia forms closed elliptical ridges and in total is almost free hanging. (3) The point that probably corresponds to the original position of the collected sample. (4) Another point of free-hanging folia that remains open at the posterior part. Points 2 and 4 resemble "hell bels."

This interpretation aligns with observations from the literature: folia typically do not form in perched pools (Queen, 2009); folia often develop in discrete zones, rather than uniformly along pool perimeters (e.g., Audra *et al.*, 2009). Such spatial selectivity implies that folia formation is not merely a function of water level, but also of specific microenvironmental or geochemical conditions.

Another key point concerns the relationship between folia and degassing. Although folia formation has been linked to CO_2 degassing and bubble trails (Green, 1991, 1997; Audra *et al.*, 2009), this connection is not always straightforward. Davis (2012) emphasized that bubble trails are not consistently present. In the Stafni Cave, no clear bubble trails were observed on bedrock surfaces, yet holes within folia laminae (Fig. 3b) may reflect former gas escape paths, suggesting that degassing was at least locally active.

From a genetic standpoint, folia occur in both hypogene and epigene caves. In the Stafni Cave, notches with cupola development above them indicate prolonged water table residence and intense condensation corrosion above that level; these features are consistent with the SAS (Sulfuric Acid Speleogenesis) model. The presence of sulfates at deeper levels can also be interpreted within this framework, adding the Stafni Cave to the inventory of SAS caves in Greece (see Lazaridis *et al.*, 2024).

Today, hydrogen sulfide-bearing, Na–Cl-type thermal springs emerge near the cave at Loutra Eleftheron. If a similar hydrochemical regime existed during the cave's formative phases, ponded waters may have had analogous compositions. In such conditions, carbonate precipitation could have been induced by a variety of mechanisms: evaporation; CO_2 degassing; mixing with meteoric freshwater; biologically mediated pH shifts; and hydrogen sulfide oxidation, although the relative role of these processes would depend on the local geochemical setting.

Under this scenario, folia formation would be genetically tied to hypogene processes due to the deep-seated, geothermally influenced waters in the case study. However, it should be noted that SAS-type caves have also been documented in epigene settings (D'Angeli *et al.*, 2018; Webb, 2021), cautioning against a singular genetic interpretation. Interestingly, the cenotes where "hell bells" are originally found (however, quite rarely) contain a mixing zone with hydrogen sulfide (Ritter *et al.*, 2019; López-Martínez *et al.*, 2020; Davis *et al.*, 2025).

The nearby hot springs, notches, complex cave morphology, and sulfate deposits, coupled with a distinct lack of epigene features, strongly support a hypogene origin for the cave. In this context, the folia are interpreted as water table-controlled features, likely representing a former air–water interface. This interpretation is further reinforced by the cave's low elevation, which suggests proximity to the regional or local thermal water table during its formation.

CONCLUSIONS

The investigation of the Stafni Cave has revealed a morphologically complex and hydrogeologically dynamic environment, marked by its morphology and the recognition of multiple speleogenetic events. Within this framework, the identification of a folia deposit constitutes a significant finding, representing the first documentation of this speleothem type in a Greek cave. The occurrence of folia in such a context not only expands the known geographical distribution of these enigmatic deposits but also raises important questions regarding their formation processes.

While the precise genesis of the folia at the Stafni Cave remains open to further mineralogical and geochemical analysis, the observed morphology, spatial arrangement, and possible hydrological setting suggest a formation process consistent with known folia development under conditions of gas-supersaturated waters. The isolation of the deposit from dripping water, its consistent elevation relative to past water levels, and the proximity to conduits that may have facilitated CO_2 or H_2S degassing collectively support a model involving physicochemical precipitation near to or at the water/air interface.

This study has laid the groundwork for further investigation and provided high-resolution 3D documentation, which is made available for further research. By situating the deposit within the broader context of the cave's evolutionary history and comparing it with formation mechanisms proposed in the literature, various parameters for its development have been discussed. Future mineralogical and geochemical research will be critical in refining our understanding of the environmental conditions that led to the formation of this deposit and, more broadly, in testing the applicability of proposed models of folia genesis to new cave settings.

ACKNOWLEDGMENTS

The climbers Markos Paptsikis and Panagiotis Dimopoulos are gratefully acknowledged for providing information about the cave.

REFERENCES

Audra, P., L. Mocochain, J. Y. Bigot, and J. C. Nobécourt, 2009, The association between bubble trails and folia: a morphological and sedimentary indicator of hypogenic speleogenesis by degassing, example from Adaouste Cave (Provence, France): International Journal of Speleology, v. 38, no. 2, p. 93–102, https://doi.org/10.5038/1827-806X.38.2.1

Arvanitis, A., E. Dotsika, and N. Kolios, 2017, Geochemical characteristics of the geothermal fluids in the Akropotamos area (Macedonia, Northern Greece): Bulletin of the Geological Society of Greece, v. 50, no. 2, p. 596–605, https://doi.org/10.12681/bgsg.11764

Davis, D. G., L. D. Hose, and H. R. DuChene, 2025, The taxonomy and origins of folia: a brief review: International Journal of Speleology, v. 54, no. 2, p. ijs2563,https://doi.org/10.5038/1827-806X.ijs2563

D'Angeli, I., C. Carbone, M. Nagostinis, M. Parise, M. Vattano, G. Madonia, and J. De Waele, 2018, New insights on secondary minerals from Italian sulfuric acid caves: International Journal of Speleology, v. 47, no. 3, p. 271–291, https://doi.org/10.5038/1827-806X.47.3.2175

D'Angeli, I. M., J. De Waele, O. C. Melendres, N. Tisato, F. Sauro, E. R. G. Gonzales, S. M. Bernasconi, S. Torriani, and T. R. Bontognali, 2015, Genesis of folia in a non-thermal epigenic cave (Matanzas, Cuba): Geomorphology, v. 228, p. 526–535, https://doi.org/10.1016/j.geomorph.2014.09.006

Davis, D. G., 2012, In defense of a fluctuating-interface, particle-accretion origin of folia: International Journal of Speleology, v. 41, no. 2, p. 189–198, https://doi.org/10.5038/1827-806X.41.2.6

Eleftheriadis, G., W. Frank, and K. Petrakakis, 2001, 40Ar/39Ar dating and cooling history of the Pangeon granitoids, Rhodope Massif (Eastern Macedonia, Greece): Bulletin of the Geological Society of Greece, v. 34, no. 3, p. 911–916.

Green, D. J., 1991, On the origin of the folia and rims: Salt Lake Grotto Technical Note, No. 88: Huntsville, Ala, National Speleological Society, p. 182–196.

Green, D. J., 1997, The origin of folia: Salt Lake Grotto Technical Note, No. 96: Huntsville, Ala, National Speleological Society, p. 51–60.

Häuselmann, P., 2011, UIS mapping grades: International Journal of Speleology, v. 40, no. 2, p. IV–VI.

Hill, C. A., and Forti, P., 1997, *Cave Minerals of the World*: Huntsville, Ala., National Speleological Society, p. 73–74.

Lazaridis, G., 2024, Formation conditions of hypogene caves in the Hellenic orogen: mineralogy, geochemistry, stable isotopes (C, O, S), fluid inclusions [Ph.D. thesis]: Thessaloniki, Aristotle University of Thessaloniki, Annex Number of Scientific Annals of the School of Geology No. 245, 165 p.

Lazaridis, G and K. Pipera, 2008, Preliminary report on granite caves in Greece: Cadernos do Laboratorio Xeolóxico de Laxe, v. 33, p. 101–113.

Lazaridis, G., 2017, Hypogene speleogenesis in Greece, *in* Klimchouk, A., Palmer, A. N., De Waele, J., Auler, A. S., and Audra, P., eds., *Hypogene Karst Regions and Caves of the World*: Cham, Springer, p. 225–239, https://doi.org/10.1007/978-3-319-53348-3_14

Lazaridis, G., K. P. Trimmis, I. Drnić, and K. Brkić Drnić, 2024, Deciphering rock surface origins in a karst cave: insights from the Rača Cave, Lastovo, Croatia: Geologia Croatica, v. 77, no. 3, p. 235–242.

Liñán Baena, C., C. Jiménez de Cisneros, Y. Del Rosal, and P. Forti, 2023, Reverse pseudo-gours: a new sub-type of folia observed in the Nerja Cave (SE Spain): International Journal of Speleology, v. 53, no. 1, p. 1–12, https://doi.org/10.5038/1827-806X.53.1.2485

López-Martínez, R., F. Gázquez, J. M. Calaforra, P. Audra, J. Y. Bigot, T. Pi Puig, R. J. Alcántara-Hernández, Á. Navarro, P. Crochet, L. Corona Martínez, and R. Daza Brunet, 2020, Bubble trail and folia in cenote Zapote, Mexico: petrographic evidence for abiotic precipitation driven by CO_2 degassing below the water table: International Journal of Speleology, v. 49, no. 3, p. 173–186, https://doi.org/10.5038/1827-806X.49.3.2344

Plan, L and J. De Waele, 2011, Folia in der Odelsteinhöhle, Steiermark. Erstnachweis im deutschsprachigen Raum (Folia in Odelstein Cave, Styria first description from the German-speaking realm): Die Höhle, v. 62, p. 54–57.

Queen, M., 2009, The Lost City: hot springs, mixing and a possible model for folia development, *in* White, W. B., ed., 15th International Congress of Speleology, Proceedings, Volume 3, p. 1650–1656.

Ritter, S. M., M. Isenbeck-Schröter, C. Scholz, F. Keppler, J. Gescher, L. Klose, N. Schorndorf, J. Avilés Olguín, A. González-González, and W. Stinnesbeck, 2019, Subaqueous speleothems (Hells Bells) formed by the interplay of pelagic redoxcline biogeochemistry and specific hydraulic conditions in the El Zapote sinkhole, Yucatán Peninsula, Mexico: Biogeosciences, v. 16, no. 11, p. 2285–2305, https://doi.org/10.5194/bg-16-2285-2019

Webb, J. A., 2021, Supergene sulphuric acid speleogenesis and the origin of hypogene caves: evidence from the Northern Pennines, UK: Earth Surface Processes and Landforms, v. 46, no. 2, p. 455–464, https://doi.org/10.1002/esp.5037

Matthew Kaspar, Kathryn Brown, Jonathan D. Price, Brian Vauter, and Kashif Mahmud. Mapping groundwater infiltration in Karst using LIDAR at Natural Bridge Caverns, Texas. *Journal of Cave and Karst Studies*, v. 88, no. 3, p. 78-99. DOI: 10.4311/2025ES0109

MAPPING GROUNDWATER INFILTRATION IN KARST USING LIDAR AT NATURAL BRIDGE CAVERNS, TEXAS

Matthew Kaspar[1,2], Kathryn Brown[1], Jonathan D. Price[1], Brian Vauter[3], and Kashif Mahmud[1]

Abstract

The Trinity and Edwards Aquifers, two of the nine major groundwater systems in Texas, are significant sources of water in south-central Texas. The aquifers are primarily hosted in a network of fractured carbonate rock with substantial areas of cavernous porosity. This study used Light Detection and Ranging (LiDAR) to generate a three-dimensional point cloud in centimeter resolution to study water flow patterns within cavernous porosity. The research was conducted at Natural Bridge Caverns (NBC), a cave system northeast of San Antonio, Texas. The NBC cave system formed within Cretaceous carbonate rocks that host the Trinity and Edwards Aquifers. Our investigation focused on various spatial resolutions of LiDAR point cloud data to map and assess the size and spatial distribution of cave ceiling features (stalactites). The best spatial resolution to accurately identify and count stalactites, when compared to manual counts of stalactites, was established. Areas of specific flow types were classified using stalactite morphology and spatial distribution. Additionally, the effect of LiDAR distance from the cave ceiling/wall surface on the identification process was evaluated. We found that the number of LiDAR scans has a greater effect on data quality than scan distance. For the analysis of larger ceiling sections in various cave chambers, we established an optimal resolution of 10 mm (~0.39 in.). We established an optimal threshold of 97th percentile for stalactite identification and a threshold of 93rd percentile for flow classification. The flow classification based on stalactite morphological analysis shows that the Castle of the White Giants exhibits the highest amount of flow despite the chamber having the thickest overburden. The chamber also presents the greatest flow rate within the caverns.

INTRODUCTION

Aquifers, the underground layers of water-permeable rock and sediments, are crucial water resources. Karst aquifers supply 20%–25% of the water resources around the world (Ford and Williams, 2007). The Edwards (Balcones Fault Zone) Aquifer and the Trinity Aquifer, two of the nine major groundwater systems in Texas, are a significant source of water in south-central Texas. The Edwards and Trinity Aquifers are primarily hosted in Cretaceous limestones and dolostones (Gary, 2011; Clark and Morris, 2017).

The primary recharge of the Edwards Aquifer in south-central Texas (Fig. 1) is along the Balcones Fault Zone (BFZ) (Kastning, 1983). BFZ normal faulting initiated during the Late Oligocene and continued into the Early Miocene, increasing the hydraulic conductivity of the area (Barker et al., 1994). In Bexar County and adjacent regions, the Edwards Aquifer flows south by southeast before curving to flow from west to east (Shindel, 2019). Fault displacement reaches 305 m. Fault-enhanced fractures have formed large zones of cavernous porosity (Gary, 2011). Faulting produces interfacing between the Edwards and Trinity aquifers (Lindgren et al., 2004; George et al., 2011; Bruun et al., 2016).

The strata of the Trinity and Edwards Groups host numerous caverns. The assessment of groundwater movement through speleothems plays a significant role in estimating infiltration through karst environments. Several studies have shown that the size, location, and shape of stalactites have a profound influence on infiltration in the subsurface (Klimchouk et al., 2000; Ford and Williams, 2007; Mahmud et al., 2015). Therefore, understanding the factors can provide valuable insights into groundwater dynamics in karst environments similar to the Natural Bridge Caverns. Terrestrial LiDAR is increasingly utilized in high-resolution 3D modeling of cavernous karst formations (Bellian et al., 2005; Pringle et al., 2006); a single LiDAR scan collects hundreds of millions of coordinates that detail speleothem distribution in caves. Most knowledge of groundwater flow behavior and potential contamination has come from drilling and well observation, leaving our understanding underdeveloped. Drilling uses carbonic acid to dissolve away rock, altering the rock, and may lead to inaccuracies in mapping karst formations. Similarly, wells are complicated and expensive to make and maintain. Use of LiDAR in caves allows the study of karst without additional host rock deformation or alteration of aquifer flow paths.

The Natural Bridge Caverns (NBC) is a cave system located within the BFZ, northeast of San Antonio, Texas, placing it directly in the recharge zone of the Edwards Aquifer. NBC has two major sections, a southern section named the Hidden Passages and a northern section named the Discovery Passages, which is the focus of this study. Both sections cut the Glen Rose Formation (Trinity Group) and the Kainer Formation (Edwards Group) (Fig. 2), somewhat uniquely

[1]Kimbell School of Geosciences, Midwestern State University, Wichita Falls, Texas 76308
[2]National Cave and Karst Research Institute, 400-1 Cascades Ave., Carlsbad, New Mexico 88220
[3]Natural Bridge Caverns, 26495 Natural Bridge Caverns Road, San Antonio, Texas 78266

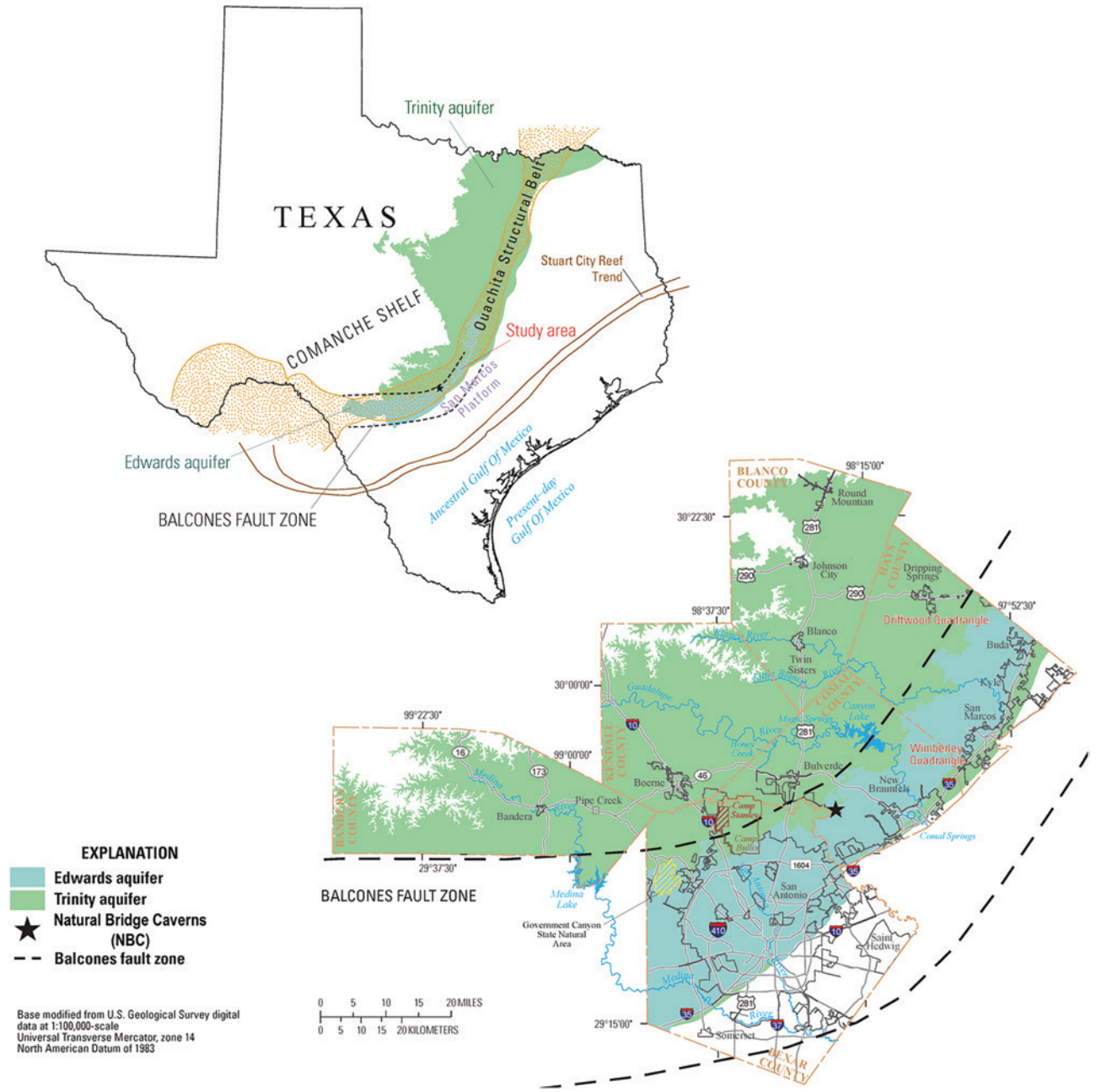


Figure 1. Location map showing the Edwards and Trinity Aquifers, the Balcones Fault Zone (BFZ), and Ouachita Structural Belt (top). Also, a close-up map of the Edwards Aquifer showing recharge zones of the BFZ and the location of NBC marked by the black star (bottom). Modified from Clark and Morris (2017).

connecting the two aquifers. The system is proximal to the saturated zone of the Trinity Aquifer; lower sections of NBC's Discovery Passages (the Castle of the White Giants and Purgatory Creek Sections) are prone to flooding events during intense precipitation (Gary, 2011).

The cavern system is hosted in the upper member of the Glen Rose Formation and the dolomitic and basal layers of the Kainer Formation, which are Lower Cretaceous sub-tidal to intertidal carbonates. The lower Glen Rose Formation is 91–98 m of rudist-reefal dolomitic limestone, highly karstified (Gary, 2011). The upper (Cavernous) member is roughly 152 m of interbedded dolomite and chalky limestone that weathers to stair-step morphology (Maclay and Small, 1986; Gary, 2011). Locally, the Glen Rose Formation is overlain by the nodular member of the Kainer Formation, 15–18 m of irregularly bedded micritic nodular limestone and clay. In the subsurface, it acts as a lower confining unit for the Edwards Aquifer but is karstified at the outcrop level (Gary, 2011). The cavern system roof partially extends into the dolomitic member, a dense crystalline carbonate with grainstone layers (Fig. 2).

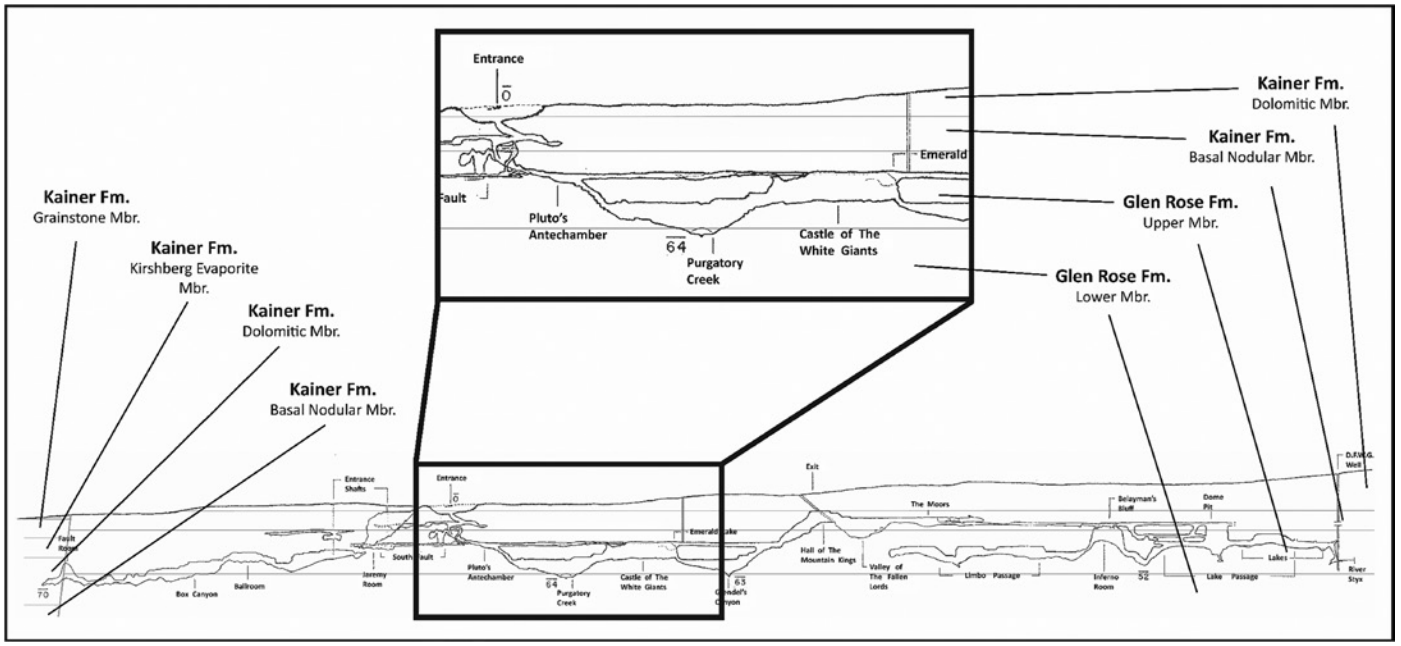


Figure 2. A cross section of NBC that shows the stratigraphic layers with which the cave system interacts within the Kainer Formation and the Glen Rose Formation modified from Kastning (1983) using information from Gary (2011).

Karst formation in the area occurred in two stages. First, exposure of the region subjected the strata to cavity formation by meteoric water shortly following deposition. The area was then buried, insulating it from further karstification. The next deformation of the area resulted in a 6° regional dip in present strata, causing extensional faulting and minor folding accompanied by fractures, which increased karst formation (Bellian et al., 2005; Clark and Morris, 2017).

Accessibility to aquifers is limited, which makes accurate data collection and modeling difficult. Most understanding of groundwater flow behavior and potential contamination has come from drilling and well observation, leaving our understanding underdeveloped. Drilling uses carbonic acid to dissolve away rock, altering the rock and leading to inaccuracies in mapping karst formations. Wells are also complicated and expensive to make and maintain. Studying caves gives access to key aquifer components and allows for the study of an aquifer without altering it.

This study applies the technique of Mahmud et al. (2015) to the recharge space of the Edwards and Trinity Aquifers. The objective of this study is to apply the technique in a more complex system at NBC. This method also needs parameter optimization based on a specific cave site and the associated stalactites' morphological attributes. NBC lies under an extremely heterogeneous karst environment. Hence, we optimize the algorithm parameters based on NBC stalactite morphology and spatial distribution, which are far more complicated than those in the previous study site at Mahmud et al. (2015). The initial results of Mahmud et al. (2015) were later validated using cave drip logger data in Mahmud et al. (2016), where cross-referencing outputs from both the stalactite morphological analysis and cave drip method showed correlating results. Here, we perform morphological and spatial analysis of cave ceiling features primarily using the cross-sectional area and aspect ratio of both singular and groups of stalactites to characterize the flow infiltration processes. The primary flow types defined are (1) intergranular percolation **matrix flow**, (2) conduit-focused **fracture flow**, and (3) matrix-and-fracture **combination flow**. This study identified the optimal resolution of LiDAR point clouds and input parameters that fit for analyzing the flow types at NBC. We evaluate scan attributes (such as distance, number, and angle) on the final stalactite count and flow classification using data from Brown et al. (2023).

METHODS

LiDAR Data Collection

This survey of NBC's Discovery Passages used a Leica BLK360 terrestrial LiDAR with a resolution of 5 mm at a distance of up to 45 m. The survey began at the Castle of the White Giants and scanned through the southern sections of the cave, including Purgatory Creek, Sherwood Forest, Pluto's Antechamber, and the south entrance of the cavern (Fig. 3). The survey collected 57 total individual scans. It attempted to scan most major speleothems from a minimum of four angles to maximize the quality of the LiDAR point cloud. Most of the accessible caverns (Purgatory Creek and switchbacks leading to Pluto's Antechamber) were limited to a single path, reducing the number of angles possible. Large areas, such as the Castle of the White Giants, allowed more scan angles. Once completed, the LiDAR data were

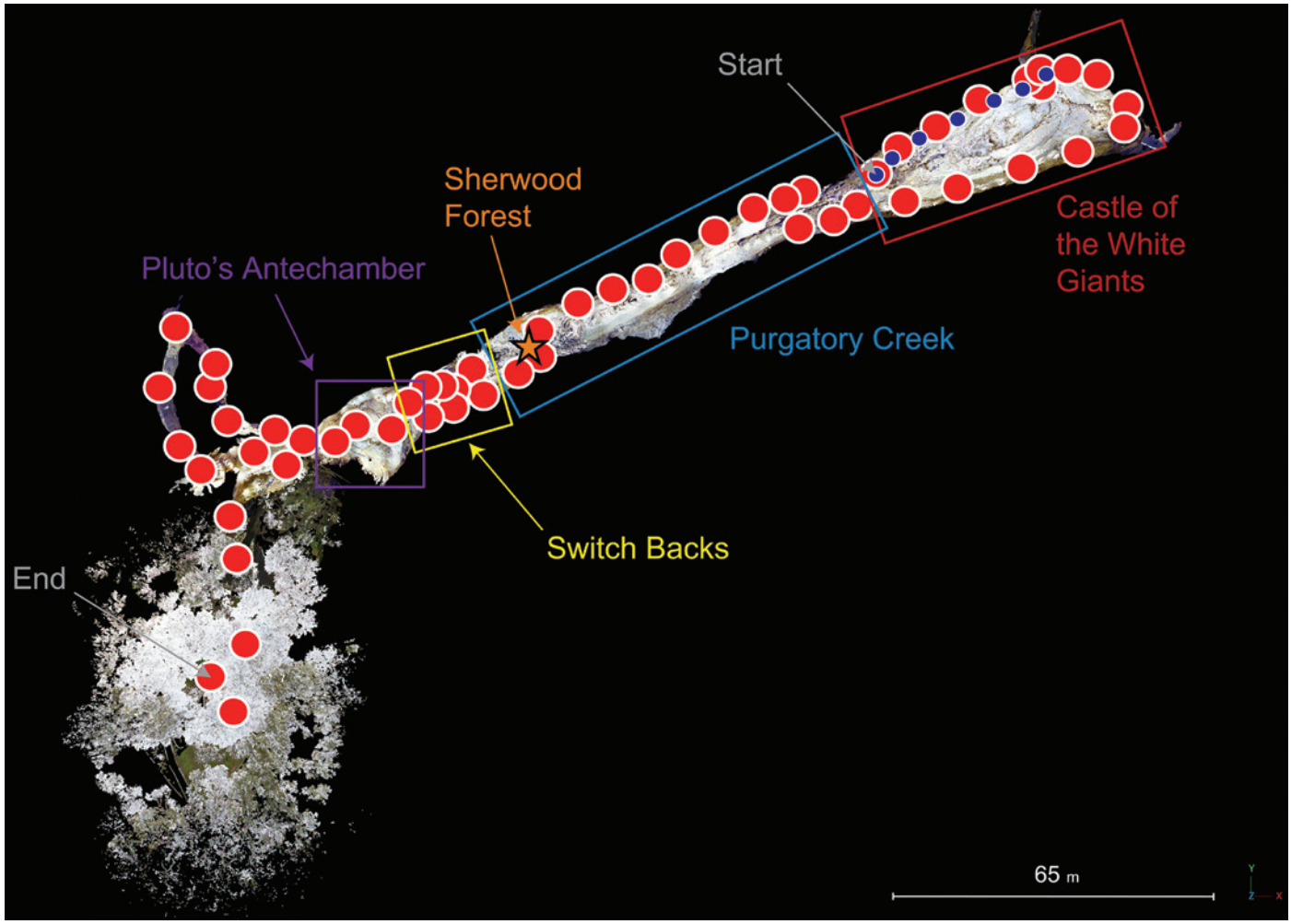


Figure 3. Final LiDAR point cloud of the Southern section of NBC's Discovery Passages showing all 57 scan locations represented by red dots from the start to end point covering the Castle of the White Giants, Purgatory Creek, Sherwood Forest, the Switch Back, and Pluto's Antechamber. Additional scans are considered from Brown et al. (2023) and are indicated by smaller blue dots.

downloaded using the Leica Cyclone REGISTER 360 software, where the individual scans were aligned and linked into a single point cloud to be exported. Combining multiple scans together fills in holes left by the individual scans and can further decrease point spacings by capturing stalactites at different angles and overlapping scans in existing areas.

The first LiDAR scan (set 1) of Discovery Passages was presented in Brown et al. (2023). This set started in the Castle of the White Giants and moved north to the exit passages. This was collected using the same LiDAR unit and scan strength as the later survey collected for this study.

Stalactite Identification Process

The study created an averaged surface to represent the overall cave ceiling topography using the moving average window of the ceiling surface. Window size was optimized through trial and error, varying the size in increments of 10 cm. The actual ceiling point cloud is subtracted from the smooth ceiling surface to generate a map of anomalies. These anomalies define the location of stalactites within the ceiling section. A histogram of the anomalies was plotted, and a threshold parameter was used to identify the individual stalactites. Anything below the threshold was natural rock surface variability and was not identified as stalactites. Lastly, a connected component analysis was performed (Mahmud et al., 2015) with the flow percentile threshold to group stalactites in close proximity for the identification of fracture and combination flow. The morphological properties of those groups determined the different water flow types. These properties consisted of stalactite's cross-sectional area and its aspect ratio. A more in-depth explanation is available in Mahmud et al. (2015).

Manual counts of stalactites are required for verification. This study counts these using photos of the cave ceiling and the point cloud viewed in CloudCompare. Total count assessment requires care to identify closely lying stalactites.

Visible spikes on cave ribbon are included in this count. Soda straws (subclass of matrix flow) are counted separately and subtracted from the total count to give the stalactite counts and soda straw counts as further comparison points.

Optimizing Resolution and Input Parameters

The technique introduced in Mahmud et al. (2015) is a semi-automated method that requires optimizing a set of input parameters for a specific cave site. These parameters are moving average window size, stalactite percentile threshold, and flow percentile threshold. The moving average window represents the cell numbers considered to generate the average ceiling surface. To optimize these parameters, the point spacing or resolution of the LiDAR point cloud must also be optimized to avoid extraneous data and to optimize the computational requirement. Four areas of easily identifiable features were clipped out of the ceiling point cloud using CloudCompare. Three of these were located in Purgatory Creek, and the remaining clip was from Sherwood Forest. These clips were cleaned of extraneous data points. The individual scans are then subsampled with six different point spacings or resolutions (2, 4, 6, 8, 10, and 12 mm). These clips are exported from CloudCompare and input into MATLAB to be converted into Stanford Geostatistical Modeling Software (SGEMS) files using the scattered interpolation prompt (scatteredInterpolant) with a natural neighbor interpolation method and no extrapolation method. The processed point clouds were analyzed to identify stalactite locations and generate flow type maps. Flow type maps were compared to a visual analysis of stalactite morphology to verify the accuracy with the input parameters. The tool also gives total stalactite counts of both soda straw stalactites and regular stalactites, which were compared to manual counts using field photographs and original LiDAR point clouds (Fig. 4). This was completed for every resolution with varying input parameters to find the optimum parameter set giving the closest stalactite counts.

Analyzing the Effect of Scan Number and Resolution on Stalactite Count

The northern section of NBC's Discovery Passages was surveyed as part of another study (set 1) (Brown et al., 2023). The previous survey area overlapped in the Castle of the White Giants. The major differences between the two surveys were the number of scans and the locations of the LiDAR. This survey consisted of 14 scans around the entire perimeter of the chamber, whereas the previous survey consisted of seven scans on one side of the chamber. The overlap permitted an evaluation of scan number, distance, and angle on the performance of the technique. Eleven clips (2 × 2 m) were cut out in the area both sets have in common (the upper path in Fig. 5C). Another eleven were cut out of the area exclusive to this study's survey (the lower path in Fig. 5C). These clips were run through the geometric analysis tool in CloudCompare to assess the surface volume of the point clouds in the area using a nearest neighbor input of

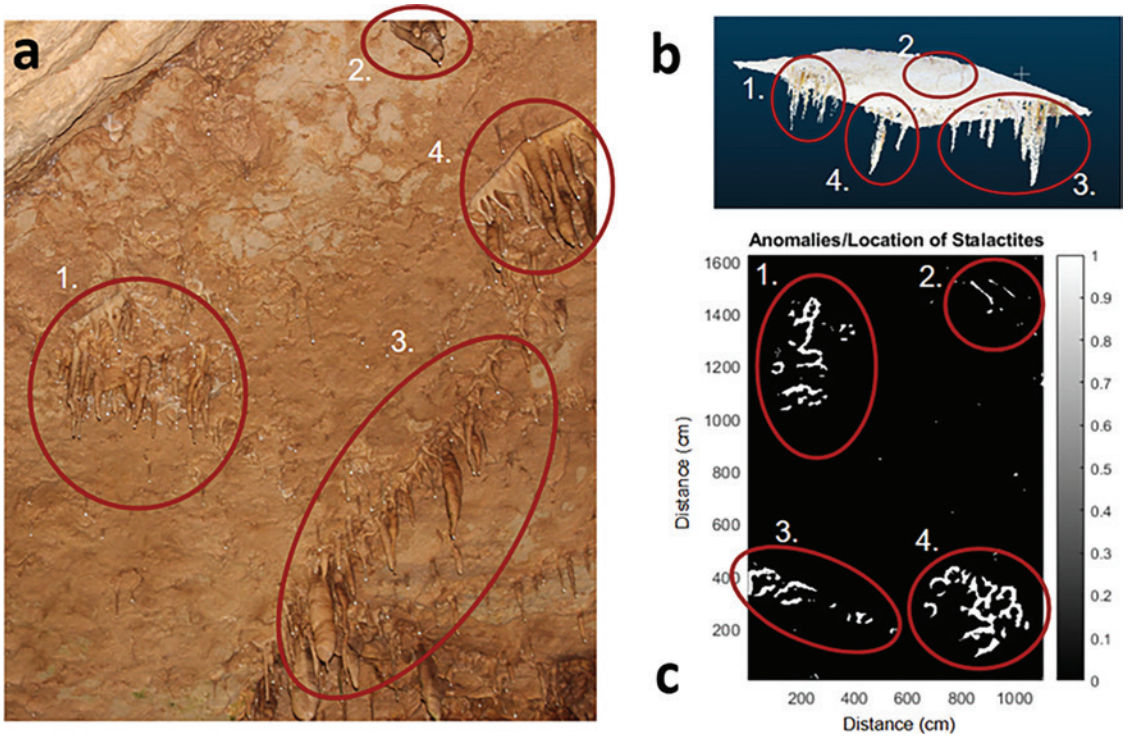


Figure 4. (a) Digital photograph and high-resolution LiDAR image (b) of a ceiling portion for the optimization and validation process. (c) Locations of individual stalactites identified using the morphological analysis located in Purgatory Creek section 2.

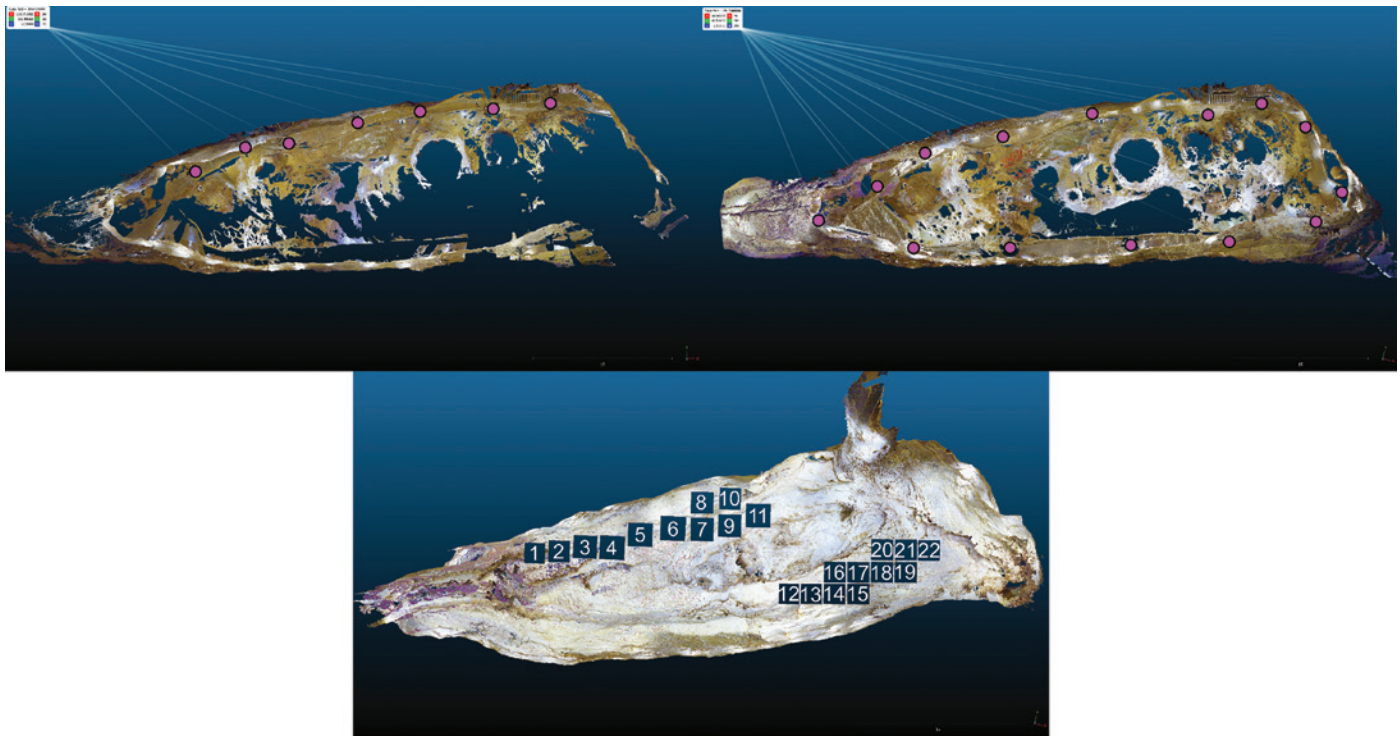


Figure 5. Point clouds of set 1 (a) and set 2 (b) in the Castle of the White Giants. The purple dots represent the location of LiDAR. All 22 clip sections are shown in (c).

1 unit (equivalent to 1 m). The statistics tool is then used on each clip to assess the mean surface density of each clip in points/m^2. This can then be converted to point spacing in millimeters using the equation edited from Heidmann (2018),

$$Point\ Spacing\left(mm\right)=1000\times\sqrt{\frac{1}{Point}Density\left(\frac{p}{m^2}\right)},$$

where point density is calculated as points per m^2.

Distance from the LiDAR location to the ceiling clips and the number of points in each clip can be determined in CloudCompare. The clips were cleaned and subsampled to the optimal resolution then exported to SGEMS files. SGEMS were analyzed to determine total stalactite counts for each clip. The differences between the distances to each clip, the resolution, the point counts, and the final stalactite counts were determined using Cloud Compare. We finally calculated the correlation coefficient for all of these attributes.

Flow Classification Analysis

After determining optimal parameters and resolution, large sections of Pluto's Antechamber and Purgatory Creek were clipped out and analyzed to determine the flow paths in those sections. The matrix flow, fracture flow, and combined flow categories were defined in Mahmud et al. (2015) as follows: Matrix flow is usually represented by smaller isolated stalactites in the cave ceiling. Soda straw stalactites were also included in the matrix flow category and were defined by lower stalactite diameter and higher length/diameter ratio. Stalactites having a cross-sectional area of <75 cm^2 and a connected component aspect ratio of <10 were identified as matrix flow, including the soda straws. Soda straws are defined by a diameter of <10 mm and a length/diameter ratio of >8. Pure fracture flow produces a linear distribution of ceiling stalactites. Stalactite groups with a large cross-sectional area (≥75 cm^2) and a large aspect ratio (>8:1) are identified as fracture flow. Lastly, combined flow forms larger stalactites with a more circular distribution. Stalactite groups with a large cross-sectional area (≥75 cm^2) but a low aspect ratio (<8:1) are identified as combined flow.

A large section containing several complex speleothems was clipped within the Castle of the White Giants for large-scale analysis (Fig. S1). This is along with the 22 sections analyzed in the previous section (Figure 5c) and provides a more complete picture of the flow classification in this chamber. Each of the new clips was cleaned and subsampled to the optimal resolution to analyze for flow classification.

RESULTS

Optimum Point Cloud Resolution

Manual count of stalactites for Purgatory Creek section 1 (Table 1) yielded 119 soda straws and 23 larger stalactites with a total of 142 stalactites. Purgatory Creek section 2 yielded 11 soda straws and 94 larger stalactites, a total of 105 stalactites. Purgatory Creek section 3 yielded 10 soda straws and 36 larger stalactites for a total of 46 stalactites. Sherwood Forest yielded 87 soda straw stalactites and 181 larger stalactites for a total of 268 stalactites.

In Purgatory Creek 2 and Purgatory Creek 3, total stalactite counts tend to decrease as resolution increases. In Purgatory Creek 1 and Sherwood Forest, the total count is largest at 4 mm resolution. When comparing total output stalactite counts in both Purgatory Creek section 1 and Sherwood Forest, considerably larger total stalactite counts were found across all resolutions than those found in visual counts (Table 1 and Fig. S2). When looking solely at soda straw counts, Purgatory Creek has a similar count to the manual count at 8 mm resolution, and Sherwood Forest matches its output count exactly to the manual count at 10 mm (Table 1 and Fig. S3). Large stalactite counts for Purgatory Creek section 1 and Sherwood Forest are still significantly larger than the manual counts at all resolutions. This generated a large difference in total stalactite count (Table 1 and Fig. S4). Stalactite counts for Purgatory Creek sections 2 and 3 were consistent across all resolutions and are most accurate to total stalactite counts at 10 mm (Table 2 and Fig. S3). For Purgatory Creek 3, the large stalactite counts matched the manual count exactly at both 6 and 10 mm. However, the large stalactite count for Purgatory Creek section 2 more closely matched the manual count at 10 mm (Table 1 and Fig. S4). The results determined that 10 mm is the optimal resolution for stalactite counts in this study area.

The moving average window size of 20 cm by 20 cm for the identification of stalactites was found to be optimal for NBC, compared to the 40 cm by 40 cm window used in Mahmud et al. (2015). A smaller window size provides more localized ceiling topography fluctuation, where larger window size results in a smoother surface. The larger window reduces the responsiveness to ceiling topography changes and results in inaccurate stalactite identification.

When verifying the accuracy of the combination of 10 mm resolution and the 97th stalactite percentile threshold of Mahmud et al. (2015), the clips were recompiled with different combinations of resolution and stalactite percentiles (Table 2). For Purgatory Creek 1 and Sherwood Forest, total stalactite counts remain significantly higher than manual counts, and the best match was found at the 97th percentile. Purgatory Creek 3 does match its total and manual counts at a resolution of 12 mm and a percentile of 98. At this combination, Purgatory Creek section 2 shows a difference of over 10 total stalactites and 3 soda straws. The final count is also off by more than 10 stalactites from the manual count for 8 mm, another combination where Purgatory Creek section 3 counts are close (Table 2). Due to the higher level of variance with other parameters, a 10 mm resolution and a threshold of 97th percentile were selected to be the optimal parameters for identifying stalactites at NBC (Fig. S5). To determine the optimal flow parameter, the clip was run with another set of varying thresholds to determine which threshold gave the most accurate flow patterns. When tested with the 95th percentile threshold, large portions of the stalactites are absent from the final flow paths. Lowering this to the

Table 1. Manual counts of stalactites vs automatic counts at different resolutions.

			Counts at Resolution (mm)					
Site Name	**Clip Size (m)**	**Manual Counts**	**2**	**4**	**6**	**8**	**10**	**12**
Soda Straws								
Purgatory Creek 1	2 × 2	119	159	161	124	117	85	62
Purgatory Creek 2	1 × 1.5	11	16	12	13	14	9	8
Purgatory Creek 3	1 × 0.6	10	13	12	13	8	7	6
Sherwood Forest	1 × 2	87	138	140	97	95	83	70
Large Stalactites								
Purgatory Creek 1	2 × 2	23	228	232	201	187	170	162
Purgatory Creek 2	1 × 1.5	94	123	123	107	118	96	108
Purgatory Creek 3	1 × 0.6	38	43	42	38	37	38	31
Sherwood Forest	1 × 2	181	302	308	264	251	276	240
Total Stalactites								
Purgatory Creek 1	2 × 2	142	387	393	325	304	255	224
Purgatory Creek 2	1 × 1.5	105	139	135	120	132	105	116
Purgatory Creek 3	1 × 0.6	48	56	54	51	45	45	37
Sherwood Forest	1 × 2	268	441	448	361	346	359	310

Note. All clips were run with a 97th stalactite percentile and a 93rd flow percentile.

Table 2. Stalactite counts at different stalactite percentiles.

Site Name and Resolution (mm)	Percentile			
	95th	96th	98th	99th
Soda Straw Counts				
Purgatory Creek 1 (8 mm)	95	96	156	192
Purgatory Creek 2 (8 mm)	14	14	12	17
Purgatory Creek 3 (8 mm)	10	9	10	7
Sherwood Forest (8 mm)	246	228	168	96
Purgatory Creek 1 (12 mm)	53	53	97	113
Purgatory Creek 2 (12 mm)	10	9	8	9
Purgatory Creek 3 (12 mm)	10	9	6	10
Sherwood Forest (12 mm)	188	180	150	209
Large Stalactite Counts				
Purgatory Creek 1 (8 mm)	220	202	192	160
Purgatory Creek 2 (8 mm)	194	139	79	56
Purgatory Creek 3 (8 mm)	56	40	37	30
Sherwood Forest (8 mm)	358	300	222	171
Purgatory Creek 1 (12 mm)	165	168	140	129
Purgatory Creek 2 (12 mm)	157	132	82	67
Purgatory Creek 3 (12 mm)	59	39	39	36
Sherwood Forest (12 mm)	305	270	204	172
Total Stalactite Counts				
Purgatory Creek 1 (8 mm)	315	298	348	352
Purgatory Creek 2 (8 mm)	208	153	91	73
Purgatory Creek 3 (8 mm)	66	49	47	37
Sherwood Forest (8 mm)	604	528	390	267
Purgatory Creek 1 (12 mm)	218	221	237	242
Purgatory Creek 2 (12 mm)	167	141	90	76
Purgatory Creek 3 (12 mm)	69	48	45	46
Sherwood Forest (12 mm)	493	450	354	381

93rd percentile corrects this, making this the optimal flow threshold (Figs. S5 and S6).

Relationship between Scan Number, Distance, and Final Counts

This study evaluated the effect of LiDAR scan distance from cave ceiling/walls and scan number on point cloud resolution and final stalactite counts by comparing set 1 (7 scans) to set 2 (14 scans) from the Castle of the White Giants (Fig. 5). The average distance increased for set 1 as we moved to the lower section of the Castle of the White Giants (sites 12–22), which was not covered in set 1. Set 2 has a lower point spacing (average of 4.4 mm) compared to set 1 (average of 5.6 mm), even in areas where set 1 was closer to the clipped area, although the spacing increased in the areas where distance increased. Point counts are higher in set 2 (Fig. S7c). The difference in point spacing does increase in the set with greater scan distances (Table 3 and Fig. S7b). The stalactite counts are larger for set 2 compared to set 1 (Fig. S7d). There is a moderate correlation between LiDAR scan distance and resolution with an R^2 of 0.454 (Fig. S8a). LiDAR scan distance and stalactite count have a weak linear to slightly negative trend with an R^2 of 0.091 (Fig. S8c). Point count and stalactite count have a weak linear negative trend with an R^2 of 0.044 (Fig. S8d). Lastly, LiDAR scan distance versus point count has a weak linear trend with an R^2 of 0.002 (Fig. S8b).

Flow Classification

The primary flow type present in Pluto's Antechamber is matrix flow (Fig. 6). There is a small amount of pure fracture flow and combined flow in Pluto's Antechamber #2 (Fig. 6). Purgatory Creek is mostly dominated by matrix flow, but large sections of fracture flow can be seen in clips Purgatory Creek #7 and Purgatory Creek #8 (Fig. 7). Small amounts of combined flow can also be seen in clips Purgatory Creek #1 and Purgatory Creek #7 (Fig. 7). The Castle of the White Giants consists of mostly fracture and combined flows, with a few patches of matrix flow present in the center of the chamber (Fig. 8). The large pillar in this section has been designated mostly as combined flow (Fig. 9). Considering the entire chamber, fracture flow tends to be located around the perimeter of the chamber, and the center is dominated by combined flow (Figs. 8 and 9). The flow types that represent the higher amount of water movement tend to be located in the deeper section of the caverns, with the shallower sections exhibiting almost entirely slower matrix flow.

DISCUSSION

The method used in Mahmud et al. (2015) is highly sensitive to three parameters that each depend on the morphology and spatial distribution of cave ceiling features. Parameter optimization is the first and most important step in the process because the cave features in NBC differ from those in Golgotha Cave, Western Australia (the study area of Mahmud et al., 2015). These two cave systems vary in size, morphology, age, petrology, climate, and speleothem density. All of these factors can impact how this technique detects stalactites, flow paths, and classification of flow types. NBC is in Cretaceous limestone and dolostone that has been deformed by normal faulting and associated stresses (Gary, 2011). The Golgotha Cave in Mahmud et al. (2015) is formed in Quaternary aeolianite (dune limestone). Lithology and age have significant impacts on cave morphology. The late Miocene faulting that promoted regional erosion and eventual NBC speleogenesis predates the Golgotha Cave by at least 5 million years. NBC's larger, more complex

Table 3. Differences between set 2 and set 1.

Clip #	Surface Density Difference	Resolution Difference (mm)	Distance Difference (m)	Point Count Difference	Soda Straw Difference	Stalactite Difference	Total Stall Difference
1	32880.578	1.017	0.266	241,862	328	447	775
2	15958.520	0.425	−0.357	−120 073	1654	508	2162
3	−11550.734	−0.252	−0.294	−224 358	36	−34	2
4	12564.570	0.568	−0.903	134,586	124	494	618
5	16773.016	0.665	−0.986	256,192	239	109	348
6	6482.945	0.383	−1.530	95,858	96	1309	1405
7	8910.230	0.493	−1.670	77,721	411	491	902
8	−14375.945	−0.278	−1.974	316,246	140	137	277
9	1038.957	0.046	−1.230	−343253	66	373	439
10	16367.500	0.699	−1.544	286,523	46	−6	40
11	−2587.805	−0.085	−1.614	−51974	23	128	151
12	23382.578	2.086	1.267	168,538	22	29	51
13	14896.408	1.384	2.804	75,489	7	268	275
14	11523.445	2.284	7.743	89235	−51	−42	−93
15	2742.477	0.466	8.005	38175	−48	−185	−233
16	20667.787	2.320	5.030	123633	−43	987	944
17	28884.367	2.965	5.191	184,086	11	384	395
18	25496.000	1.559	−0.513	201,724	83	130	213
19	21666.287	3.458	9.017	224034	−5	8	3
20	38105.457	1.258	−2.517	253,467	61	61	122
21	24131.461	0.875	−0.952	173,610	205	181	386
22	37159.783	2.511	1.039	223,500	85	83	168
Avg.	15050.813	1.129	1.103	110,219	159	266	425

Note. Locations of clip numbers can be seen in Figures 7 and 5c.

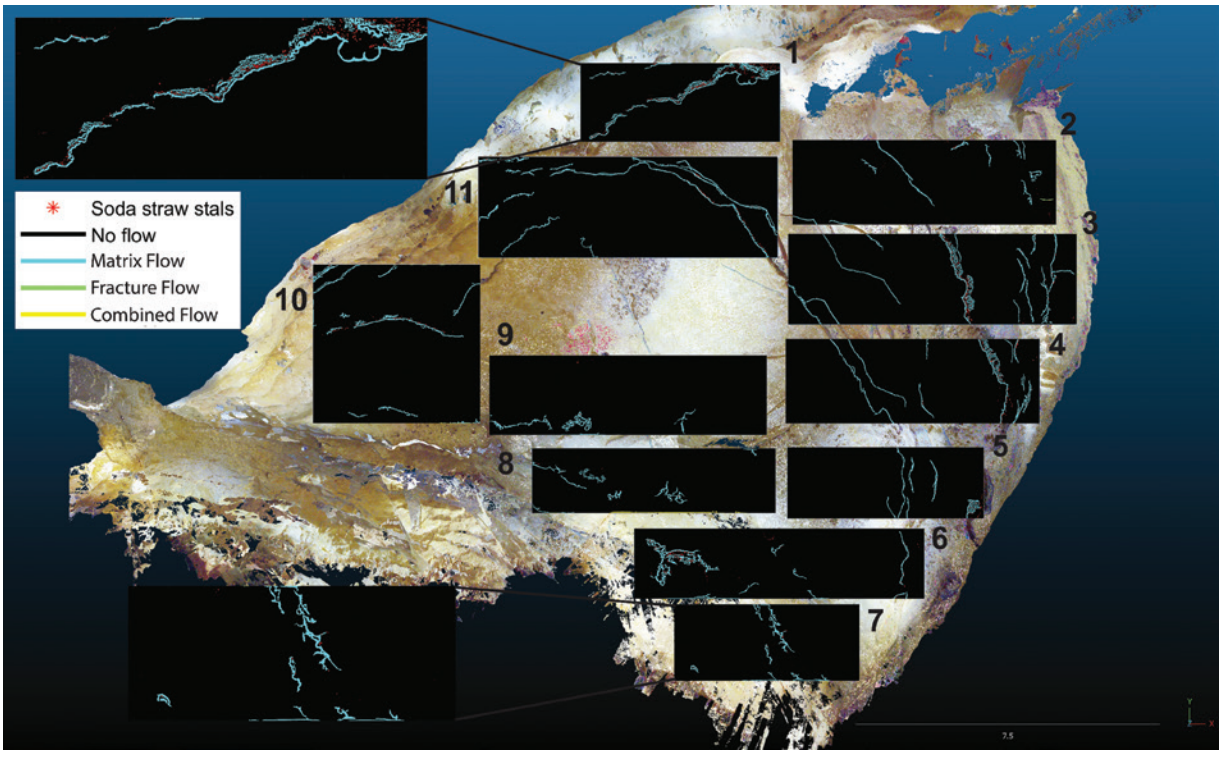


Figure 6. Flow classification maps of Pluto's Antechamber for all 11 clips, showing almost entirely matrix flow represented by blue and some soda straws represented by red asterisks. A small amount of fracture flow represented by green can be seen in clip #2.

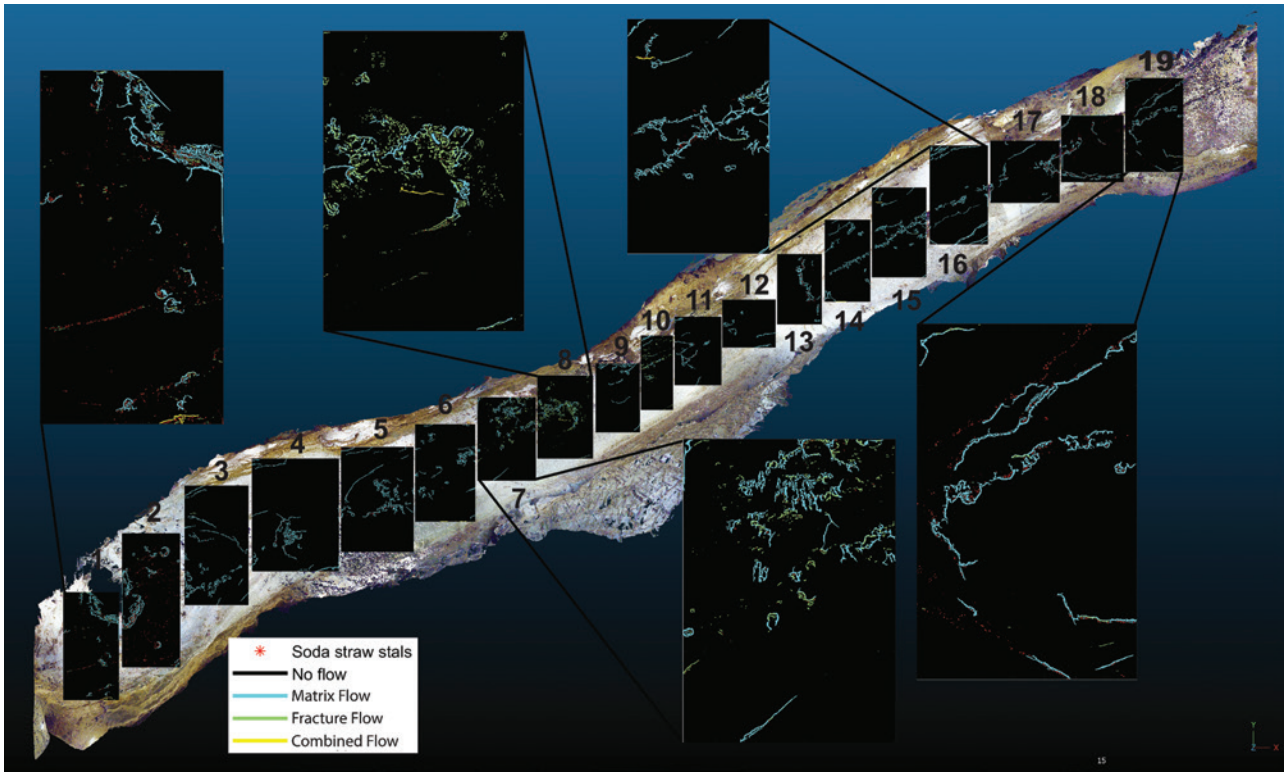


Figure 7. Flow classification maps of Purgatory Creek for all 19 clips showing mostly matrix flow in blue and fracture flow in green. A small amount of combined flow represented with yellow can be seen in clip #1.

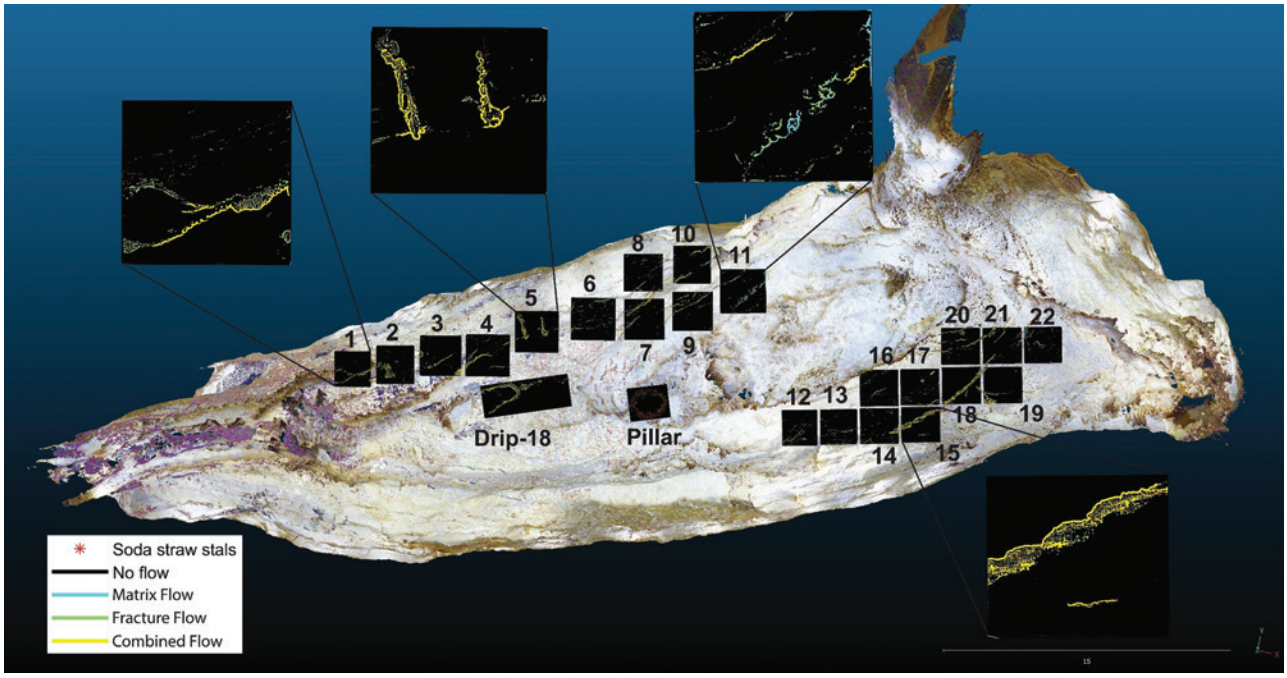


Figure 8. Flow classification maps of the 22 clips in the Castle of the White Giants plus one over drip logger 18 and the main pillar in the chamber. Flow types in the clips consist mostly of flow type 2 (fracture flow) represented by the color green and combined flow represented by the color yellow. A large number of soda straw stalactites were also detected, represented by red asterisks.

stalactites may be due in part to its antiquity, which allows for more opportunities for water flow and speleothem growth. The complexity of this system can also be attributed to two episodes of fracturing and meteoric water interactions, making the current and past movement of water more complex when compared to Golgotha Cave. Stalactites in NBC tend to be larger and cluster closely together, which introduces difficulty in optimizing parameters.

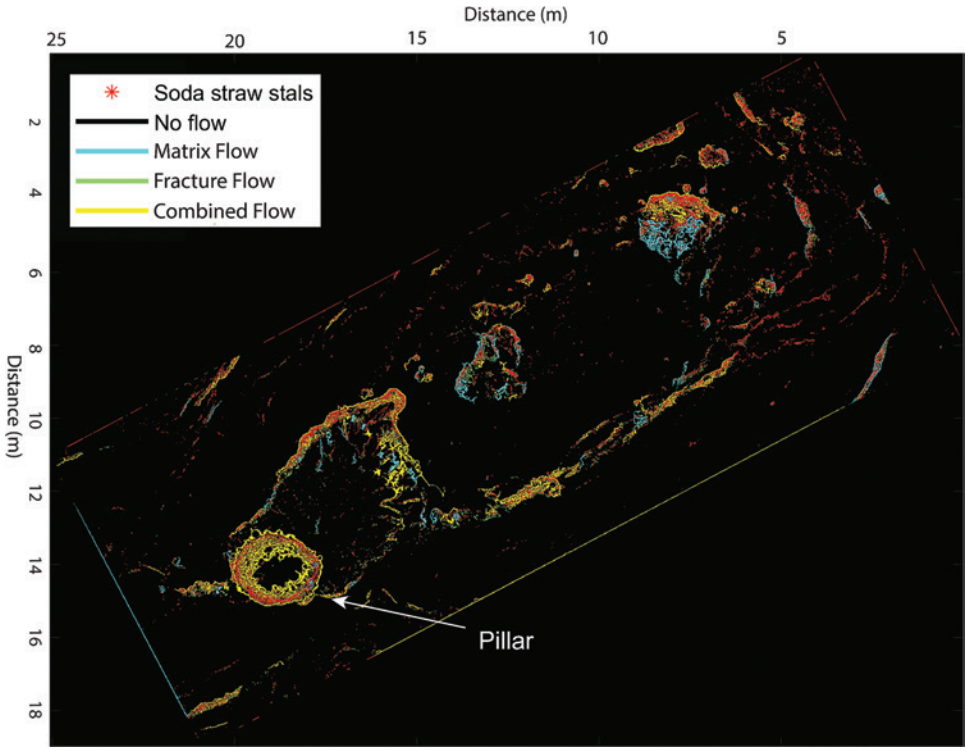


Figure 9. Large clip (9 × 24 m) of the Castle of the White Giants, which shows a very large number of soda straws represented by red asterisks, matrix flow represented by blue and combined flow represented by yellow.

In ceiling areas with larger stalactites, such as cave ribbons, both stalactite and soda straw counts are anomalously high. Purgatory Creek section 1 (Fig. S9, Table 1) examples this. While the method identifies a large number of stalactites, there are only 23 stalactites in the clip and most of the total stalactite count are soda straws (Table 1). The primary speleothem in this ceiling section is an area of cave ribbon (Fig. S9a). Most of the soda straws in this site are located in the center of the clip, away from the cave ribbon. The final flow map struggles to capture these soda straws (Fig. S9b). This is also seen in Sherwood Forest: this area is mostly composed of individual stalactites with no cave ribbon; however, we see an increase (from 181 to 276) in identified stalactites (Table 1). The soda straw locations tend to be more accurate, and the number of misidentified stalactites is sufficiently small, suggesting that individual stalactites are comparatively easier to capture than cave ribbons (Fig. S10).

The final interpolated point cloud representation of cave ribbons is problematic. When observing a 3D representation of the final point cloud, distinct artifacts are seen in the areas of cave ribbon (Figs. 10a and 10b). These artifacts are counted as many separate individual stalactites, increasing the total counts (Table 1). When observing the 3D representations of Purgatory Creek sections 2 and 3, we do not see these artifacts (Figs. 10c and 10d). There, the presence of distinct individual stalactites produces fewer artifacts and permits better identification of stalactites. This introduces extensive investigation when compared to Mahmud et al. (2015), as few cave ribbons were found in the tested areas of Golgotha Cave. It should also be noted that although these affect stalactite counts, their impact on flow identification is minimal. Flow identification groups the stalactites together and uses ratios between aspect ratio and cross-sectional areas of stalactite groups for identification (Mahmud et al., 2015). Due to these factors, it is recommended to perform parameter optimization in areas with smaller stalactites, as the complexity of the stalactites drives the inaccuracy in stalactite counts.

The optimized parameters found in Mahmud et al. (2015) for Golgotha Cave were a stalactite threshold of 97th percentile, a flow threshold of 94th percentile, and a moving average window of 40 cm by 40 cm. We found the same threshold (97th percentile) as the optimal value for stalactite identification in this cavern; however, the flow threshold was the 93rd percentile to capture flow classification accurately. The moving average window size used in this study is 20 cm by 20 cm. The smaller moving average captured more detailed local ceiling fluctuation compared to Mahmud et al. (2015).

Ultimately, there is no strong correlation between any of the point cloud properties and ceiling/wall distance from the LiDAR location. The one with the strongest correlation ($R^2 = 0.45$) is between resolution and distance, which indicates that resolution decreases with increasing distance between the object and LiDAR. There is scant correlation between distance and point count, distance and stalactite count, and point count and stalactite count.

Despite large parametric differences, there are areas shared by the two surveys (set 1 and set 2) where the stalactite count is dramatically different and others where it is statistically invariant. The two scan sets in Castle of the White Giants #5 differ by 348 total stalactites, whereas Castle of the White Giants #19 has a difference of only 3 total stalactites. This is likely due to the presence of LiDAR data voids, holes in LiDAR point clouds due to refraction, absorbance, or scattering of light or shadowing from interfering objects (Heidmann, 2018). When looking at the LiDAR point clouds for Castle of the White Giants #5 and Castle of the White Giants #19, significant data voids can be seen in Castle of the White Giants #5 from set 1 that are not present in set 2 (Fig. 11). These voids are not present in Castle of the White

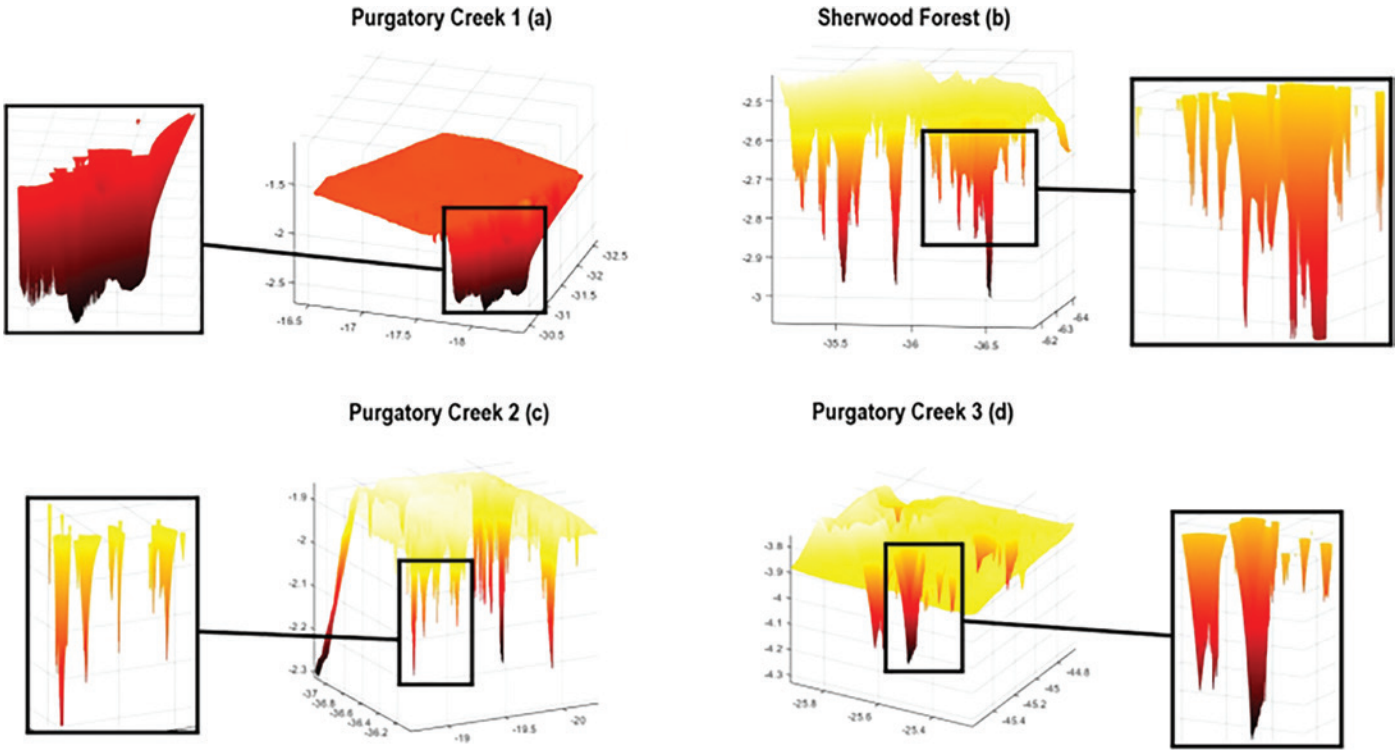


Figure 10. 3D representation of the ceiling for Purgatory Creek sections 1, 2, 3, and Sherwood Forest. Possible artifacts are marked by a black box and zoomed alongside in Purgatory Creek 1 (a) and Sherwood Forest (b). However, they are not present in Purgatory Creek 2 (c) and Purgatory Creek 3(d).

Giants #19 (Figs. 11b and 11e). The presence of these voids is likely due to the interference of the two large cave ribbons present in Castle of the White Giants #5 blocking the LiDAR's view in the affected areas (Fig. 11a). Having seven extra scans in set 2 compensated for those areas' absence on one side. This also explains the difference of over 2000 stalactites in Castle of the White Giants #2. It has a large data void that removes large sections of cave ribbon and stalactites that set 2 has intact (Figs. 11c and 11f). This highlights the importance of obtaining as many scans as possible when conducting a LiDAR survey inside a cave to minimize potential data gaps, hence improving final stalactite counts and producing accurate flow classification maps.

The flow classification maps in both Purgatory Creek and the Castle of the White Giants (Figs. 7 and 8) agree with the observations of the ceiling stalactites present in those two chambers. The Castle of the White Giants has mostly large complex groups of stalactites with large cross-sectional areas, classifying them as both fracture and combined flows (Fig. 8). This is also in agreement with work done in the Castle of the White Giants using drip logger data, where it was found that a majority of water infiltration in the chamber was due to combination flow (Remie et al., 2025). They used multidimensional scaling and agglomerative hierarchical clustering to classify similar drip types based on the drip loggers' time series and identify four unique drip regimes at those point locations within NBC, which are similar to our flow classification. Of the 5 drip loggers present from the Castle of the White Giants, 2 were identified as combination flow, 2 were classified as fracture flow, and the last one was classified as storage overburden flow (similar to soda straw flow in our classification scheme). Purgatory Creek has many more solitary stalactites with smaller cross-sectional areas (Fig. 7). Fracture and combination flow throughout the cavern tend to be located in the larger, deeper sections (Purgatory Creek and Castle of the White Giants). These sections cut through the upper member of the Glen Rose Formation. While matrix flow is present throughout the entire cavern, it is the only flow type to appear in the smaller chambers cutting through the shallower sections of the upper Glen Rose Formation (Pluto's Antechamber).

Overburden thickness remains consistent above both Pluto's Antechamber and Purgatory Creek and thickens over the Castle of the White Giants. Despite this, the Castle of the White Giants contains flow types representing the largest amount of water movement. This suggests that infiltration time in this system is controlled more by secondary porosity and less due to differences in overburden thickness. There are also no significant changes in stratigraphic units across the southern section, as there is only about a 2-degree dip in units with no changes in thickness, which leads to minimal impact from the rock units present. We identify that preexisting conduits are more developed above the Castle of the White Giants and the middle of Purgatory Creek, with other locations above Purgatory Creek and Pluto's Antechamber being less developed (Fig. 12). There is a solution fracture (NBS—38) located 60 m west of the cavern located near the

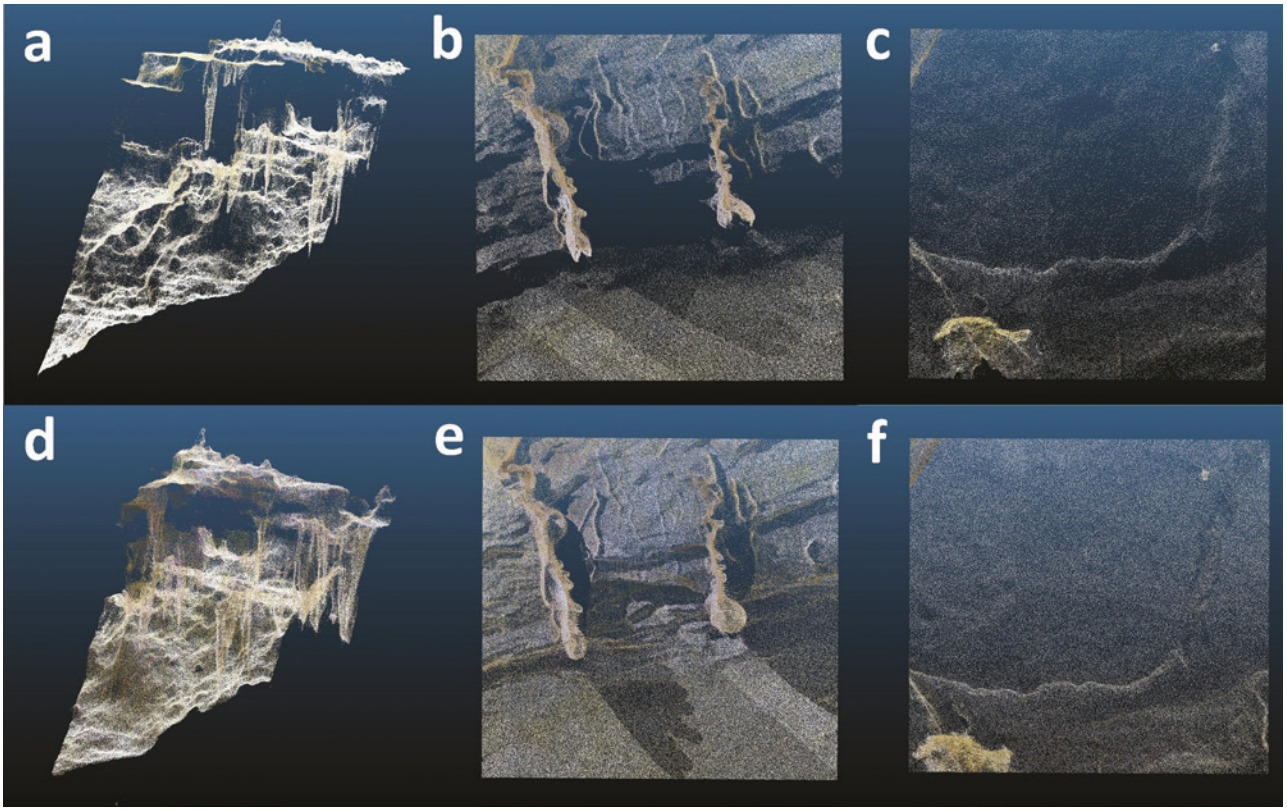


Figure 11. LiDAR point clouds showing the presence of data voids in different clips from the Castle of the White Giants (CWG): (a) showing CWG#2 from set 1, (b) showing CWG#5 from set 1, (c) showing CWG#19 from set 1, (d) showing CWG#2 from set 2, (e) showing CWG #5 from set 2, and (f) showing CWG#19 from set 2.

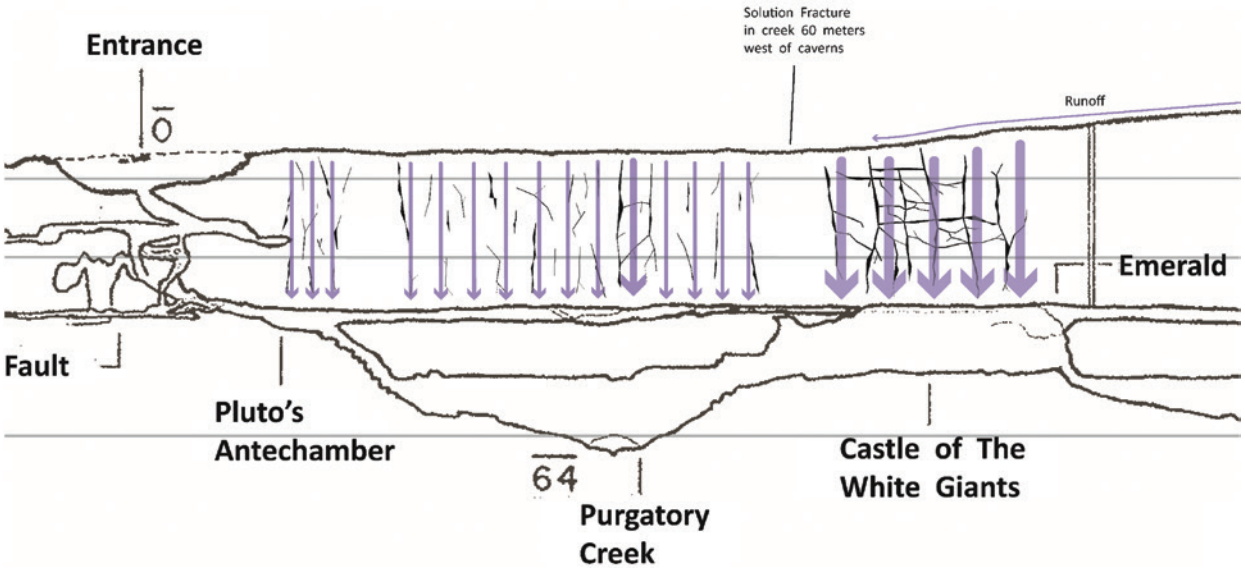


Figure 12. Conceptual framework of potential fracture distribution within the overburden rock layers above the southern section of NBC Discovery Passages. Water movement is represented by purple arrows, with thicker arrows representing higher estimated flow rates and thinner arrows representing lower. Also noted is the location of the solution fracture over the Castle of the White Giants, which serves as a point of water infiltration in the subsurface.

southern section of the Castle of the White Giants (Gary, 2011), which presumably act as an area for water to easily infiltrate in the below cave chamber. Also, an access shaft (NBS-55) above the Purgatory Creek dumps water after rain events straight to the chamber, impacting water availability for subsurface infiltration above this chamber and resulting in less stalactite development in recent years. Another factor to consider is topography's effect on runoff. Elevation

decreases as you move towards the south of the cave, leading to a severe drop in elevation near the entrance, with elevation rising after that. This potentially concentrates runoff in the southern section, leading to a higher quantity of infiltrating water in these sections. Historically, the entrance has been the primary point of water infiltration into the cave, supplying a large quantity of faster moving water to form thinner chambers, such as Purgatory Creek (Gary, 2011). This, however, has changed with the installation of doors that now block major water flow into the entrance section.

Few areas are identified as different flow types within different ceiling sizes. Purgatory Creek 1, for example, is identified as combined flow in the smaller optimization clip but identified as matrix flow in the larger clip, Purgatory Creek 16. The resolution and input parameters are unchanged, so not a likely cause of differences. It is possible that the larger clip simply provided more data for the method to use in identification. Alternatively, it is also possible that larger clips may introduce more error into the identification method.

We find that ceiling areas lacking stalactites are misidentified as matrix flow, for example, in Pluto's Antechamber (Fig. S11). This ceiling area actually has few stalactites, most of them being located along the margins of the chamber. Interbedded clay layers are common to the carbonate rock that hosts NBC, and these layers cause a distinctive stair-step terracing pattern on the ceiling throughout the cavern (Gary, 2011). These terraces are identified as matrix flow, even without the presence of stalactites (Fig. S11). The elevation of the terraces is likely being registered as an anomalous area and misidentified as stalactites.

Flow classification maps failed to identify the recent development of fracture flow. Numerous soda straws oriented along a potentially newly developed fracture at Fig. S9 did not register as fracture flow. These soda straws are too tiny to model them adequately. This can also affect the identification of younger stalactites along fractures, potentially leading to misidentification of matrix or no flow. Smaller stalactites can also lead to misidentification of flow types that represent less water movement.

This technique requires high processing power to run the algorithm and to process the LiDAR point clouds in Cloud Compare. Cloud Compare needs more RAM to render all data points and a faster CPU to calculate surface density. MATLAB also needs a faster CPU to run this algorithm, especially for larger study areas. A majority of the data processing for this study was performed using a computer with 128 GB of RAM and a Ryzen 7950× CPU, which contains 16 processing cores that run at a clock speed of 5.4 GHz. On average, the smaller clips took less than a minute to complete, but larger ceiling sections required 10 min. The large clip in the Castle of the White Giants with a dimension of 25 × 18 m ran 12 h and 35 min to complete. Comparing this to a computer with 256 GB of RAM and an Intel(R) Xeon(R) w5-3335x CPU, which also contains 16 processing cores but a slower clock speed of 3.1 GHz. This computer takes 19 h and 35 min to run the same clip. Hence, CPU clock speed has a greater impact on MATLAB processing, while RAM has a greater impact on LiDAR point cloud rendering.

CONCLUSIONS

Three-dimensional LiDAR surveys of caverns provide a useful tool to understand the preferential water movement in highly heterogeneous karst formations. Our results utilize cavern morphology, predict infiltration water movement, and discover areas of cavern development while leaving the aquifer unaltered.

Optimal parameters for the study of flow types exhibited by speleothems at NBC's Discovery Passages are a threshold of 97th percentile to identify stalactites, a threshold of 93rd percentile to classify flow types, and a 20 cm by 20 cm moving average window. The optimum thresholds are similar to those from prior efforts in cave LiDAR mapping of speleothems, but the optimum moving average window size is reduced to 50% for NBC compared to Golgotha cave (Mahmud et al., 2015). The optimization of input parameters must always be the first step in this method, as cave morphology varies significantly due to factors such as age, lithology, and preexisting structures.

The primary areas containing fracture and combined flows, hosting the most water movement through NBC, are located in the deeper sections of the cavern (Purgatory Creek and the Castle of the White Giants). Fracture flow in Purgatory Creek tends to be consolidated to one area (located in clips 7 and 8 in Fig. 7), with a small fraction of combination flow being present at the end closest to Sherwood Forest. Fracture flow in the Castle of the White Giants tends to be located closer to the walls of the chamber, with large amounts of combination flow being located in the center of the chamber (Fig. 8). This matches the methodology, as the stalactites with higher aspect ratio and cross section area are located more in Purgatory Creek and around the edge of the Castle of the White Giants. Lastly, the center of the Castle of the White Giants is dominated by more circular pillars, driven by combination flow. Areas with slow matrix flow are located in the shallower sections of the cave system (Pluto's Antechamber). Lithologically, fracture flow and combination flow tend to be located in the deeper sections of the cave that cut through the upper member of the Glen Rose Formation.

We estimate that the larger secondary porosity is distributed over the Castle of the White Giants, as we identify flow types representing a higher quantity of flow (combination and fracture) despite the greater overburden thickness. The secondary porosity over Purgatory Creek and Pluto's Antechamber is assumed to be less developed, as those cave ceilings are dominated by matrix flow.

When conducting a LiDAR survey in a cave, it is essential to collect as many scans as possible to avoid data voids in the point clouds. This methodology performed accurately in various ceiling sections within NBC's Discovery Passages; however, there were few caveats while analyzing larger cave ceilings with complex stalactite distributions. Larger stalactites and other ceiling features such as cave ribbons create anomalously large stalactite counts, challenging the optimization process. It is best to optimize input parameters in areas with smaller, simple ceiling sections. There was also anomalous flow classification produced due to the presence of terracing in the cavern, despite no stalactites being visible.

ACKNOWLEDGMENTS

The authors would like to acknowledge the thoughtful reviews of Steven Rosscoe and Andrew Katumwehe on an early draft. The authors acknowledge Elizabeth Elkins for her assistance in the LiDAR survey. Lastly, our sincere thanks to the staff of NBC for their help in the data collection process.

DATA AND CODE AVAILABILITY

The raw data and code used in this study are freely available from this Github repository: https://github.com/mtk7120/Methodology-for-the-Identification-of-Ground-Water-Flow-Types-in-Caverns-using-LiDAR-and-MATLAB-.git

REFERENCES

Barker, R. A., Bush, P. W. , and Baker, E. T. Jr., 1994, Geological history and hydrogeologic setting of the Edwards-Trinity aquifer system west-central Texas: U.S. Geological Survey, Water-Resource Investigations Report 94-4039, 51, p. 27–44, https://doi.org/10.3133/wri944039

Bellian, J., Kerans, C. , and Jennette, D. , 2005, Digital outcrop models: Applications of terrestrial scanning LiDAR technology in stratigraphic modeling: Journal of Sedimentary Research, v. **75**, no. 2, p. 166–176. https://doi.org/10.2110/jsr.2005.013

Brown, K., Mahmud, K., Katumwehe, A. B. , Price, J. D. , and B. Vauter, 2023, Morphological and spatial analysis of cave LiDAR remote sensing to identify karst water infiltration pathways: AGU23, San Francisco, California, 11–15 December, American Geophysical Union, H51P-1304.

Bruun, B., Jackson, K., Lake, P., and Walker, J., 2016, Texas aquifers study groundwater quantity, quality, flow, and contributions to surface water: Texas Water Development Board Report, p. 74–81, https://digitalcommons.usf.edu/kip_articles/4891.

Chang, C and Liu, L., 2021, Investigating the formation of the Cretaceous Western Interior Seaway using landscape evolution simulations: GSA Bulletin, v. **133**, no. 1–2, p. 347–361.

Clark, A. K and Morris, R. R., 2017, Bedrock geology and hydrostratigraphy of the Edwards and Trinity aquifers within the Driftwood and Wimberley 7.5-minute quadrangles, Hays and Comal Counties, Texas: U.S. Geological Survey Scientific Investigations Map 3386, 12, pp. 2–8, https://doi.org/10.3133/sim3386

Ford, D and Williams, P. D., 2007, *Karst Hydrogeology and Geomorphology*: Hoboken, NJ, USA, Wiley, 562 p.

Gary, M. O., 2011, *Geological Assessment for Natural Bridge Caverns Comal County*: Texas, Zara Environmental LLC, 40 p.

George, P. G., Mace, R. E., and Petrossian, R., 2011, Aquifers of Texas, Texas Water Development Board Report 380, 172 p, https://doi.org/10.3133/wri944039

Heidmann, H. K., 2018, Lidar Base Specification Version 1.3: United States Geological Survey, National Geospatial Program, Chapter 4 of Section B: U.S. Geological Survey Standards Book 11, Collection and Delineation of Spatial Data: p. 5–52, https://doi.org/10.3133/tm11b4.

Kastning, E. H., 1983, Geomorphology and hydrogeology of the Edwards Plateau Karst, Central Texas [Ph.D. thesis]: University of Texas at Austin, Texas Speleological Survey Reissue, 657 p., https://texasspeleologicalsurvey.org/PDF/Kastning.pdf.

Klimchouk, A. B., Ford, D. C., Palmer, A. N., and Dreybrodt, W., 2000, *Speleogenesis and Evolution of Karst Aquifers*: Huntsville, AL, USA, National Speleological Society, 514 p.

Lindgren, R. J., Dutton, A. R., Hovorka, S. D., Worthington, S. R. H., and Painter, S., 2004, Conceptualization and Simulation of the Edwards Aquifer, San Antonio Region, Texas: United States Geological Survey Scientific Investigations Report 2004-5277, p. 27–31.

Mahmud, K., Mariethoz, G., Pauline, C. T., and Baker, A., 2015, Terrestrial Lidar survey and morphological analysis to identify infiltration properties in the Tamala Limestone, Western Australia: IEEE Journal of Selected Topics in Applied Earth Observations and Remote Sensing, v. **8**, no. 10, p. 4871–4881.

Mahmud, K., Mariethoz, G., Baker, A., Treble, P. C., Markowska, M., and McGuire, E., 2016, Estimation of deep infiltrating unsaturated limestone environments using lidar and drip count data: Hydrology and Earth System Sciences, v. **20**, no. 1, p. 359–373.

Maclay, R. W and Small, T. A., 1986, Carbonate Geology and Hydrology of the Edwards Aquifer in the San Antonio Area: Texas: Texas Water Development Board Report, p. 13–28, https://digitalcommons.usf.edu/kip_articles/612/.

Pringle, J. K., Howell, J. A., Hodgetts, D., Westerman, A. R., and Hodgson, D. M., 2006, Virtual outcrop models of petroleum reservoir analogues: A review of the current state-of-the-art: First Break, v. **24**, no. 3, p. 33–42.

Remie, R., Mahmud, K., Gary, M., Price, J. D., Katumwehe, A., and Vauter, B., 2025, Using Cave Drip Loggers to Characterize Groundwater Infiltration and Examine Hydrological Response in Cretaceous Karst Formation: EGUsphere [preprint], https://doi.org/10.5194/egusphere-2025-2623.

Shindel, G. M., 2019, Genesis of the Edwards aquifer, *in* Sharp, J. M., Green, R. T., and Shindel G. M., eds., *The Edwards Aquifer: The Past, Present and Future of a Vital Water Resource*: Boulder Colorado, Geological Society of America Memoir, 215, p. 9–18. https://doi.org/10.1130/2019.1215(02).

USGS, 2021, Water Resource Mission Area, Principal Aquifers of the United States, United States Geological Survey: https://www.usgs.gov/mission-areas/water-resources/science/principal-aquifers-united-states (accessed April 28 2025).

Weary, D. J. and Doctor, D. H., 2014, Karst in the United States: A digital map compilation and database, U.S. Geological Survey Open-File Report 2014-1156, p. 23.

SUPPLEMENTAL MATERIAL

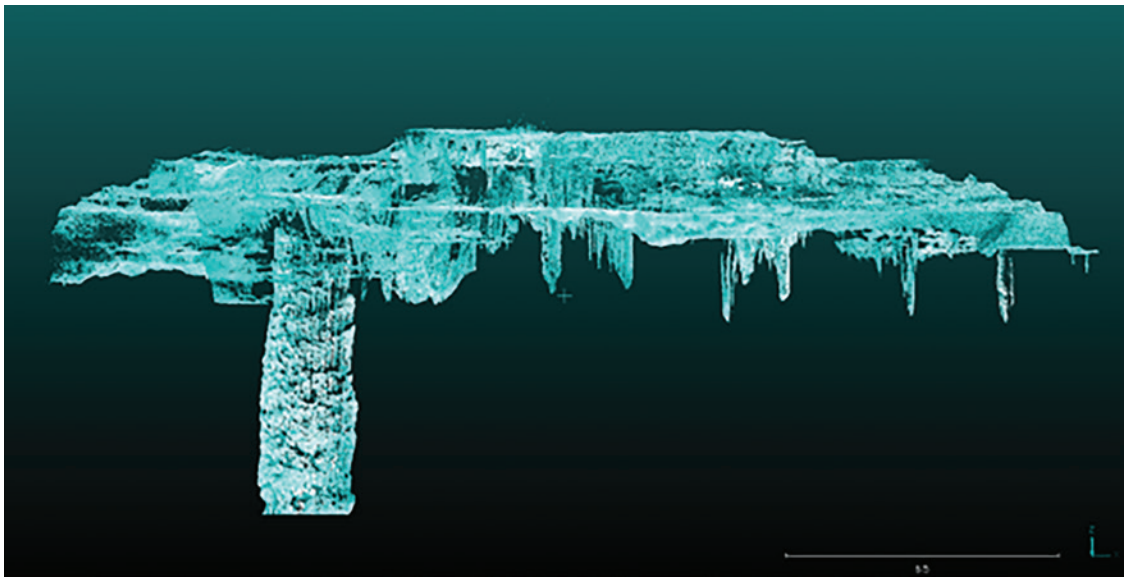


Figure S1. Side view of a large clip (24 × 9 m^2) of the Castle of the White Giants, containing very large and complex speleothems.

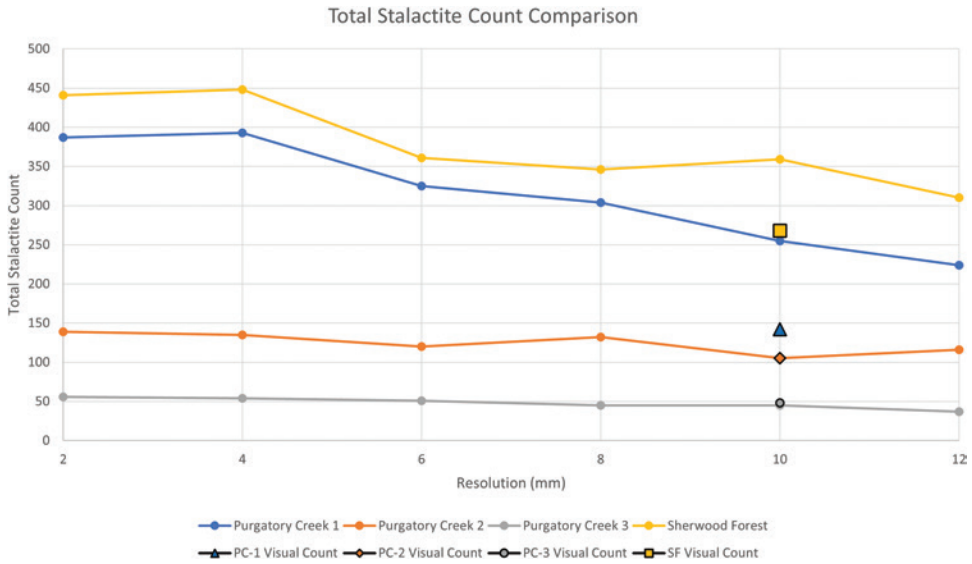


Figure S2. Graph showing total output stalactite counts at the tested resolutions compared to a manual count of the present stalactites. Total stalactite counts at Purgatory Creek section 1 and Sherwood Forest are significantly off from the manual counts, while Purgatory Creek section 2 and Purgatory Creek section 3 are most accurate.

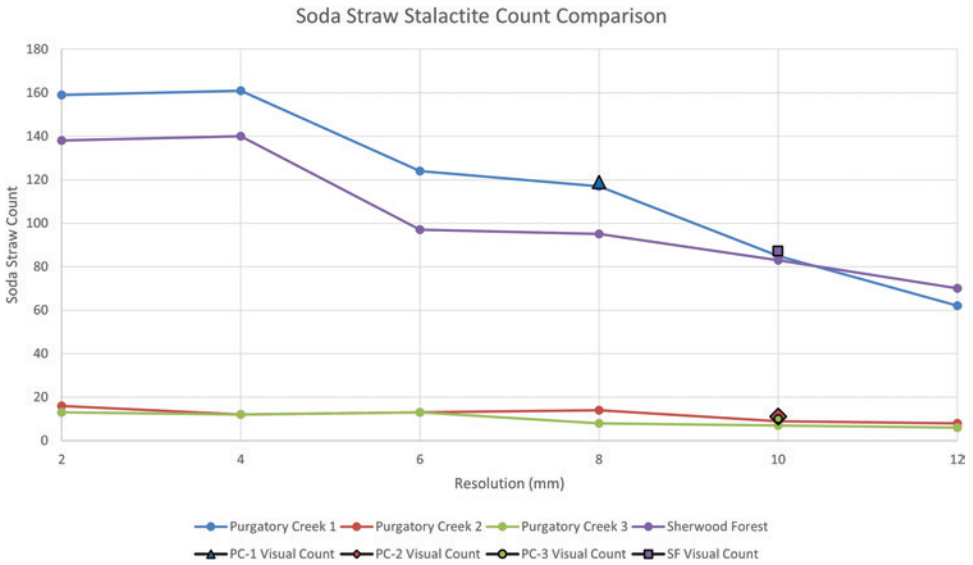


Figure S3. Graph showing output soda straw stalactite counts at the tested resolutions compared to a manual count of the present stalactites. Soda straw counts at Purgatory Creek section 1 are most accurate at 8 mm and Purgatory Creek section 2, Purgatory Creek section 3, and Sherwood Forest are most accurate at 10 mm.

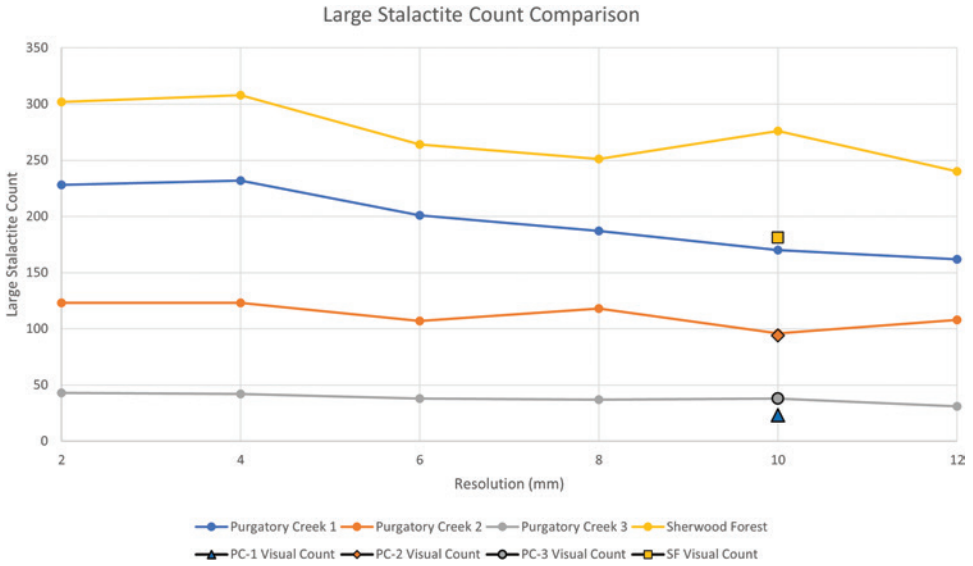


Figure S4. Graph showing output large stalactite counts at the tested resolutions compared to a manual count of the present stalactites. Large stalactite counts at Purgatory Creek section 1 and Sherwood Forest are significantly off from the manual counts, while Purgatory Creek section 2 and Purgatory Creek section 3 are most accurate at 10 mm.

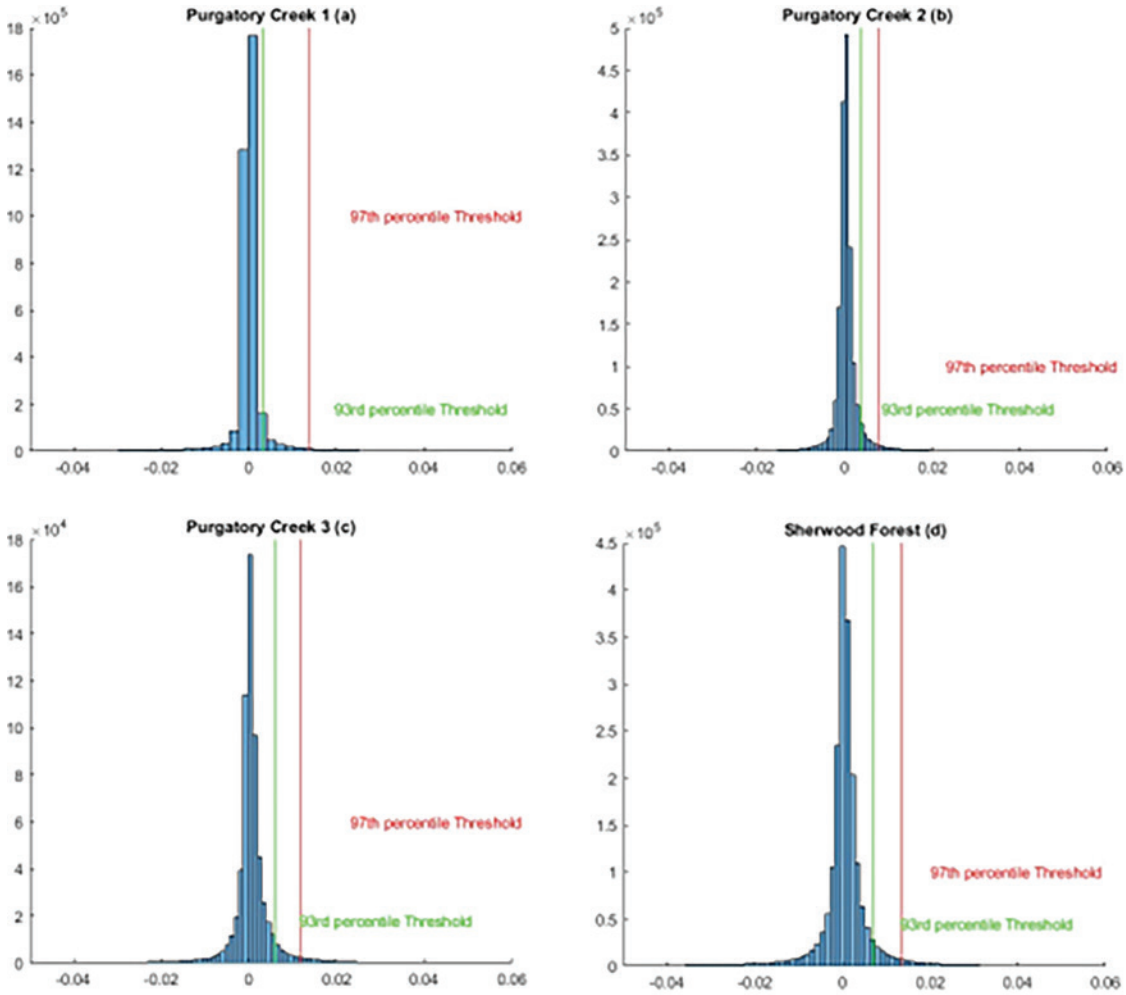


Figure S5. Histogram of anomalies and the thresholds used for stalactite (97th for stalactite identification and 93rd for flow identification) and flow type identifications of Purgatory Creek 1 (a), Purgatory Creek 2 (b), Purgatory Creek 3 (c), and Sherwood Forest (d).

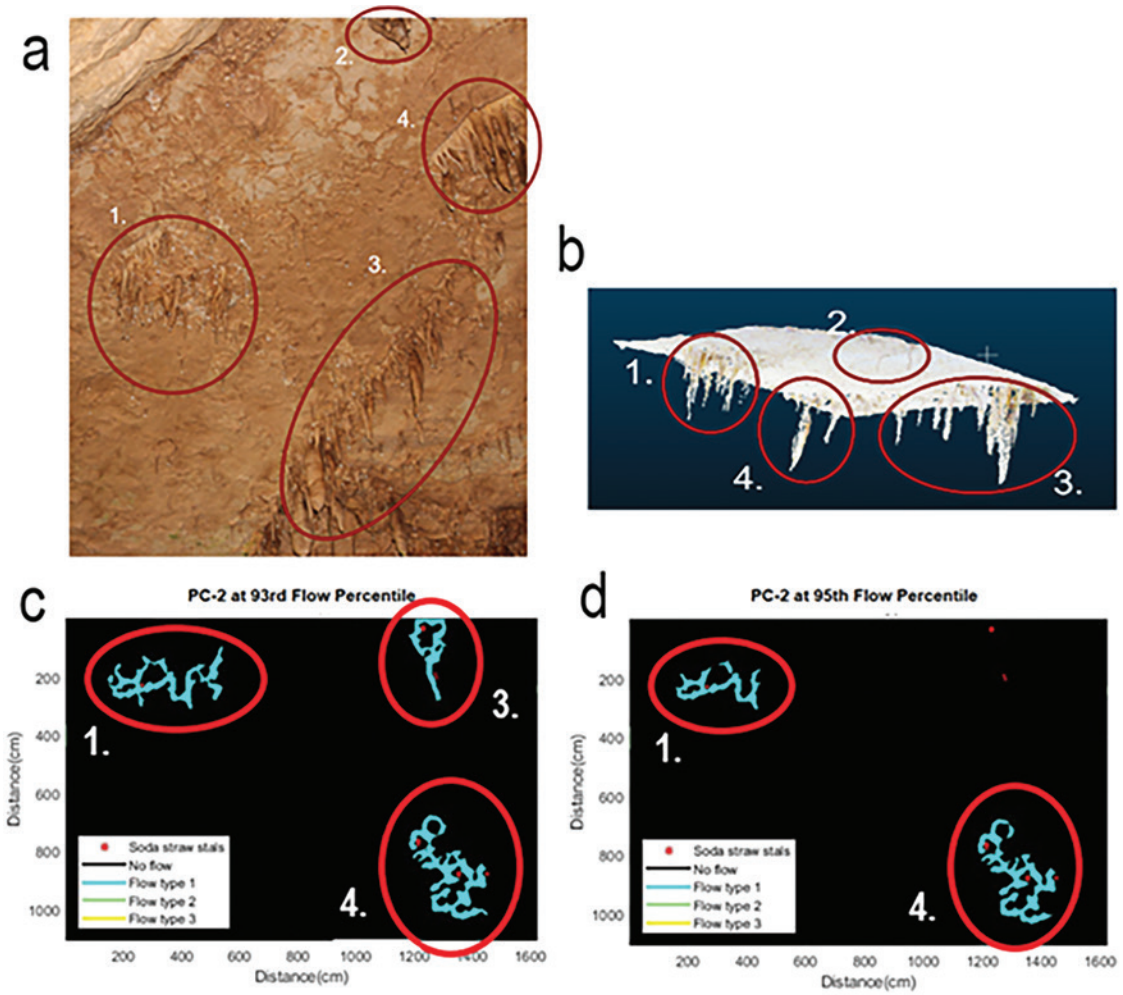


Figure S6. Comparison between flow threshold of a 93rd percentile shown in (c) and 95th percentile shown in (d) compared to a photo of Purgatory Creek 2 (a) and a LiDAR scan of the area (b) (same section used in Fig. 4).

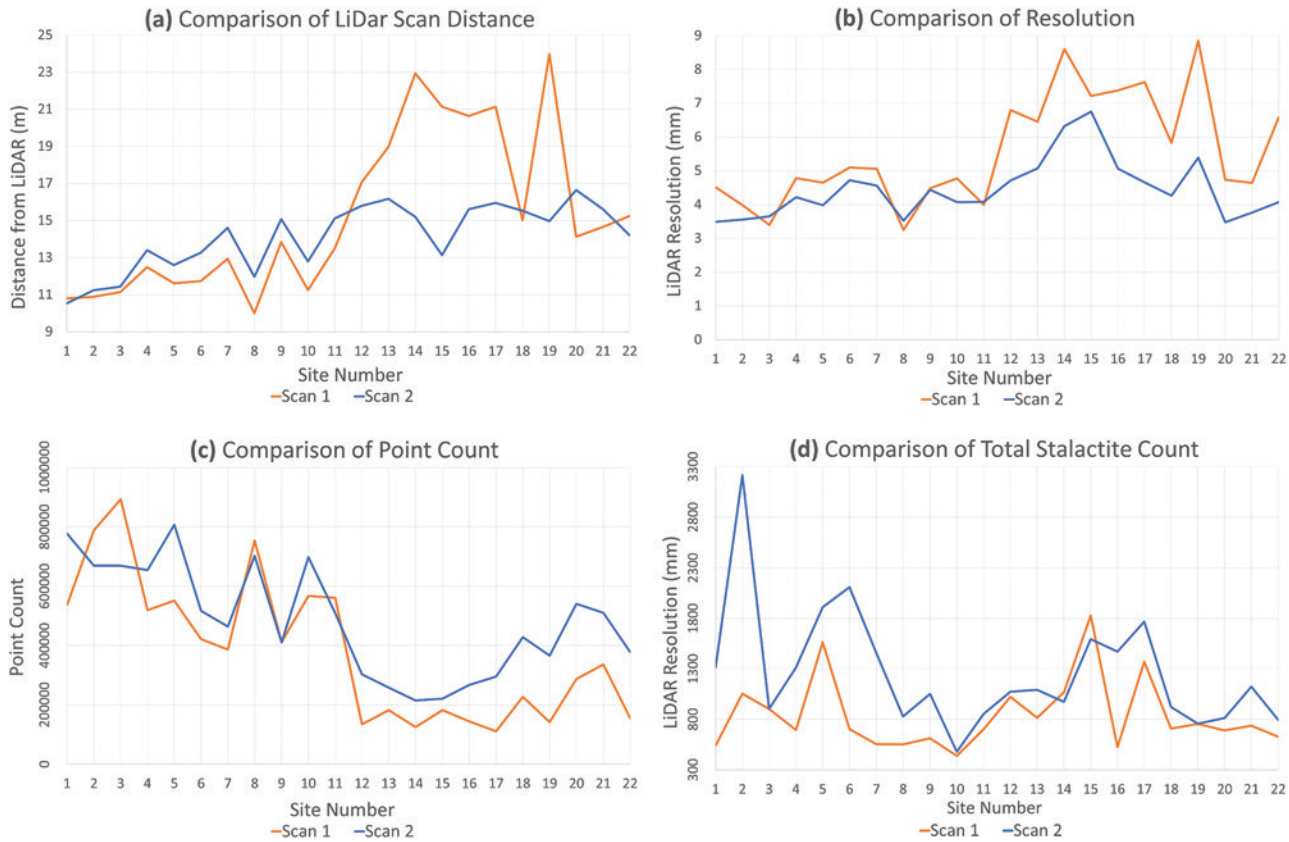


Figure S7. Graphs showing the differences in LiDAR scan distance (a), base point cloud resolution (b), point count of the individual clip locations (c), and total stalactite counts at each location between set 1 (represented by an orange line) with 7 scan locations and set 2 (represented by a blue line) with 14 scan locations (d).

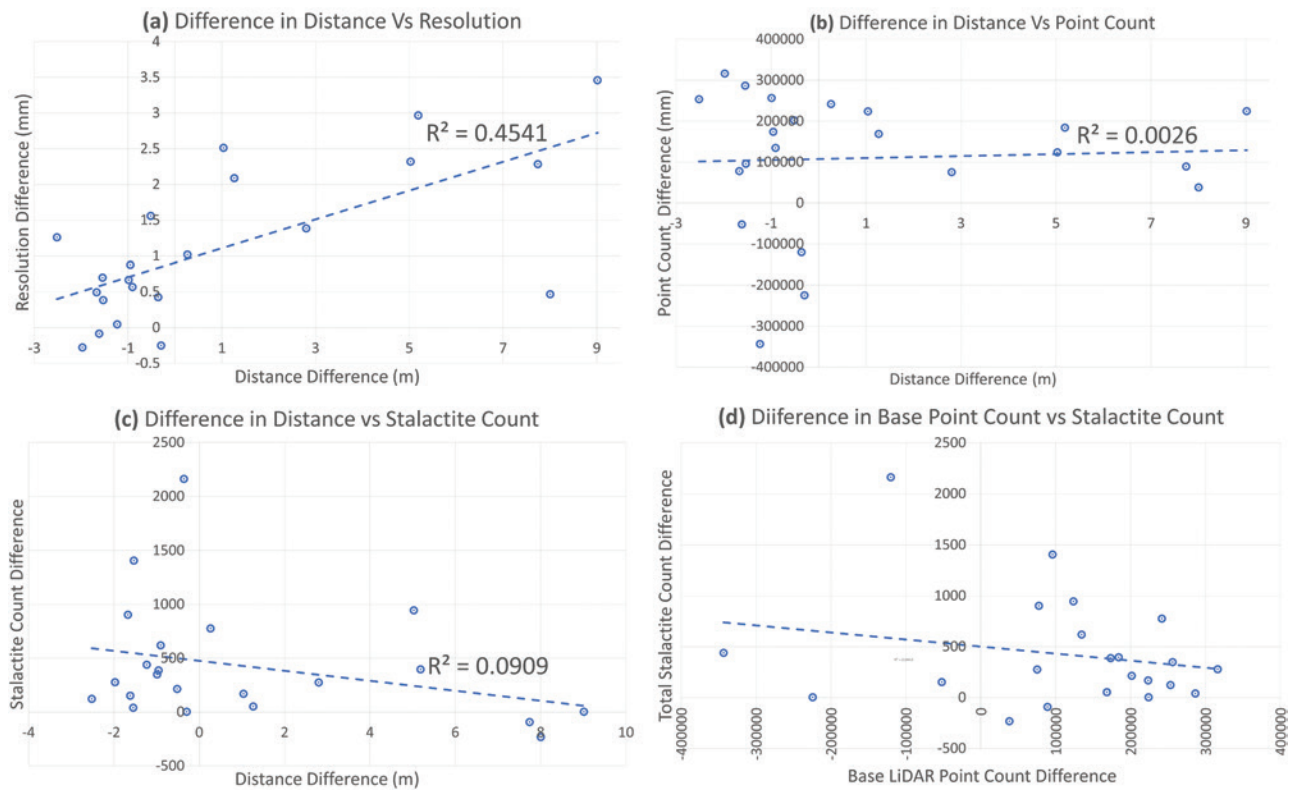


Figure S8. Plots showing the correlation between differences in scan distance and resolution (a), scan distance vs point count (b), scan distance vs stalactite count (c), and point count and stalactite count (d). R^2 values are listed in all subplots.

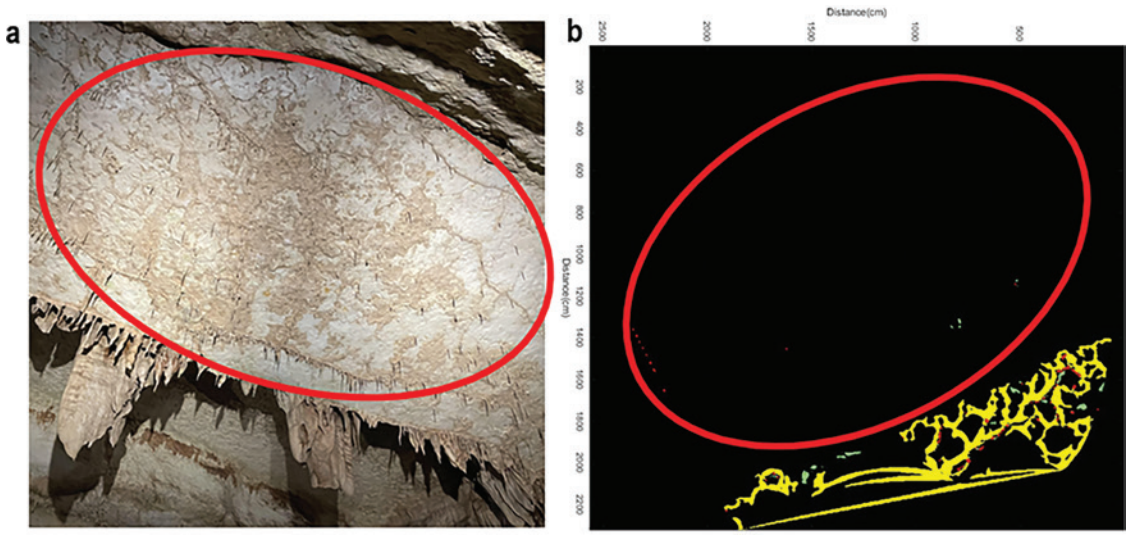


Figure S9. Comparison between an on-site photo of Purgatory Creek (a) and the final flow map of the area showing misidentification of soda straw locations (represented as red asterisk) from the center of the clip to the areas of cave ribbon.

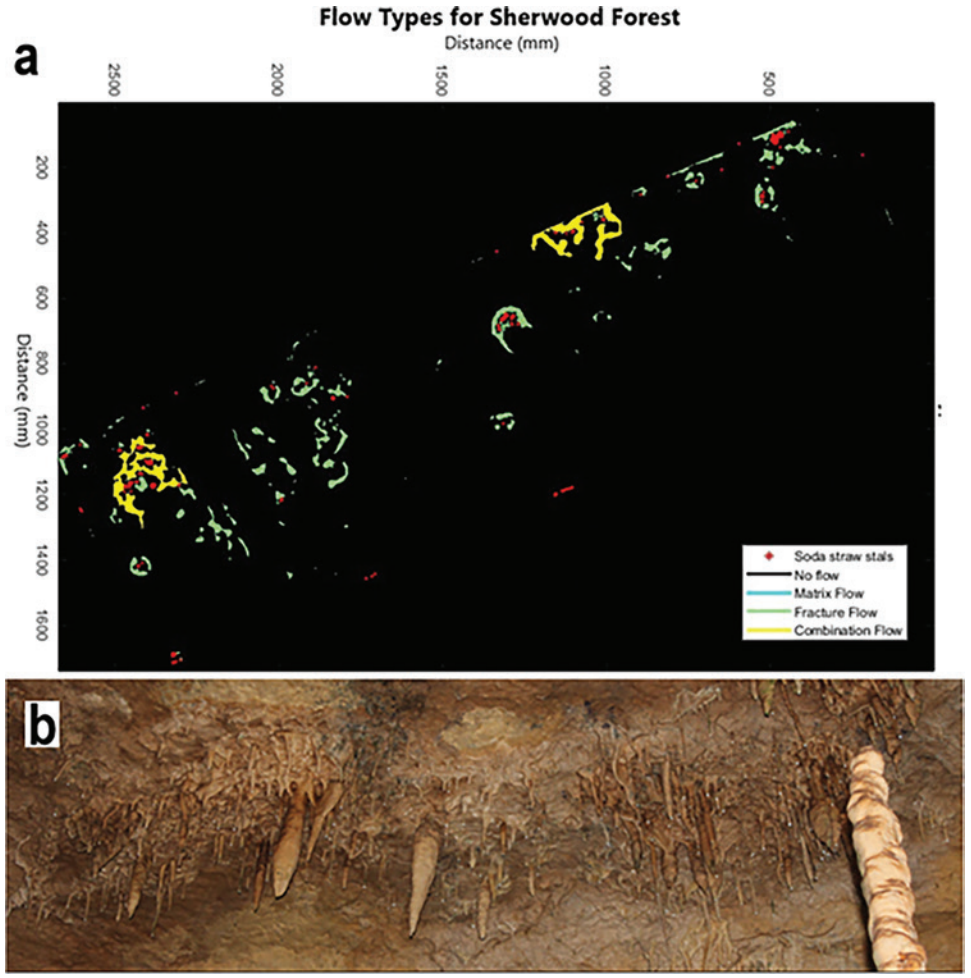


Figure S10. Comparison between an on-site photo of Sherwood Forest (a) and the final flow map (b) of the area showing more accurate identification of soda straw locations (represented as red asterisk).

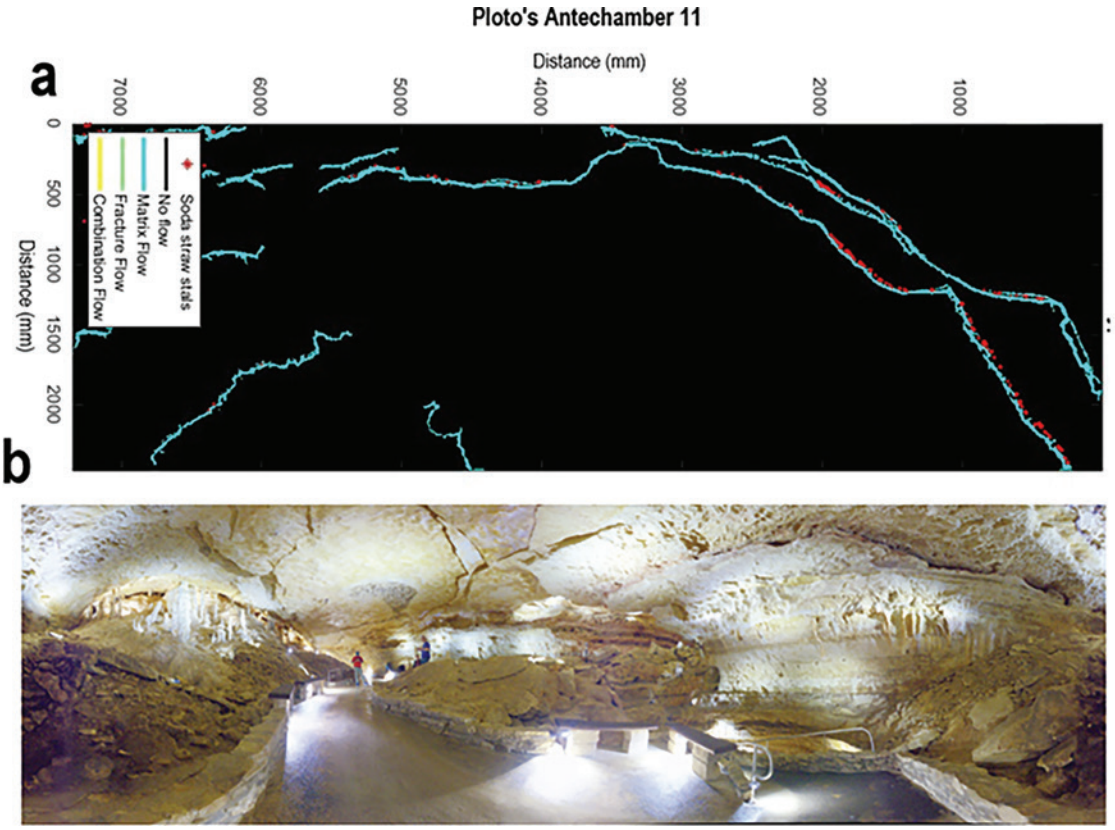


Figure S11. Comparison between LiDAR panoramic image and final flow map showing terracing with no stalactites identified as type 1 flow.

Michael Sean Chenoweth. Morphometric analysis of gypsum depressions using drone imagery at sinkhole flat, Eddy County, New Mexico, USA. *Journal of Cave and Karst Studies*, v. 88, no. 3, p. 100-108. DOI: 10.4311/2022ES0105

MORPHOMETRIC ANALYSIS OF GYPSUM DEPRESSIONS USING DRONE IMAGERY AT SINKHOLE FLAT, EDDY COUNTY, NEW MEXICO, USA

Michael Sean Chenoweth[C]

Abstract

Morphometric analysis is conducted on five karst depressions in Permian-age gypsum of southeast New Mexico. These depressions take on the form of classically shaped blind valleys and sinkholes. Blind valleys in this study are disappearing surface streams composed of multiple tributaries that connect to the main trunk channel leading to a cave entrance. A visible light (RGB) sensor mounted on a quadcopter is used to collect aerial imagery for karst depression mapping and analysis. Field measurements were taken for each depression for comparison with the drone imagery and its derivative layers such as digital elevation model (DEM) and slope. Drone flight elevations were set to 45 m above ground level (AGL) except for one site, which was 76 m AGL, resulting in a spatial resolution ranging from 0.78 to 2.37 cm. A total of 505 images were taken for all sites and mosaiced with photogrammetry software for geospatial analysis. The average field measured depth is 7.5 m and the average DEM measured depth is 5.48 m. DEM measured perimeter ranged from 77 to 675 m and volume ranged from 129 to 4,339 m^3. All DEM measured slopes were less than field measured slopes with the differences ranging from −1° to −39°. Drone orthomosaics and DEM-derived layers make it possible to visualize and quantify the complex morphology of the karst depressions that are not clearly discernible from the ground. Drone imagery can be used to rapidly map and assess gypsum depressions in arid areas.

INTRODUCTION

Gypsum and salt are the most soluble of common evaporite rocks. Evaporite karst features can form rapidly, within days, weeks, or years, whereas carbonate karst features take years, decades, or centuries to form. Water percolates over or through gypsum, causing the formation of sinkholes, disappearing streams, natural bridges, caves, and springs (Johnson, 1997).

Sinkholes are numerous in southeast New Mexico wherever beds of salt and gypsum lie near the surface and the ranchmen fence them to prevent cowboys from riding into them (Lobeck, 1939). Sinkholes and karst fissures formed in gypsum bedrock are common features in the lower Pecos Valley region of New Mexico and West Texas (Land, 2013). In the Delaware Basin region, hypergene karst occurrences are dominated by surficial geomorphic expression of heavy karren development on exposed gypsum surfaces and extensive solutional sinkhole development is often associated with well-developed, dendritic arroyo drainage networks (Stafford et al., 2018).

The Permian Basin of the American Southwest represents the most widespread and pronounced examples of gypsum and salt karst in the United States (Johnson, 1997). Permian evaporites in southeastern New Mexico include gypsum, anhydrite, and salt. Dissolution has produced hundreds of individual karst features including collapse sinks, karst valleys, blind valleys, karst plains, caves, and breccia pipes (Bachman, 1987).

A blind valley is a gorge that terminates abruptly at a point where the stream sinks (Gilli, 2015). Blind valleys have been documented by other researchers in southeastern New Mexico. Blind valleys commonly develop in the thick upper sulfate of the Tamarisk Member in the Nash Draw karst valley 30 km east of Carlsbad, New Mexico (Powers et al., 2006). Bachman (1987) suggests that in semiarid southeastern New Mexico, the term “blind arroyo” is a more descriptive name for “blind valleys.” Blind arroyos are small, deep flat-bottomed gullies with intermittent flow occurring after heavy rain. A steep bank marks the termination of the arroyo at a collapse sink or cave. Half blind arroyos back up headward in the arroyo during intense rainfall. Stafford et al. (2008) conducted field studies in the Castile Formation evaporite karst region of southeast New Mexico, measuring sinkhole length, width, and depth. Their findings were that sinkhole area and volume varied widely within the surveyed sites (see pages 37–38 for detailed morphometric measurements).

Numerous sinkhole studies using drones and LiDAR have been published effectively delineating and quantifying doline physical attributes (Silva et al., 2017; Kim et al., 2019; Mihevc and Mihevc, 2021). A literature gap exists in the use of visible light (RGB) drones and evaporite karst surface morphology. Fewer studies have used drones to map and measure sinkholes using visible light (RGB) sensors. Gijón-Yescas et al. (2021) compared drone-derived orthomosaics to Google Earth images of a large complex cenote in the Yucatan, Mexico. Drone imagery was able to obtain much finer measurement results compared with satellite-derived Google Earth imagery. Even for a large depression, such as cenotes in urban areas, drone imagery is superior to high-resolution satellite data.

Department of Chemistry & Geosciences, Jacksonville State University, Jacksonville, Alabama 36265
[C]Corresponding author: mchenoweth@jsu.edu.

STUDY AREA

The study area is situated in the northeastern Chihuahuan Desert Great Plains region (Medellín-Leal, 1982) about 16 km west of Brantly Lake State Park in Eddy County, New Mexico, USA (Fig. 1). The Pecos Valley forms the southern end of the Great Plains where the surface is almost flat with an average altitude of 750 m (Medellín-Leal, 1982). Hydrologically, the study area is located in the USGS Rio Grande Region. The karst features discussed in this paper are within the Long Draw–South Seven Rivers Hydrologic Unit (HUC12 130600110505). The study site can also be found on the USGS 7.5-min topographic quadrangle named Foster Ranch, NM (Latitude +32.5412°, Longitude −104.5857°).

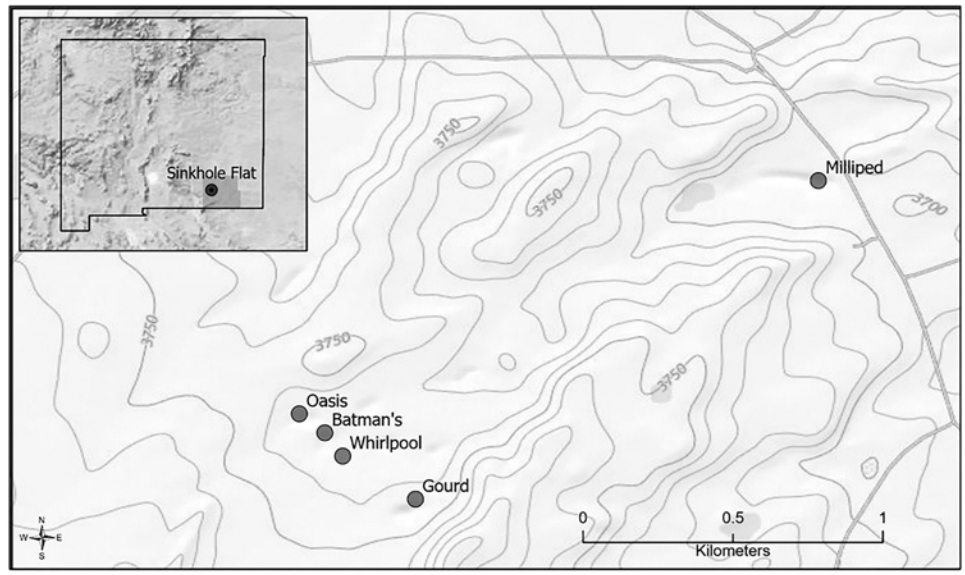


Figure 1. Location of karst depressions in this research paper at Sinkhole Flat in Eddy County, New Mexico, USA (USGS 7.5 topo Foster Ranch, NM).

Gypsum karst is best expressed where mean annual precipitation is low (Ford and Williams, 2007). Gypsum karst is fairly common in the semiarid to arid regions of the western United States (Johnson, 1997). The Köppen climate classification for Carlsbad, New Mexico, is cold desert (BWk). The average annual maximum temperature is 25.8 °C, and the average annual minimum temperature is 8.4 °C. The average annual total precipitation is 32.6 cm, with an average snow depth of 11.2 cm (WRCC, 2022). The Lower Sonoran life zone in the Pecos Valley is mainly composed of mesquite, black grama grass, *Optunia*, *Yucca*, *Larrea*, and *Acacia* (Beck and Hasse, 1969; Cokendolpher and Polyak, 1996).

Sinkhole Flat is located in the evaporite facies of the Grayburg Formation (Permian/Guadalupian Series/Artesia Group), which consists of sandstone, gypsum, anhydrite, dolomite, and red mudstone. The Artesia Group is the shelf or back reef facies of the Guadalupian Series including the Queen Formation overlying the Grayburg Formation (Tait et al., 1962). Gypsum is the dominant evaporitic rock at the surface where karst features including collapse sinks and karst valleys are prominent in the Artesia Group north of Carlsbad, New Mexico (Bachman, 1987). The gypsum caves of Sinkhole Flat form along and within surface drainage systems and probably migrate with the denudation of the region where the soluble Permian gypsum units crop out. These caves formed relatively fast and are probably short-lived (Cokendolpher and Polyak, 1996).

METHODS

Field measurements were taken for each depression for comparison with the drone imagery and its derivative layers such as the digital elevation model (DEM) and slope. Field measurements focused on the physical characteristics associated with the stream sink area. All depressions in this study have a cave associated with their deepest point. Slope and joint orientations were taken with an analog compass and clinometer. The magnetic declination for the compass was set to +6° East. The internal slopes of each karst depression were measured in the four cardinal directions (north, south, east, and west) at a height of approximately 1 m above the lowest point of the depression (Chenoweth, 1997). The depth of the karst depressions was measured from the bottom up. The top was defined as the elevation of the highest closed contour surrounding the depression. To determine this top edge accurately, careful field observations were made. Each contour line was identified and confirmed by walking the perimeter of the depression and using a GPS for elevation data. Length and width measurements were made with a standard field measuring tape after each karst depression's highest closed contour was determined through careful observation in the field. The length of each depression was defined as the longest straight line corresponding to the ephemeral surface stream entering the karst depression. The width was then measured as the longest line perpendicular to this length.

Each depression was surveyed using a small, unmanned aircraft system (sUAS) or drone. The DJI Phantom 4 Pro Version 2 is a quadcopter that comes with a visible light (RGB) camera, and it costs approximately $1,200. This drone was selected primarily for its mechanical shutter, which eliminates rolling shutter distortion when capturing still images during autonomous flights. The camera has a 2.54 cm (1 in.) CMOS sensor to record 20 megapixel still images. Image

size settings included a 3:2 aspect ratio with a width of 5,472 pixels and height of 3,648 pixels. Images and videos were stored on a high-speed Micro SD card (64GB, UHS-3) inserted into the drone fuselage.

Drone mission planning and automated drone flights were performed using Pix4D Capture software operating on an Apple iPad mini connected to the drone's remote control or ground control station (GCS). Image overlap was set to 70% forward and 60% side for all missions (Fig. 2). Flight elevations for each drone survey were set to a constant altitude of 45 m above ground level (AGL) from the initial takeoff point adjacent to each karst depression, except for Gourd BV, where the elevation was 76 m AGL (Table 1).

Drone2Map (ESRI version 2.3.2) is a photogrammetry software used to create orthomosaics and digital terrain models (DTMs) or digital elevation models (DEMs) from images taken by the drone over each karst depression. The software also generates 3D point clouds enabling volumetric measurements of features in a scene. The processing time for each drone survey dataset in Drone2Map averaged approximately 40 min using a high-performance desktop workstation. Orthomosaics and DEMs were exported from Drone2Map into ArcGIS Pro (ESRI version 2.9.1) for integrative geospatial analysis.

The drone-derived DEM was used in ArcGIS Pro to create contours, slope models, linear, area, and volumetric measurements. Perimeter, area, and volume (Table 4) were calculated using the upper closed depression contour associated with each karst depression (Figs. 4–6). Contours for the digital elevation models (DEMs) of each study site were generated, originating from the lowest point of the depression. The lowest point for each DEM was calculated using a raster tool in ArcGIS Pro called Highest or Lowest.

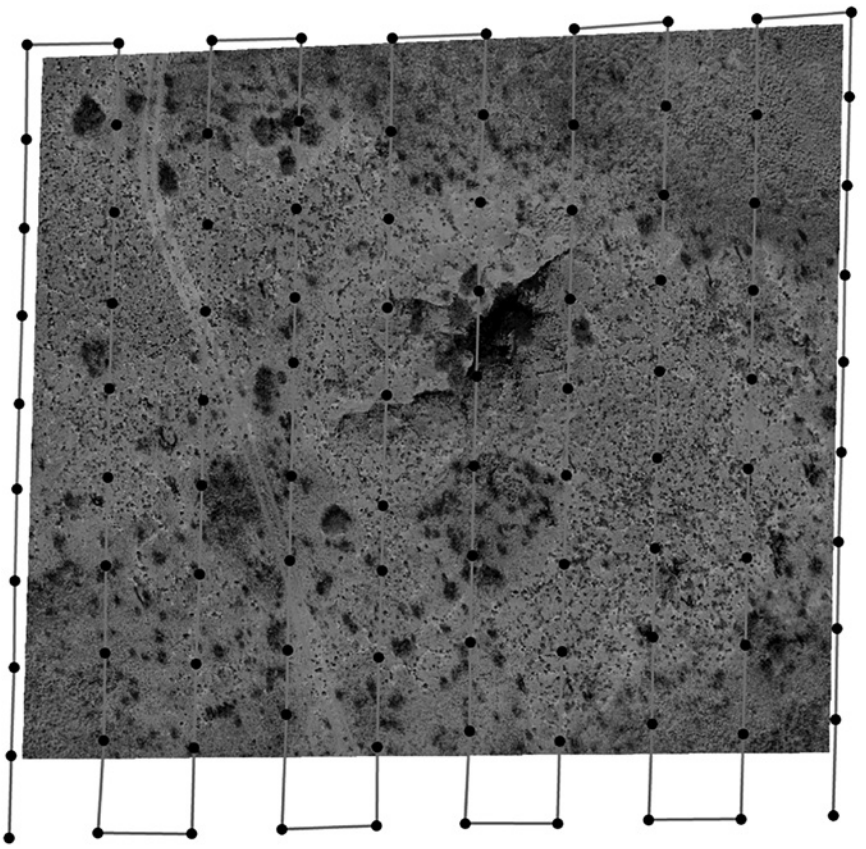


Figure 2. Drone flight lines for Whirlpool Sink. The dots show the location of each photograph taken (100 images total). Orthomosaic shown in the background is a clipped version of the original mosaic. Note dirt track on the left side of sinkhole.

Table 1. Drone autonomous flight attributes for each depression.

Site Name	# Photos	Flight Elev. (m)	Spatial Res. (cm)
Oasis	135	45	0.78
Batman's	57	45	0.78
Whirlpool	100	45	0.81
Gourd	25	76	2.37
Milliped	188	45	0.92

RESULTS

Field Investigation

The depressions in this study, except for Whirlpool sink, are blind valleys (BVs) with a cliff foot sink point at the downstream blind end. Well-developed rillenkaren, reminiscent of tropical karst, is present on various steeply sloped areas throughout the gypsum depressions. The names of these depressions come from round metal Bureau of Land Management (BLM) identification plaques bonded to the bedrock outside of each cave entrance (Oasis, Batman's, Whirlpool, Gourd, Milliped). The BLM has confirmed that the spelling of Milliped is correct.

Oasis blind valley (Fig. 3) has a cave with 7-m-high ceilings and a meandering serpentine passage typical of gypsum caves explored in this area. The major joint orientation is 50° (Table 2) and the depth is 7.62 m (Table 3). The field measured length is 105.46 m and the width is 77.72 m (Table 4). The field measured internal slopes are as follows: Slope north (Sn) 48°, Slope east (Se) 85°, Slope south (Ss) 40°, and Slope west (Sw) 30° (Table 5).

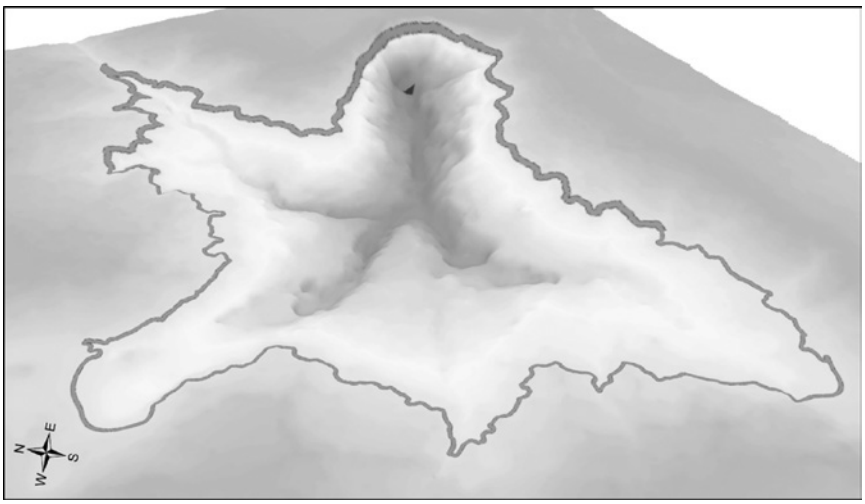


Figure 3. Oasis blind valley DEM 3D view (scale varies in this perspective). The solid line delineates the upper closed contour and the triangle is the lowest point in the DEM.

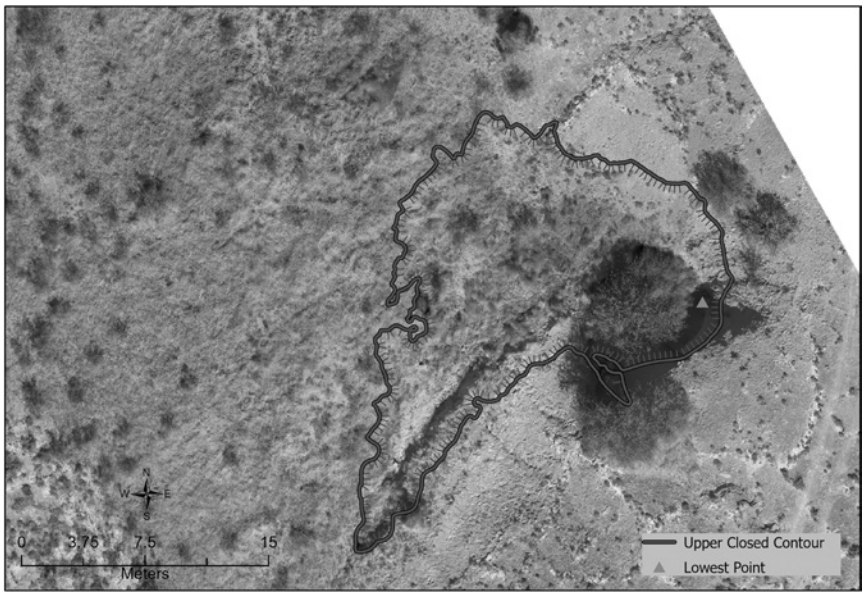


Figure 4. Batman's blind valley orthomosaic shows surface drainage entering from the NNE and SSW. Large mesquite tree adjacent to the lowest point.

Batman's cave (Fig. 4) is also a blind valley with a 1.7-m-high cave entrance facing north under a 3.5-m-high cliff (Table 3). Several surface streams converge on the depression and lead to the cave entrance. A large mesquite tree grows near the cave entrance in the base of the depression. There is a well-beaten path to the bottom where cattle take respite from the heat. The major joint orientation is 110° (Table 2) and the depth is 3.05 m (Table 3). The length is 16.46 m, and the width is 13.41 m (Table 4). Internal slopes are as follows: Sn 30°, Se 40°, Ss 90°, and Sw 42° (Table 5).

Whirlpool sink (Fig. 5) is deep, with few surface tributaries, and steep vertical walls. There is a cave entrance about 2 m high and 1 m wide in the southwest part of the sinkhole beneath a steep slope. Rillenkarren is particularly abundant, and a layer of red sandstone is exposed at the base. The major joint orientation is 30° (Table 2), with a minor joint orientation of 120°. The deepest section is at the cave entrance, measuring 9.14 m from the surface (Table 3). The length is 19.81 m and the width is 17.67 m (Table 4). Internal slopes are as follows: Sn 50°, Se 78°, Ss 72°, and Sw 80° (Table 5).

Gourd blind valley (Fig. 6) has a tight squeeze cave entrance about 45 cm high and 50 cm wide with a major joint orientation of 95° (Table 2) and a depth of 7.01 m (Table 3). Drainage flows into the depression from the east. The length is 19.81 m and the width is 13.41 m (Table 4). Internal slopes are as follows: Sn 40°, Se 20°, Ss 40°, and Sw 50° (Table 5).

Milliped blind valley (Fig. 7) or Barbed Wire Cave (Cokendolpher and Polyak, 1996) is the largest blind valley by volume (Table 4) in this study and is located northeast of the main cluster of depressions (Fig. 1). This elongated blind valley is oriented east–west with a cave entrance on the topographically lower eastern side. The major joint orientation is 60° (Table 2) and the deepest point is 10.67 m (Table 3). Internal slopes adjacent to the cave entrance are as follows: Sn 75°, Se 62°, Ss 90°, and Sw 20° (Table 5). The length and width of this depression were not measured in the field due to the large size and safety considerations near the precipice edges. Primary drainage flows into the depression from the west with several first order surface tributaries entering the trunk channel. There are three other prominent geomorphic features associated with this depression: a karst window, a small sinkhole, and a stream meander. The karst window is located about 15 m east and upslope from the cave entrance and the vadose stream passage has a joint orientation of 160° (Table 2). The small sinkhole (Fig. 7) is in the main trunk channel about 96 m west of the cave entrance. It is about 70 cm deep, with the same joint orientation as the karst window, crossing the wall of the blind valley. The stream meander is located about 22 m west of the cave entrance.

Geospatial Investigation

The number of survey photographs taken for each depression ranged from 57 to 188, with a total of 505 images (Table 1). The spatial resolution or pixel size is directly related to flight elevation and ranged from 0.78 to 2.37 cm. Gourd

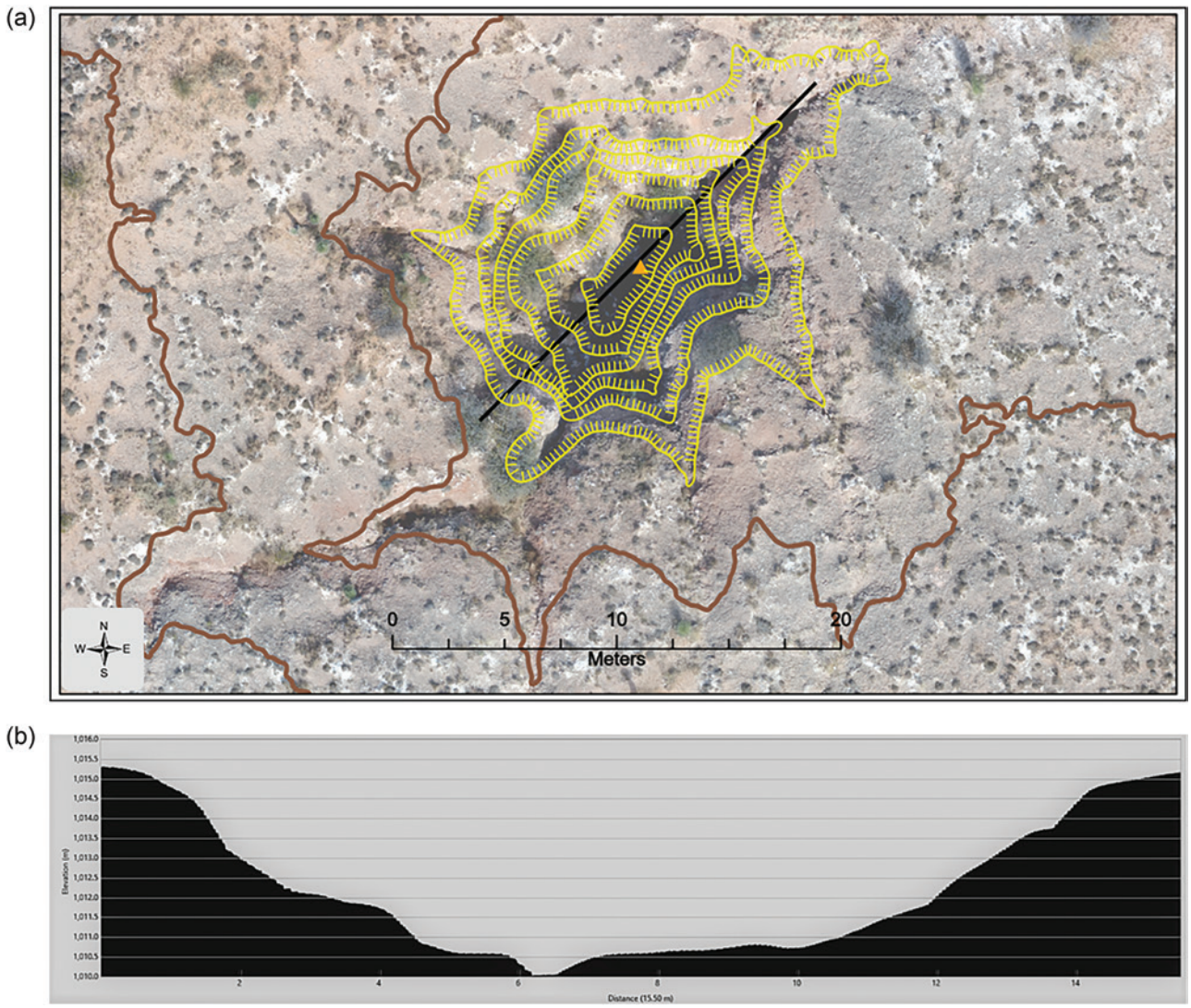


Figure 5. Drone-generated orthomosaic of Whirlpool sink. (A) Yellow-hatched contours demarcate the sinkhole, the orange triangle represents the lowest point, and the brown lines are open contours leading away from the depression. Contours are at 1-m intervals. (B) Elevation profile represented by the black line in the orthomosaic. Drone-derived elevations are relative to the takeoff point and depend on the accuracy of the GNSS at the time of flight.

BV flight elevation was set at a higher flight elevation of 76 m instead of 45 m (Fig. 2) so that the mission could be completed on one battery from the location of the GCS. The flight elevation increase resulted in 2.37 cm spatial resolution instead of sub-one-centimeter spatial resolution for all other depression flights. The vertical accuracy ranged from 2.34 to 7.11 cm.

Depth measured from the drone-derived DEM was obtained from the lowest calculated point to the upper closed contour. DEM depth ranged from 1.54 to 7.46 m, with an average of 5.48 m (Table 3). DEM measured length ranged from 27.9 m (Whirlpool) to 211.8 m (Milliped) with an average of 92.3 m, while the width varied from 21.2 m (Whirlpool) to 83.8 m (Oasis), averaging 48.1 m (Table 4).

The DEM measured perimeters ranged from 77.1 m at Whirlpool sink to 675.4 m at Milliped BV. The average for all five features is 304.3 m (Table 4). The DEM surface area ranged from 179.6 m^2 at Whirlpool sink to 2,601.8 m^2 at Oasis BV, with an average of 1,422.76 m^2 (Table 4). The average depression volume measured from the DEM is 2,152.6 m^3, where Batman's BV is 129.2 m^3 and Milliped BV is 4,339.4 m^3 (Table 4).

Table 6 summarizes all the slope values calculated from the DEM below the upper closed contour for each depression. The GIS software calculates the slope values for all pixels within the depression. The minimum slope value for all depressions is 0.0° except for Whirlpool sink at 0.1°. Gourd BV has the lowest maximum slope value at 60° and Milliped BV has the steepest maximum aggregated slope values of 78.4°. Gourd BV has the lowest mean value of 12.3° while Whirlpool sink has the highest mean slope value of 38.2°. The standard deviation was lowest for Gourd BV (9.7) and

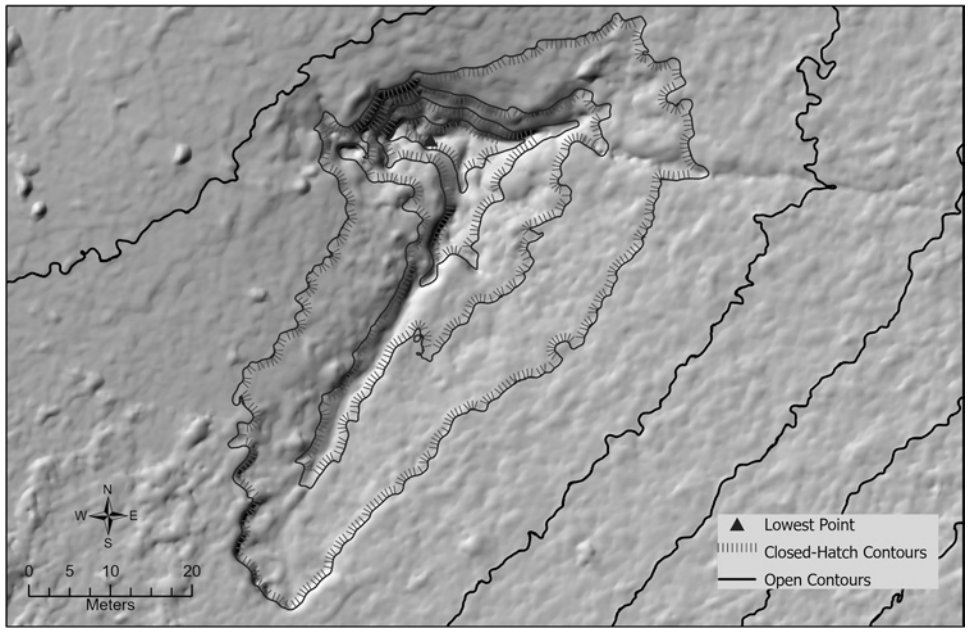


Figure 6. Hillshade model and 1-m contours of Gourd blind valley generated from drone DEM.

Table 2. Joint orientations associated with each karst depression measured in the field.

Site Name	Joint Orientations
Oasis	50°
Batman's	110°
Whirlpool	30°, 120°
Gourd	95°
Milliped	60°, 160°

Table 3. Comparison of field measured depth to DEM depth.

Site Name	Field Depth (m)	DEM Depth (m)	Difference
Oasis	7.62	7.46	−0.16
Batman's	3.05	1.54	−1.51
Whirlpool	9.14	6.71	−2.43
Gourd	7.01	4.32	−2.69
Milliped	10.67	7.37	−3.30
$\bar{x}$	7.50	5.48	−2.02

the highest was for Whirlpool sink (15.6).

DISCUSSION

Many minor karst features in gypsum in southeast New Mexico remain to be catalogued and described in detail (Bachman, 1987). This paper seeks to fill this literature gap with detailed field- and drone-derived DEM measurements of gypsum karst depressions at Sinkhole Flat. There are fourteen large karst depressions in the vicinity of Sinkhole Flat, several of which are not on BLM land. This research focused on five depressions that were difficult to measure in the field due to size, complexity, and safety. The edges of some depressions are steep, fragile, and unstable, making it dangerous to measure the landforms accurately in the field.

LiDAR drones are expensive and exceed the budget of most academic departments' discretionary funds. Also, there are often additional software and hardware purchases, such as proprietary image processing software and RTK GPS, necessary to make the LiDAR data accurate and functional. Sinkholes and other surface geomorphic features can be accurately mapped and characterized using inexpensive visible light (RGB) drones. High-spatial resolution drone DEMs allow for detailed delineation of morphologically complex karst depressions using quantitative methods based on the topography.

Table 4. Field measured length and width and DEM measured length, width, perimeter, area, and volume.

	Field Measured		DEM Measured				
Site Name	Length (m)	Width (m)	Length (m)	Width (m)	Perimeter (m)	Area (m^2)	Vol. (m^3)
Oasis	105.46	77.72	103.60	83.80	388.90	2601.80	4130.50
Batman's	16.46	13.41	31.70	22.70	126.60	298.30	129.20
Whirlpool	19.81	17.67	27.90	21.20	77.10	179.60	340.00
Gourd	19.81	13.41	86.50	45.10	253.60	2074.80	1823.90
Milliped	—	—	211.8	67.70	675.40	1959.30	4339.40

Table 5. **Comparison of field measured cardinal slopes* versus DEM measurements.**

	Field Measurements				DEM Measurements				Differences			
Site Name	**Sn°**	**Se°**	**Ss°**	**Sw°**	**Sn°**	**Se°**	**Ss°**	**Sw°**	**Sn°**	**Se°**	**Ss°**	**Sw°**
Oasis	48	85	40	30	45	67	38	28	−3	−18	−2	−2
Batman's	30	40	90	42	27	39	53	15	−3	−1	−37	−27
Whirlpool	50	78	72	80	49	55	62	54	−1	−23	−10	−26
Gourd	40	20	40	50	33	18	37	48	−7	−2	−3	−2
Milliped	75	62	90	20	68	61	51	18	−7	−1	−39	−2

*Slope north (Sn), Slope east (Se), Slope south (Ss), Slope west (Sw).

Table 6. Summary statistics for all DEM slope values, in degrees, below the upper closed contour.

Site Name	Min	Max	Mean	Std. Dev.
Oasis	0.0	77.4	19.2	13.3
Batman's	0.0	73.3	13.8	10.6
Whirlpool	0.1	79.1	38.2	15.6
Gourd	0.0	60.0	12.3	9.7
Milliped	0.0	78.4	36.1	15.2

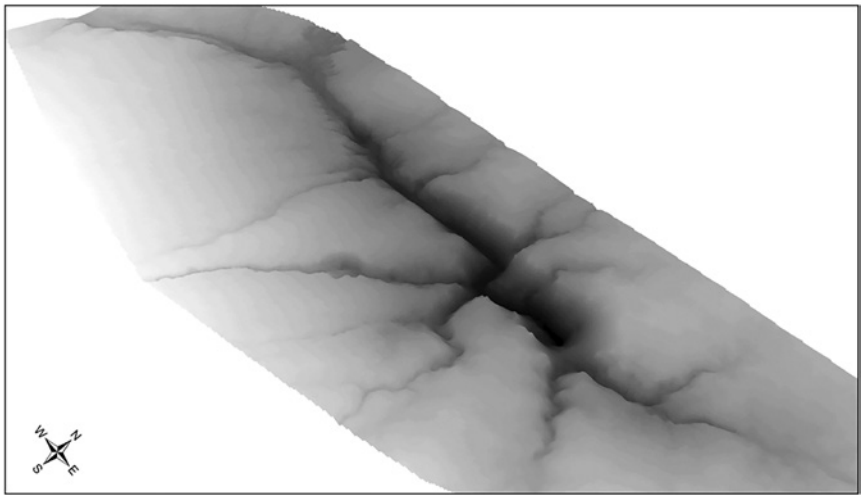


Figure 7. 3D elevation model of Milliped blind valley and tributaries (scale varies in this perspective).

One of the disadvantages of using a visible light sensor is the obstruction of geomorphic details by vegetation, even in arid regions. While conducting field work, some of the depressions had large clusters of wind-blown tumbleweed accumulated in narrow or low places including cave entrances. Contour lines generated from the DEM in a GIS are affected by heaps of dead vegetation, taller living vegetation, and the brittle, crumbly nature of gypsum near depression edges.

The mean field measured depression depth was 7.5 m while the mean DEM measured depth was 5.48 m (Table 3). All DEM depths were less than the actual field measured depths, ranging from −0.16 m for Oasis BV to −3.3 m for Milliped BV. Since there are significant differences between the field measured depths and drone measured depths, perhaps a double grid pattern could be flown for additional images to potentially capture more angles to map the depression depth more accurately.

Oasis BV has the largest surface area of 2,601.8 m^2 (Table 4), but Milliped BV has the largest volume of 4,339.4 m^3 (Table 6). This may be related to slope values where the Oasis BV average slope is 19.2° m and Milliped BV average slope is 36.1° m (Table 6). Perimeter is the continuous line forming the boundary of a closed geometric figure. Oasis BV has the second longest perimeter of 388.9 m compared to Milliped BV, which has the longest perimeter of 675.4 m.

Batman's BV has unique hydrogeomorphic conditions that allow a large mesquite tree (Fig. 4) to grow in its base adjacent to the cave entrance. This large tree conceals the morphology of the blind valley so that when the drone-generated DEM is used to measure the morphometric characteristics, it appears shallower and with gentler slopes (Tables 3, 5, and 6). Also, this blind valley has the lowest volume of only 129.2 m^3 because of the presence of a tree in its deepest section. Batman's BV is also the shallowest depression with a field measured depth of 3.05 m compared to 1.54 m measured from the DEM (Table 3).

Whirlpool sink was the only true sinkhole in this study. It is the most compact depression with the lowest surface area of 179.6 m^2 and shortest perimeter of 77.1 m (Table 4). It has the 2nd deepest field measured depth of 9.14 m, but its DEM measured depth ranked 3rd deepest (Table 3). This small anomaly is probably due to topographic shadowing associated with its steep slopes affecting accurate DEM generation and a layer of tumbleweed at the bottom. DEM measured slopes for Whirlpool sink are the steepest in the study, ranging from 0.1° to 79.1°, with an average of 38.2° (Table 6).

Gourd BV flight elevation was set at a higher flight elevation of 76 m instead of 45 m so that the mission could be completed on one battery from the location of the GCS. The flight elevation increase resulted in 2.37 cm (Table 1) spatial resolution instead of sub-one-centimeter spatial resolution for all other depression flights. In the field, it was noted that the surface drainage originates from the east. Examination of the DEM illustrates the elongated NNE–SSW shape of the depression and the broad, shallow surface drainage originating from the SSW (Fig. 6). Surface drainage originating from the east aligns with the cave entrance joint orientation of 95° (Table 2) and is readily apparent in the field.

Milliped BV is oriented east–west and is long, narrow, and deep with more than a dozen first-order tributaries (Fig. 7). It has the deepest field measured depth of 10.67 m, but its DEM measured lowest point is 7.37 m (Table 3). The east–west orientation of this depression created shadows on the south slopes (northern aspect) during the drone flight, concealing details of depth and slope. Field measured slopes reveal the shadowing effect when compared to the DEM slopes. The field measured southern slope adjacent to the cave entrance is 90° and the equivalent location on the DEM is 51°, which is a −39° difference (Table 5). Milliped's DEM measured length is 211.8 m, which is more than twice the length of Oasis. Milliped BV also has the longest perimeter of 675.4 m and the greatest volume of 4,339.4 m^3 (Table 4).

One of the limitations of this study was the lack of documentation of the exact locations for field length and width measurements. Oasis BV field versus DEM measurements (Table 4) were relatively similar, followed by Whirlpool sink. Both depressions are deep with easily recognized boundaries in the field. However, the remaining depressions' dimensions and morphology were difficult to determine in the field due to the subtle nature of surface tributaries for Batman's and Gourd blind valleys (Figs. 4 and 6). In the case of Milliped BV, the numerous deeply incised tributaries (Fig. 7) made it challenging to demarcate the outline of this depression in the field. Drone images were not processed in the field while camping at Sinkhole Flat due to limited resources; each drone flight required about 1 h of computer processing time, and the vehicle was only used for charging drone batteries via an inverter.

CONCULSIONS

Inexpensive visible light (RGB) drone imagery can be used to create relatively accurate maps for karst depression and geomorphometric analysis in sparsely vegetated arid areas. Surface area can be measured accurately, but because depth is obscured by shadows and vegetation, drone measured depths can vary by several meters.

Drone orthomosaics and DEM-derived layers make it possible to visualize and quantify the complex morphology of the karst depressions that cannot easily be seen from the ground. Drone imagery can be used to rapidly map and assess gypsum depressions in arid areas. The use of an affordable RGB drone to map surface features is possible in arid areas, open fields, sparsely vegetated outcrops, or low-density urban areas.

Terrain shadows and low sun angles obscure the true depth and slope values of drone-generated DEM's and slope models. A double grid pattern (flight lines perpendicular to each other) flown by the drone will increase the number of images collected from different angles to increase DEM accuracy and thereby improve the accuracy of derivative layers such as contouring and slope values. Drone flights should occur between the hours of 11:00 am and 1:00 pm to reduce topographic shadowing of karst depressions and to improve the accuracy of the DEM.

REFERENCES

Bachman, G. O., 1987, *Karst in Evaporites in Southeastern New Mexico*: Albuquerque, New Mexico, Sandia National Labs., https://www.osti.gov/biblio/5947512

Beck, W. A and Hasse, Y. D., 1969, *Historical Atlas of New Mexico*: Norman, Oklahoma, University of Oklahoma Press, 62 p.

Chenoweth, M. S., 1997, The spatial distribution and morphometric analysis of dolines, Buffalo National River, Newton County, Arkansas [MA thesis]: Fayetteville, University of Arkansas, 94 p., https://www.proquest.com/docview/304338686?pq-origsite=gscholar&fromopenview=true.

Cokendolpher, J. C and Polyak, V. J., 1996, Biology of the caves at Sinkhole Flat, Eddy County, New Mexico: Journal of Caves and Karst Studies, v. 58, no. 3, p. 181–192. https://caves.org/pub/journal/PDF/V58/v58n3-Cokendolpher.htm

Ford, D. C and Williams, P., 2007, *Karst Hydrogeology and Geomorphology*: Chichester, England, John Wiley, 562 p., https://doi.org/10.1002/9781118684986.

Gijón-Yescas, N. G., Aguilar-Duarte, Y. G., Frausto-Martínez, O., and Bautista-Zuñiga, F., 2021, Anatomy of a Cenote with use of Dron: Tropical and Subtropical Agroecosystems, v. 24, no. 30, p. 1–14, https://www.revista.ccba.uady.mx/ojs/index.php/TSA/article/view/3634

Gilli, É., 2015, *Karstology: Karsts, Caves and Springs: Elements of Fundamental and Applied Karstology*: Boca Raton, Florida, CRC Press, 256 p.

Johnson, K. S., 1997, Evaporite karst in the United States: Carbonates and Evaporites, v. 12, no. 1, p. 2–14, https://doi.org/10.1007/BF03175797

Kim, Y. J., Nam, B. H., and Youn, H., 2019, Sinkhole detection and characterization using LiDAR-derived DEM with logistic regression: Remote Sensing, v. 11, no. 13, p. 1592, https://doi.org/10.3390/rs11131592

Land, L., 2013, Geophysical records of anthropogenic sinkhole formation in the Delaware Basin region, southeast New Mexico and west Texas, USA: Carbonates and Evaporites, v. 28, no. 1–2, p. 183–190, https://doi.org/10.1007/s13146-013-0126-9

Lobeck, A. K., 1939, *Geomorphology, An Introduction to the Study of Landscapes*: New York, McGraw-Hill Book Company, 731 p.

Medellín-Leal, F., 1982, The Chihuahuan desert, *in* Bender, G. L., ed., *Reference Handbook on the Deserts of North America*: Westport, Connecticut, Greenwood Press, 594 p.

Mihevc, A and Mihevc, R., 2021, Morphological characteristics and distribution of dolines in Slovenia, a study of a LiDAR-based doline map of Slovenia: Acta Carsologica, v. 50, no. 1, p. 11–36, https://doi.org/10.3986/ac.v50i1.9462

Powers, D. W., Beauheim, R. L., Holt, R. M., Hughes, D. L., and Land, L., 2006, Evaporite karst features and processes at Nash Draw, Eddy County, New Mexico, *in* New Mexico Geological Society Fall Field Conference Guidebook, Volume 57: Socorro, New Mexico, New Mexico Geological Society, p. 253–266.

Silva, O. L., Bezerra, F. H., Maia, R. P., and Cazarin, C. L., 2017, Karst landforms revealed at various scales using LiDAR and UAV in semi-arid Brazil: Consideration on karstification processes and methodological constraints: Geomorphology, v. 295, p. 611–630, https://doi.org/10.1016/j.geomorph.2017.07.025

Stafford, K. W., Rosales-Lagarde, L., and Boston, P. J., 2008, Castile evaporite karst potential map of the Gypsum Plain: Eddy County, New Mexico and Culberson County, Texas: a GIS Methodological Comparison: Journal of Cave and Karst Studies, v. 70, no. 1, p. 35–46, https://caves.org/pub/journal/PDF/v70/cave-70-01-35.pdf

Stafford, K. W., Ehrhart, J. T., Majzoub, A. F., Shields, J. M., and Brown, W. A., 2018, Unconfined hypogene evaporite karst: West Texas and southeastern New Mexico, USA: International Journal of Speleology, v. 47, no. 3, p. 293–305, https://doi.org/10.5038/1827-806X.47.3.2166

Tait, D. B., Ahlen, J. L., Gordon, A., Scott, G. L., Motts, W. S., and Spitler, M. E., 1962, Artesia group of New Mexico and West Texas: AAPG Bulletin, v. 46, no. 4, p. 504–517, https://doi.org/10.1306/BC74383B-16BE-11D7-8645000102C1865D

WRCC, 2022, Desert Research Institute (DRI) Western Regional Climate Center, wrcc.dri.edu: https://wrcc.dri.edu/cgi-bin/cliMAIN.pl?nm1469

GUIDE TO AUTHORS

The *Journal of Cave and Karst Studies* is a multidisciplinary journal devoted to cave and karst research. The Journal is seeking original, unpublished manuscripts concerning the scientific study of caves or other karst features. Authors do not need to be members of the National Speleological Society, but preference is given to manuscripts of importance to North American speleology.

LANGUAGES: The *Journal of Cave and Karst Studies* uses American-style English as its standard language and spelling style. A second abstract in another language will be considered when room allows and is determined necessary. In the case of proper names, the Journal tries to accommodate other spellings and punctuation styles. In cases where the Editor-in-Chief finds it appropriate to use non-English words outside of proper names (generally where no equivalent English word exist), the Journal italicizes them. Common abbreviations, i.e., e.g., et al., etc. should appear in normal text. Authors are encouraged to write for our combined professional and amateur readerships. Spell out first use of acronyms.

CONTENT: Each paper will contain a title, the authors' names and addresses, an abstract, and the text of the paper, including a summary or conclusions section. Acknowledgments and references are to follow the text. Manuscripts should be limited to 6,000 words and no more than 10 figures and 5 tables. Larger manuscripts may be considered, but the Journal reserves the right to charge processing fees for larger submissions.

ABSTRACTS: An abstract stating the essential points and results is required. The abstract is to be a summary, not a promise of what topics are covered in the paper.

STYLE: The *Journal* consults The Chicago Manual of Style on most general style issues.

REFERENCES: References to previously published work should be followed by the relevant author's name and date in parentheses. All cited references are to be listed alphabetical at the end of the manuscript with senior author's last name first, followed by date of publication, title, publisher, volume, and page numbers. Geological Society of America format should be used (see http://www.geosociety.org/gsa/gsa/pubs/Ref-Guide-Examples). Please do not abbreviate periodical titles. Web references are acceptable when deemed appropriate. The references should follow the style of: Author (or publisher), year, Webpage title: Publisher (if a specific author is available), full URL (e.g., http://www.usgs. gov/citguide.html), and the date the website was accessed in brackets. If there are specific authors given, use their name and list the responsible organization as publisher. Citations within the text should read: (Author, Year).

SUBMISSION: Manuscripts are to be submitted via the PeerTrack submission system at https://www.editorialmanager.com/jcks. Additional instructions are provided at that address. You will be prompted to establish a login and password, after which you will enter information about your manuscript and upload your manuscript, tables, and figure files. Manuscript files can be uploaded as DOC, WPD, RTF, TXT, or LaTeX. Note: LaTeX files should not use any unusual style files; a LaTeX template and BiBTeX file may be obtained from the Editor-in-Chief. Table files can be uploaded as DOC, WPD, RTF, TXT, XLS, or LaTeX files and figure files can be uploaded as TIFF, AI, EPS, or CDR files. The including of supplementary materials should be minimized. Supplemental data or other materials (e.g. video clips) may be placed on the Journal's website at the discretion of the Editor-in-Chief. The data used within a paper must be made available upon request during the review process.

FIGURES: Figures and lettering must be neat and legible. A list of figures and their captions should be provided at the end of the text or as a separate document and not within the figure. Figures should be numbered in sequence and referred to in the text by inserting (Fig. x). Most figures will be reduced; hence, the lettering should be large. Photographs must be sharp and high contrast. Figures must have a minimum resolution of 300 dpi for acceptance. Please minimize the use of JPEG images.

TABLES: See https://caves.org/wp-content/uploads/2022/01/JCKS_Tables.pdf. for table layout guidelines.

MEASUREMENTS: All measurements will be in the International System of Units (SI or metric) except when quoting historical references. Other units will be allowed where necessary if placed in parentheses following the SI units.

DISCUSSIONS: Critical discussions of papers previously published in the Journal are welcome. Authors will be given an opportunity to reply. Discussions and replies must be limited to a maximum of 1000 words and discussions will be subject to review before publication. Discussions must be within 12 months after the original article appears.

COPYRIGHT AND AUTHOR'S RESPONSIBILITIES: The submitted work should represent original work of the author(s) that has not been previously published. It is the author's responsibility to clear any copyright or acknowledgement matters concerning text, tables, or figures used from others. Authors should address sensitive or legal issues such as landowner and land manager concerns or policies, verify that the work was conducted using necessary permissions and permits, and minimize the disclosure of sensitive features and cave locations.

PROCESS: Submitted manuscripts are assigned to the appropriate Associate Editor and sent out to at least two experts in the field for review. Reviewed manuscripts are then returned to the author for consideration of the referees' remarks and revision, where appropriate. Revised manuscripts are returned to the Associate Editor who then recommends acceptance or rejection. The Editor-in-Chief makes final decisions regarding publication. Upon acceptance, the senior author will be sent one set of PDF proofs for review prior to publication.

Journal of Cave and Karst Studies

Volume 88 Number 3 September 2026

CONTENTS

Article 45
The relationship between sediment geochemistry, manganese oxidation, human traffic, and microbial community structure across three southern Appalachian caves
Sarah Carmichael, James Seward, Bryce Norvell, Lucca Scoggins, Anna-Maria Riley, Morgan Smith, Howard Neufeld, and Suzanna Bräuer

Article 62
Herpetofauna in the caves of the Andaman Islands: An appeal for conservation measures
Dhanusha Kawalkar, Priyanka Desai, Rima Sadhukhan, Pooja Patil, and Shirish Manchi

Article 72
First Folia occurrence from Greece
Georgios Lazaridis and Panagiotis Sotirios Dittopoulos

Article 78
Mapping groundwater infiltration in Karst using LIDAR at Natural Bridge Caverns, Texas
Matthew Kaspar, Kathryn Brown, Jonathan D. Price, Brian Vauter, and Kashif Mahmud

Article 100
Morphometric analysis of gypsum depressions using drone imagery at sinkhole flat, Eddy County, New Mexico, USA
Michael Sean Chenoweth